



UNIVERSITÀ
DEGLI STUDI
DI PADOVA

Sede Amministrativa: Università degli Studi di Padova

Dipartimento di Scienze Chimiche

SCUOLA DI DOTTORATO DI RICERCA IN : SCIENZE MOLECOLARI

INDIRIZZO: SCIENZE CHIMICHE

CICLO XXVIII

COVALENT STABILIZATION OF 2D SELF-ASSEMBLED NANOSTRUCTURES ON SURFACES

Direttore della Scuola : Ch.mo Prof. Antonino Polimeno

Coordinatore d'indirizzo: Ch.mo Prof. Antonino Polimeno

Supervisore :Ch.mo Prof. Mauro Sambi

Dottorando : Andrea Basagni

Riassunto

La scoperta del grafene ha suscitato grande interesse verso i materiali a bassa dimensionalità (0D, 1D e 2D) e uno sforzo congiunto tra i diversi rami della scienza è orientato verso la produzione di nuovi materiali con proprietà analoghe a quelle del grafene, ma controllabili. La sintesi su superficie in condizioni di ultra-alto vuoto (UHV) sembra essere promettente per la produzione di nanostrutture organiche. Infatti, in queste condizioni, è possibile avere un'ampia varietà di materiali, un perfetto controllo delle condizioni di reazione, della simmetria della superficie e della sua corrugazione. Questi sono solo alcuni dei vantaggi che l'UHV offre. Sebbene varie reazioni siano state testate negli ultimi anni, sembra chiaro che per realizzare monostrati polimerici ordinati siano necessari approcci più complessi. In questo lavoro di Tesi, la sintesi di nanostrutture polimeriche su superficie è stata studiata per diverse reazioni, substrati e condizioni di reazione. La microscopia ad effetto tunnel e la spettroscopia di fotoemissione a raggi X sono state utilizzate per la caratterizzazione dei diversi sistemi permettendo un'analisi complementare delle strutture molecolari e dei loro stati chimici. In particolare, le reazioni attivate termicamente sono state utilizzate per polimerizzare gradualmente il 4,4"-dibromoterfenile e ottenere, in un primo step di reazione, per mezzo della reazione di Ullmann su Au (111), il poli-parafenilene, e poi nanoribbons di grafene dopo l'attivazione dei legami C-H. Un delicato equilibrio tra l'attività catalitica della superficie, la mobilità molecolare e l'organizzazione molecolare ha permesso di ottenere strutture ordinate estese. Inoltre, sfruttando questa metodica, sono stati ottenuti tre differenti polimeri 1D, caratterizzati da un crescente contenuto di azoto. Campioni macroscopicamente anisotropici sono stati preparati sfruttando l'effetto templante delle superfici vicinali e, grazie alla spettroscopia di fotoemissione risolta in angolo, è stato rivelato che la struttura elettronica dei polimeri drogati è rigidamente spostata verso energie minori rispetto al livello di Fermi del metallo all'aumentare del contenuto di azoto.

Infine, è stata esplorata l'attivazione fotochimica di diversi gruppi funzionali. Questi studi rappresentano un passo avanti verso l'applicazione della fotochimica alla sintesi su superficie, che attualmente sfrutta solo gruppi diacetilenici, e apre nuove opportunità per l'utilizzo di diversi gruppi funzionali organici come centri fotoattivi.

Abstract

The rise of graphene has attracted great interest in low-dimensional materials (0D, 1D and 2D). A joint effort among the different branches of science (chemistry, physics, materials science and related areas) is directed towards the production of new intriguing materials with tuneable graphene-like properties. Promising is the direct synthesis of organic nanostructures on metal surfaces under ultrahigh-vacuum conditions (UHV). Perfect tuning of the reaction conditions, high control of the surface symmetry and of its corrugation, a rich variety of substrate materials are only some of the advantage that UHV may offer. Although several reactions have been tested, it seems clear that to achieve ordered covalent monolayers more complex approaches are needed. In this thesis, the on-surface polymerization of covalent nanostructures has been studied for different coupling reactions, substrate materials and reaction conditions. Scanning tunneling microscopy and X-ray photoelectron spectroscopy are used for the characterization, allowing complementary analysis of molecular structures and chemical states. In particular, thermally activated reactions were used to gradually polymerize the 4,4"-dibromo-terphenyl precursor into poly-paraphenylene wires, through an Ullmann-like reaction scheme on Au(111), and then into graphene nanoribbons, after activation of the C-H bonds. A fine balance between the catalytic activity of the surface, molecular mobility and favourable molecular organization allowed us to get extended and ordered covalent structures. Taking advantage of this synthetic pathway, three different mono-dimensional polymers were obtained, namely poly-paraphenylene and two pyridinic derivatives, with gradually increased nitrogen content. Macroscopically anisotropic samples have been prepared by taking advantage of the vicinal surface templating effect. Using angle resolved photoemission spectroscopy, we reveal that the electronic structure of doped polymers is monotonically downshifted with respect to the metal Fermi level as the pyridine substitution is increased within the molecular scaffold.

Finally, the photochemical activation of different functional groups has been explored. These studies represents a step forward in the application of organic photochemistry to on-surface synthesis, which is currently limited to the use of diacetylene groups, and it opens up new opportunities for using several organic functional groups as photoactive centres for the synthesis of covalent organic frameworks.

Table of Contents

Introduction	3
Low-dimensional materials: an anecdotal existence	5
Flask type approaches.....	7
Interfacial approaches	11
On-Surface Synthesis	15
Thermal Activations.....	18
Ullmann coupling	20
Homo-coupling of terminal alkynes	25
Decarboxylation of organic acids	26
Dehydrogenation reactions	27
Photochemical activation.....	29
A little bit of theory	30
Summary and Outlook	34
Results	35
Molecules-Oligomers-Nanowires-Graphene Nanoribbons: a bottom-up stepwise on-surface covalent synthesis preserving long-range order	35
Tuning the one-dimensional band dispersion of on-surface synthesized organic nanowires	43
Stereoselective photopolymerization of tetraphenylporphyrin derivatives on Ag(110) at the sub-monolayer level	72
Summary and outlook.....	83
Publications	96

Introduction

Synthetic organic chemistry allows us to reproduce intriguing natural molecules in the laboratory and to apply the developed synthetic strategies to construct their derivatives. Such molecules have significantly aided biology and medicine, since they often find applications as biological tools and as drug candidates.^[1] The ability of man to replicate the molecules of living creatures, and create other molecules like them, is a remarkable development in human history.^[2] In fact, thanks to the sophisticated catalytic reactions and to the developed synthetic processes, we can not only synthesize the natural products and their analogues, but also a myriad of other organic molecules for potential applications in technology and everyday life.^[3] Therefore it is not a surprise that chemistry, the science of matter, is considered the central science lying between physics and biology. Its power derives from its ability to isolate and analyse molecules and to synthesize them from atoms or to modify other molecules at one's own choice. Synthesis, in particular, takes an important role to improve our well-being, since we create new chemical entities to satisfy specific needs.

Over the years, synthetic chemistry has provided solutions for many compelling questions, such as how to achieve stereo-control during reaction steps, to design and prepare powerful drugs, to develop efficient, green and sustainable protocols and to create polymers with tailor-made properties.^[4-6] Thus, the ability to interconnect atoms by covalent bonds has been strongly mastered for both "small" compounds, i.e. individual molecular compounds, and single-stranded polymers that can attain appreciable sizes. Nowadays, many synthetic polymers are the basis of numerous commercial products and they are synthesized industrially on a hundred-million-ton annual scale. Recently developed controlled polymerization methods provide increasing control of the chain lengths, excellent functional-group tolerance and access to novel copolymers.^[7-9] The chemical bonds in all these compounds and polymers are arranged in a rather complex but laterally hardly extended geometry or in long zigzag or helical geometries. Looking at the topology of these molecules by means of a somewhat coarser picture, the small compounds could be considered as "zero-dimensional" (0D) objects, whereas the polymeric chains as "one-dimensional" (1D) (irrespective of the tendency to form secondary and tertiary structures). Thus, from the point of view of dimensionality, there is substantial space for the

development of synthetic chemistry, namely in the direction of extended, yet precisely defined 2D and 3D structures. In fact, comparatively few polymerization methods have been developed to obtain regular two-dimensional structures, a challenge that lies at the interface of polymer science and molecular self-assembly.^[10] Of course, the creation of extended organic matter in the bulk phase, crystals, and thin films has always been at the heart of chemistry, but the tools were mainly non-covalent interactions. The recent decades have been characterized by enormous progress in understanding and controlling the organization of smaller components into larger units.^[11,12] Examples span from artificial membranes, surface patterning and the generation of functional 3D bulk materials through self-assembly and phase-segregation processes of carefully designed components.^[13–15] The fact that the production of these complex aggregates were obtained by intermolecular forces weaker than covalent bonds, suggests that there is still a barrier for the organic synthesis to cross the border between the 0D and 1D molecules on one side and extended 2D and 3D structures on the other. Thus, developing methods to progress into this direction holds great promise to advance chemistry.

Nanostructures with reduced dimensionality, such as quantum dots (0D), nanowires (1D) and single layer materials (2D), recently attracted increasing interest in the emerging fields of nanoscience, mainly due to their promising potential in applications as electronic and optoelectronic devices.^[16,17] Most nanostructures reported are based on inorganic materials,^[18] such as metal oxide/sulphide/selenide or perovskite sheets,^[19,20] while surface-supported organic materials have been much less thoroughly studied to date. Organic materials could provide many advantages over the inorganic counterparts, such as an unlimited choice of molecular structures for property optimization, high flexibility and low cost fabrication. Thus, this research activity is devoted to studying new procedures for the production of covalent layers and to provide novel general synthetic routes to get low dimensional materials. Self-assembly processes have been used to growth polymers at the metal/vacuum interface. The intrinsically reduced dimensionality of a surface allows one to confine all the molecular processes on a plane and therefore offers a reliable way to prepare true monoatomic-thin covalent layers. Finally, this interfacial approach offers an easy way to pay a large portion of the entropy price associated with the formation of 2D polymers. However, this method is still in its infancy and a larger number of case studies is required in order to provide a battery of working synthetic paths.

Low-dimensional materials: an anecdotal existence¹

More than 70 years ago, Landau and Peierls argued that strictly 2D crystals were thermodynamically unstable and could not exist.^[21–23] Their theory pointed out that a divergent contribution of thermal fluctuations in low-dimensional crystal lattices should lead to such displacements of atoms that they become comparable to interatomic distances at any finite temperature.^[24] The argument was later extended by Mermin^[25] and is strongly supported by an omnibus of experimental observations. Indeed, the melting temperature of thin films rapidly decreases with decreasing thickness, and the films become unstable (segregate into islands or decompose) at a thickness of, typically, dozens of atomic layers.^[26,27] For this reason, atomic monolayers have so far been known only as an integral part of larger 3D structures, usually grown epitaxially on top of single crystals with matching crystal lattices.^[26,27] Without such a 3D base, 2D materials were presumed not to exist, until 2004, when the common wisdom was flaunted by the experimental discovery of graphene and other free-standing 2D atomic crystals such as single-layer boron nitride and $B_xC_yN_z$,^[28,29] see Figure 1.

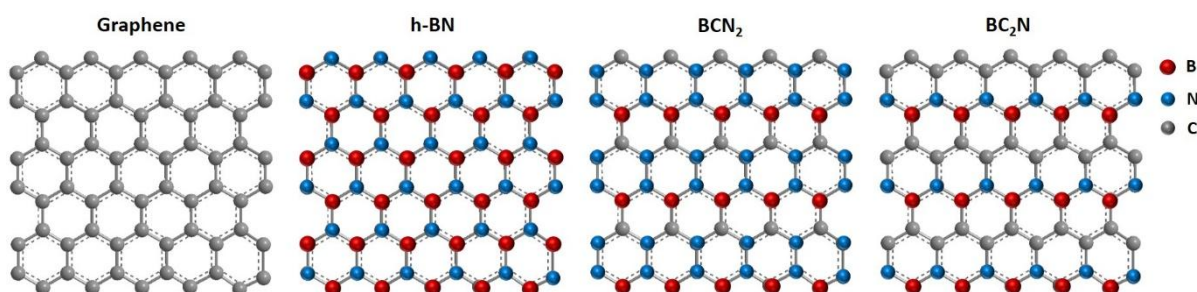


Figure 1: ball and stick models of the graphene, hexagonal boron nitride (h-BN) and other $B_xC_yN_z$ nanomaterials.

These crystals could be obtained on top of non-crystalline substrates in liquid suspension and as suspended membranes.^[28–30] With the benefit of hindsight, the existence of such one-atom-thick crystals can be reconciled with theory. Indeed, it can be argued that the obtained 2D crystallites are quenched in a metastable state because they are extracted from 3D materials, whereas their small size ($\ll 1$ mm) and strong interatomic bonds ensure that thermal fluctuations cannot lead to the generation of dislocations or other crystal defects even at elevated temperature.^[24,25]

¹ This chapter has been adapted with permission from ref. ^[21,36].

Graphene is a rapidly rising star on the horizon of materials science and condensed-matter physics. This strictly two-dimensional material exhibits exceptionally high crystal and electronic quality, and, despite its short history, has already given rise to new physics and interesting potential applications.^[31–34] Whereas one can be certain of the realness of applications only when commercial products appear, graphene no longer requires any further proof of its importance in terms of fundamental physics. Owing to its unusual electronic spectrum, graphene has led to the emergence of a new paradigm of 'relativistic' condensed-matter physics, where quantum relativistic phenomena, some of which are unobservable in high-energy physics, can now be mimicked and tested in table-top experiments.^[35]

More generally, graphene represents a conceptually new class of materials that are only one atom thick, and, on this basis, offers new inroads into low-dimensional physics that has never ceased to surprise and continues to provide a fertile ground for applications. Thus, it makes sense to examine other low-dimensional polymers for technological applications. In fact, the inherent simplicity of the graphene lattice, with each sub-lattice represented by just a single atom in the unit cell, limits the possibilities for structural modification. This has led to an ongoing search for new materials with customizable properties since the design opportunities of organic-conjugated polymer chemistry may allow us to access unprecedented structural diversity.^[10]

Up to now, the strategies applied to obtain atomically thin 2D polymeric nano-sheets are mainly divided into two categories: “interfacial/spatially-confined” and “flask type” approaches. Interfacial/spatially-confined approaches lead to materials with a lateral extension up to several micrometres, in contrast, the solution synthesis are circumscribed and only oligomers with limited lateral size have been synthesized up to now. Among all, facile reaction protocols leading to free-standing low-dimensional materials are still a challenge for both methods.

Flask type approaches

Numerous all-carbon networks were initially proposed in the 1980s and have caught the interest of many synthetic chemists to try to prepare such unusual structures. Although these networks were never actually realized, drawings of them have been published repeatedly.^[36–38]

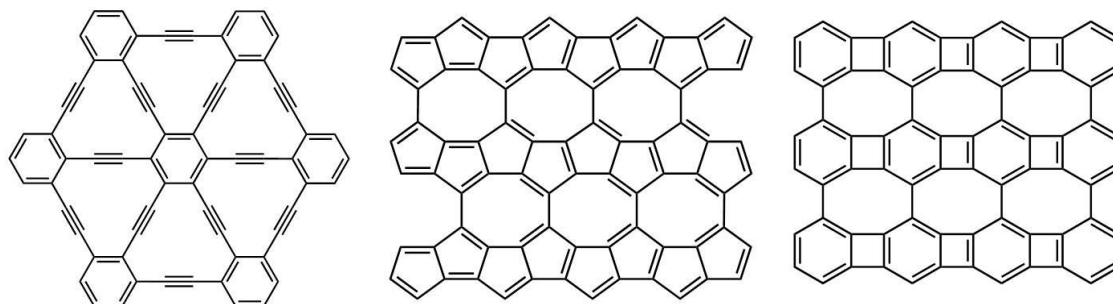


Figure 2: chemical structure of some hypothetical all-carbon networks whose electronic structures have been theoretically investigated.

The main difference between solution and interfacial approaches is that monomers are not automatically arranged into the same plane, as occurs if the synthesis is conducted directly at the interface. Thus, monomer design has to overcome this disadvantage in order to ensure the growth into a non-perturbed 2D geometry. The number and the mutual arrangement of the reactive sites and the flexibility of the scaffold of the monomers have to be properly designed. The monomers must be equipped with at least three functionalities (reactive sites) for network formation, while flexible spacers between the bond-forming sites and the skeleton should be avoided altogether.

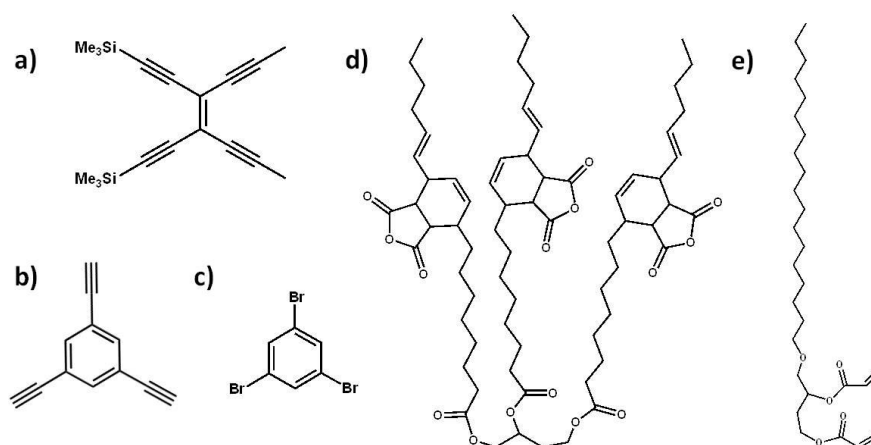


Figure 3: Structures of some already used precursors for the synthesis of 2D networks.

One can thus easily imagine that monomers such as those reported in Figure 3d-e have no chance in homogeneous solutions, while in the interfacial approach such linkers may be acceptable under certain conditions. In fact, these monomers are too

flexible and there is no force in solution that would direct them into a 2D geometry, since there are several 3D nearly-degenerate conformations. From this point of view, monomers 3b-c may be considered more reasonable candidates. Looking at the reaction steps, three coupling reactions have to occur in the same plane for each monomer, with this plane defined by the central benzene rings of the monomers. Even if one assumes that two monomers approach and bond with a parallel mutual orientation, which is unlikely, at some point two oligomers have to couple to a bigger one. The low rotational barrier of the forming covalent bond allows for a nearly free rotation of oligomeric fragments relative to one another, and will do so while growing further at their numerous reactive sites. At the end, it is highly improbable that all bond formation steps will occur when the fragments lie in a coplanar conformation. In addition, depending on the shape of the reacting fragments and the location of connecting points, it may no longer be possible to covalently stabilize the in-plane conformation. This inevitably leads to overlapping structures that eventually furnish 3D networks or to larger entities with internal holes. Such holes are formed whenever two fragments with non-complementary edges join at two points. It then depends very much on statistics whether the holes in the sheet are closed by unreacted monomers properly growing inwards. All these defects will strongly affect the properties of the materials such as gas permeation, conductivity or catalytic activity. Another critical aspect in the solution approach is the enormously fast loss of solubility with increasing size of the polymer.^[39,40] Brick-stone-like insolubility is commonly observed after having reached sizes of few nanometres, non-processable and non-isolable materials are easily obtained, which renders post-synthesis characterization difficult, if not impossible. Rigidity clearly plays a fatal role in this matter, but more tricks could be exploited to keep the polymeric sheets in solution, such as substituting the monomers with lateral alkane chains or introducing charges spread over the sheet. Finally, another aspect is the conformation of a 2D polymer in solution since such polymers may spontaneously roll up or even form tubes under certain conditions.

Significant efforts^[41] have been devoted to establish reliable and broadly applicable pathways to prepare ordered polymers taking advantage of self-assembly processes in homogeneous media. To date, a couple of beautiful examples^[42,43] highlights the possibility to exploit this combined synthetic approach and are reported in Figure 4.

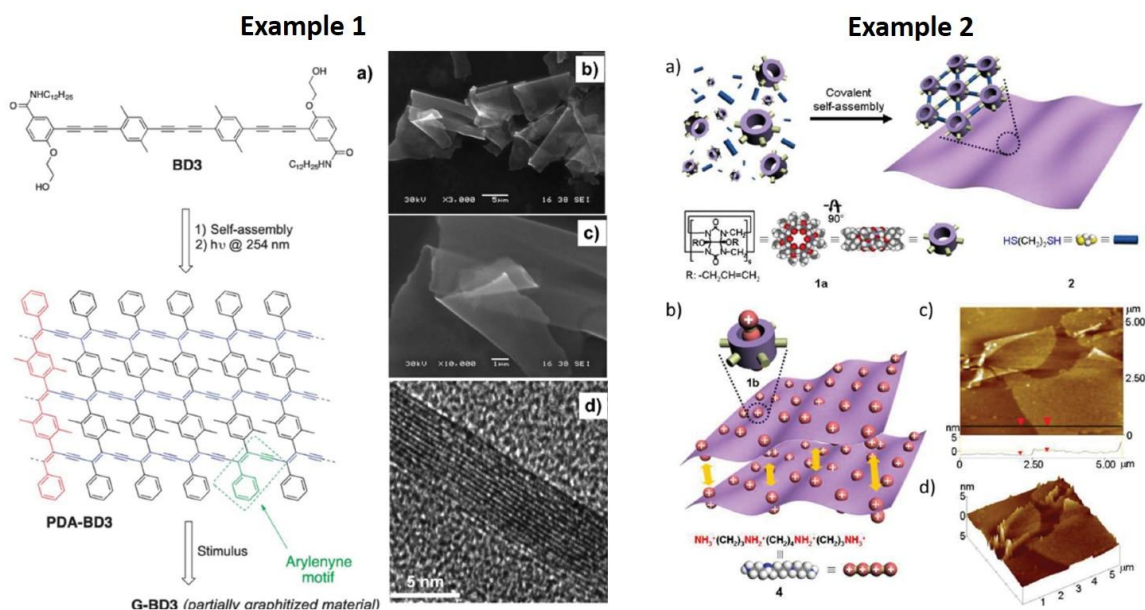


Figure 4: Two examples of the preparation of free-standing 2D polymers taking advantage of self-assembly processes. **Example 1:** the reaction scheme is reported in **a)**, while **b-c)** are SEM images of the respective product. **d)** shows a zoom-in of a folded edge. **Example 2:** **a)** the irreversible self-assembly of (allyloxy)₁₂CB[6] and 1,2-ethanedithiol. **b)** Schematic representation of the electrostatic repulsion induced by the spermine residues, **c-d)** AFM images of the product. Adapted with permission from ref [43], [42]. Copyright 2013 American Chemical Society.

The first one^[42] adopts a linear precursor with three butadiene units separated by phenyl spacers and once they organize upon gelification, the gel is spread onto a large surface and dried. Extended ultraviolet irradiation leads to the stabilization of multilayer nanostructured sheets with an average thickness of 160 nm. Another recent work^[43] adopts a rigid disk-like molecule with alkene peripheral functional groups. A thiol-ene click reaction between the precursor and a simple thiol (1,2-ethanedithiol) leads to the formation of a periodic nanosheet. In addition, positive charges spread on both sides of the covalent layer, due to the protonation of the external spermine residues, cause the electrostatic separation of different nanosheets. The obtained one-monomer-thick 2D polymer is characterized by a thickness of 2.8 nm and lateral dimension up to several micrometers.

A possible retrosynthetic analysis of a two-dimensional polymer could be in principle the lateral-connection of *n*-stranded polymers, and many years ago serious attempts were undertaken to grow the isolated filaments perpendicularly to their main axis.^[44–46] Although it is relatively simple to get linear long polymers, this was hardly possible in the 2nd-direction, since a systematic increase in the lateral extension is strongly hampered in isotropic solution experiments. The large synthetic effort and insufficient solubility of the products are not the only factors affecting the negative outcome here.

One has to think in terms of the number of new bond-formation events that are required to extend an initially single-stranded polymer with, for example, 200 repeating units. Thousands of sequential transformations per molecule are required in a situation where any mistake cannot be healed.

Increasing attention has been devoted in recent years to this challenge and among the different proposed strategies, the most reliable one takes advantage of solvothermal reversible-bond forming conditions. In principle, all synthetic methodologies for covalent-bond formation developed in organic synthesis are of potential interest for the construction of organic polymers. However, in order to construct polymers with extended structural regularity and porosity, a self-adjusting mechanism is required to heal the defects formed during the growth of the sheet. Due to this reason, it is strongly believed that only reversible reactions are applicable for the possible construction of the so-called covalent-organic frameworks (COFs).

A series of reversible reactions that have been applied for the synthesis of these low dimensional materials is reported in Figure 5.

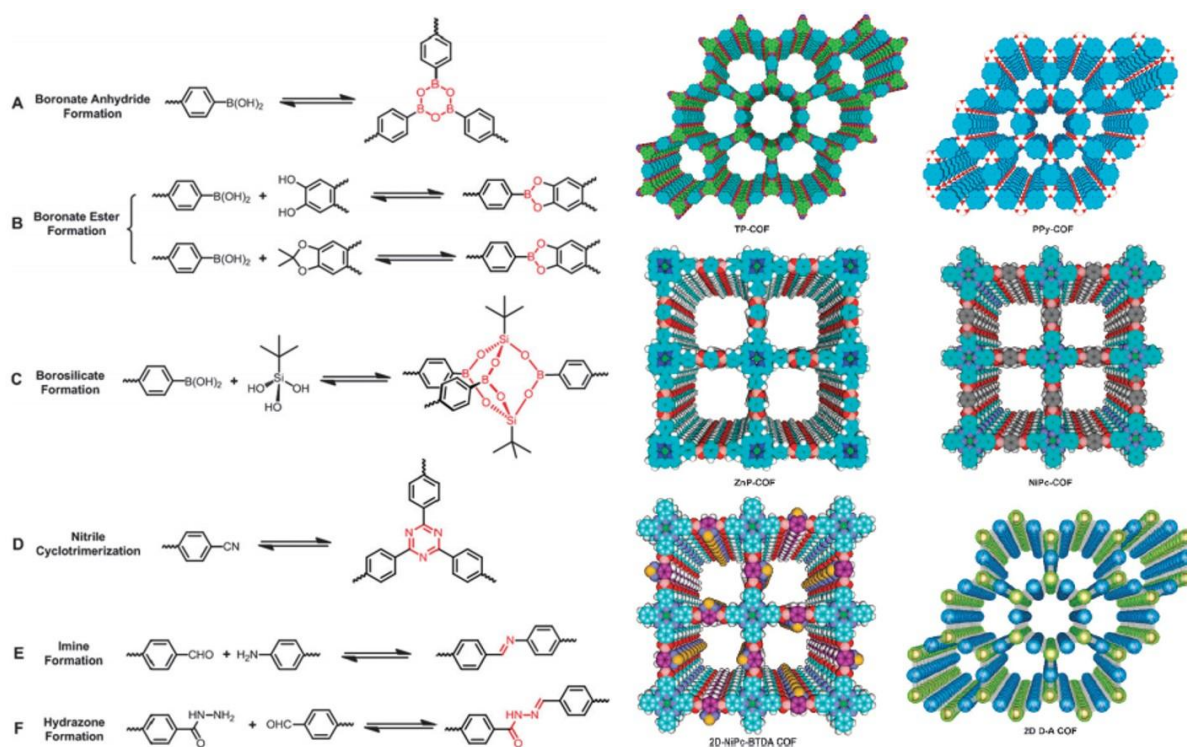


Figure 5: on the left, reversible reactions that have been successfully developed for the construction of COF materials. The covalent bonds formed through these synthetic routes are highlighted in red. On the right a schematic representation of the stacked structure of COFs is reported. Reproduced with permission from ref. ^[49] and ^[51], left and right image respectively.

COFs are layered periodic networks usually characterized by a long-range π -orbital overlap in the stacking direction, which gives rise to high exciton- and charge-mobilities of interest for optoelectronic devices.^[47–50] The layered structure generates 1D pores running parallel to the stacking direction, their dimension can be tuned simply by changing the size and length of the molecular building blocks and by providing the opportunity to produce series of designed COFs to optimize gas-adsorption properties^[51] and drug delivery.^[52] The addition of functional groups on their walls that can interact with gas molecules is an additional degree of freedom to develop new materials for the storage of specific gases. Hence it is not surprising that COFs have attracted interest for diverse applications.^[48] Their structural precision rivals that of designed supramolecular assemblies, yet they are robust, covalently linked materials. Despite these desirable features, COFs remain far from fulfilling their potential because they are typically isolated as microcrystalline powders of limited utility.^[53]

Interfacial approaches

Arranging monomers at liquid/gas,^[54,55] solid/gas, solid/liquid^[56] or solid/vacuum^[57,58] interfaces is of course an easy way to pay a large portion of the entropy price associated with the formation of 2D polymers. In these approaches, the confinement is achieved by spreading the monomers at liquid/gas interfaces, intercalating them into inorganic layered hosts, adsorbing them onto solid substrates, or letting them self-assemble into ordered structures. Cross-linking provides covalently connected ultrathin films, whose lateral extensions are orders of magnitudes larger than all those previously discussed. In this sense, the following approaches get substantially closer to the goal of a laterally infinite, one monomer unit thick and periodic structure. The first attempts to obtain 2D polymers were meant to covalently stabilize monolayers, such as surfactants or self-assembled monolayers, by means of cross-linking reactions, mainly with the aim of creating stable nanoporous membranes.^[59] Reactions such as [2+2] Diels-Alder cycloaddition, poly-condensations and topochemical diacetylene polymerization have been widely used to synthesize 2D object by UV-irradiation or e-beam activation.^[60–62]

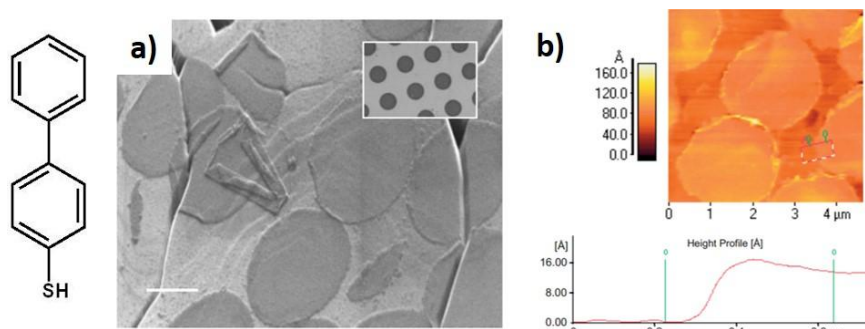


Figure 6: Production of a nanosheet by electron irradiation of 1,1'-biphenyl-4-thiol. A mask with circular holes was used to pattern the growth on a gold/mica substrate. **a)** SEM image of the resulting disk-like object after reduction by iodine vapour and rinsing in DMF/ultrasound. The inset shows the scenario before the aforementioned treatment. **b)** AFM image and height profile measured on gold. Reproduced with permission from ref ^[162].

The removal of the resulting monomolecular films from the different interfaces was achieved by horizontal lifting at the liquid/air interface, or etching-off the underlying substrate when working on a solid surface. However, since the cross-linking does not occur spatially uniformly, “glued and compressed” oligomers are obtained rather than ideal 2D crystalline materials that are characterized by translational symmetry in one plane. Despite the fact that crystallinity is not the strength of these strategies, the figure of merit is the huge lateral extension that is easily achievable: up to hundreds microns.

However, an approach wherein one needs only to spread the desired monomer onto a proper interface, activate the polymerization and take out a large 2D polymer, whose dimensions are proportional to the surface area of the interface itself, seems to easy to be realistic. In fact, unfortunately entropy complicates the picture, so that self-assembled structures usually consist of a patchwork of domains wherein both their relative orientation and the order may be different. Thus, even if an extended interface is employed, the size of the 2D polymer is then defined by the dimensions of such domains.^[63–65] It therefore appears that any interfacial polymerization of a compressed monolayer should ideally start with an analysis of the domain size and of the level of internal order. Polymerization only makes sense if both sufficiently large domains and long-range positional order are observed.

In summary, by these strategies it is possible to prepare monomolecular layers, but they do not yet allow to realize the dream of a truly single monoatomic graphene-like material. Structurally perfect 2D polymers are strictly required when dealing with the electronic structure engineering of the resulting material. Charge carrier conductivity, band gap opening and its size, energy level alignment (at the interface), catalytic

activity, etc... are all properties strongly dependent on the detailed atomic structure and connectivity of the network.^[66,67] Hence, to realize the dream of ordered mono-atomic sheets it might be necessary to take advantage of atomically controlled single-crystal surfaces, in order to control the structure of the self-assembled monolayer prior to polymerization, and to work in perfectly controlled ambient conditions, in order to avoid any impurities (dust or insufficiently purified monomers) that limit the domain sizes. This challenge is actually engaged by surface science in ultra-high vacuum environment (UHV). In fact, UHV conditions strongly reduce the presence of contaminants or side-reactions with the solvent and allow one to explore the reaction process on several different surfaces. The high control of the surface symmetry and corrugations, by choosing a proper cutting angle, greatly expands the possibility to explore fundamental reaction mechanisms and to control the system architectures by means of the templating effect. Moreover, the catalytic properties of the supporting substrate is an additional degree of freedom to tune the reactivity of the monomer. Finally, the combination of UHV conditions and surface science makes it possible to employ a powerful battery of experimental techniques that enables us to gain a deeper comprehension of the electronic and structural properties directly in-situ after the reaction or even in real time. Among them, scanning tunnelling microscopy (STM), X-ray photoemission spectroscopy (XPS) and low-energy electron diffraction (LEED) are only a few of the complementary available techniques. Despite the aforementioned advantages, these reaction conditions pose their own obstacles. The required reaction reversibility to heal the defects formed during the growth does not work in UHV conditions due to the lack of an effective exchange equilibrium with the solvent. In fact, in these conditions, all the covalent bond formation events are irreversible and once formed they remain stable. Another difficulty is how to get rid of the supporting material in order to decouple the electronic properties of the created structure from those of the substrate. A couple of techniques are known for the lift-off process that requires either a harsh chemical or electrochemical treatment, with or without an ultrasound treatment. Alternatively, the substrate can be etched away with hydrofluoric acid.^[60] Obviously all these conditions may work only for chemically inert materials. Finally, the starting precursors have to survive to the required preparation conditions such as in-vacuum deposition and high temperature treatments, usually required to activate the reactive sites.

On-surface chemistry is a very recent research area and relatively few studies have been published to date. This limited number indicates that novel reaction types and consequently novel reaction paths have to be explored, in order to prepare complex but ordered surface-supported structures.

The aim of this work is therefore clear: introducing new on-surface reactions to covalently link single functional molecules on metallic supports, thus contributing to the ongoing intense research efforts aimed at the production of robust architectures synthesized on solid surfaces. Along this line, the photochemical and thermal reactivity of selected precursors is investigated by means of ultra-high vacuum surface-sensitive techniques.

On-Surface Synthesis

The self-organization of simple precursors into complex and order structures has recently attracted the attention of many research groups.^[68] Self-assembly is at the basis of the “bottom-up” manufacturing strategies, by which the final (desired) network is obtained starting from a carefully designed precursor. The idea is to equip the monomer with proper functionalities in order to exploit various non-covalent intermolecular interactions (hydrogen bonds, π - π stacking, van der Waals, ...) ^[69,70] along well-defined directions. One can thus easily realize that if a planar monomer carrying three functional groups at 120° from each other is used, the resulting supramolecular assembly will be a net with hexagonal pores. Differently, if the same planar monomer carries four groups at 90° , the net will have square pores.

In the speculative vision of nanotechnology, microchips, transistors and other circuitry components of the future will be produced by molecular self-assembly.^[71,72]

An advantage of this method is that one has only to care about the shape and the functionalization of the molecular precursor and then the system will thermodynamically evolve towards the supramolecular system. Due to the reversible nature of the intermolecular interactions, defects are self-healed, but from the applicative point of view such intrinsic instability is not suited to build-up real devices. Covalent connection among the different sub-units is thus needed in order to increase the mechanical stability of these systems.

An ideal stabilization process will polymerize the building blocks once they are pre-organized in the desired assemblies. However, despite the numerous attempts to get 2D polymers in UHV conditions, only in few cases this approach has been actually applied.^[73–75] The problem is that usually the functional groups used to drive the network formation act also as leaving groups for the subsequent stabilization. As an example, the R-COOH functionalization can drive the network formation through intermolecular hydrogen bonds as well as R-X (X=Br, I) groups by halogen bonds, but once they are thermally activated (producing leaving groups such as CO₂ and X-surface-stabilized radicals) the network formation requires the contraction of the distances between adjacent monomers. Since there are generally no reasons for this movement to take place in a coordinated manner, the formation of an ordered network on the micrometer scale is highly unlikely. The formation of defects is not an

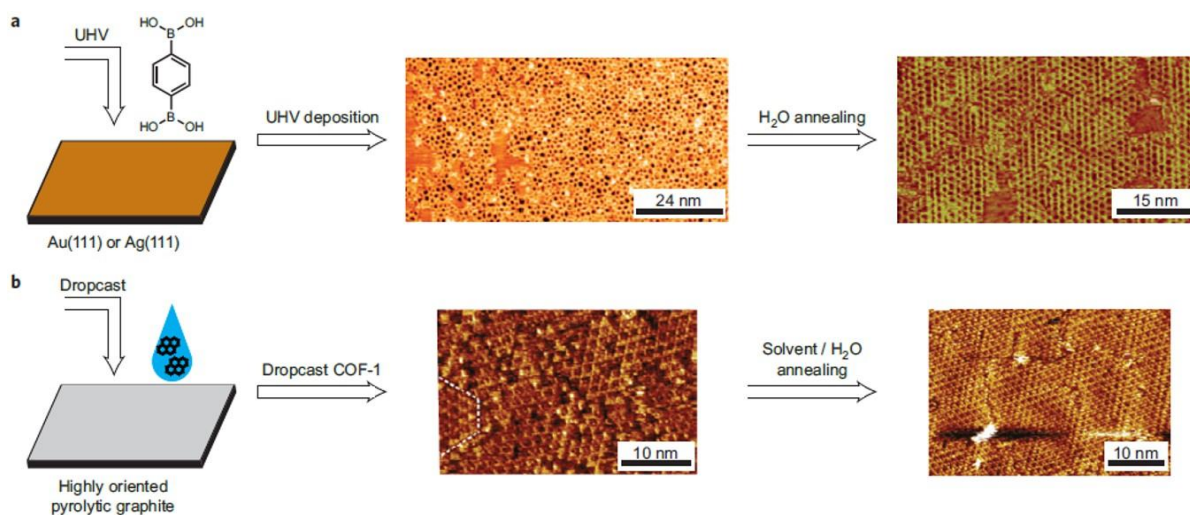


Figure 7: **a)** BDBA self-condenses onto crystalline metal surfaces following UHV deposition. After annealing, the STM image (middle) shows formation of the COF monolayers containing various 5- and 7-membered ring defects. Annealing this film in a humid environment strongly improves the order of the film (right). **b)** dropcast synthesis on to HOPG (middle). A similar annealing as in a) provides a monolayer with high long-range order (right). Reproduced with permission from ref ^[53].

issue if the reaction is carried out in reversible conditions because the dynamic equilibrium will lead, over the time, to heal these irregularities. However, this reversibility cannot be obtained under ultra-high vacuum conditions, wherein each covalent bond formation event is an irreversible process. Consider as an example the condensation reactions, such as the boronic acid or imine formation, which are reversible in solution. 1,4-benzenediboronic acid (BDBA) was sublimated in UHV by La Porte and coworkers^[76] on Ag (111) and, once the dehydration reaction has been activated by a thermal treatment, the resulting boroxine-linked network was highly defective. As can be seen in Figure 7, the 2D polymer is composed of pentagons, hexagons, heptagons and vacancies. Later studies by the same group have been devoted to determine the best reaction conditions.^[77] The growth of the polymer has been optimized on several surfaces, namely Cu(111), Ag(111), Ag(100) and Au(111), but despite the possibility to partially improve the long-range order by optimizing the rate of deposition and the annealing temperature, a crystallinity comparable to that of graphene is not obtainable. The reason is simple: small molecules are released as products of the condensation reactions –water in the present case– that immediately desorb from the surface, disabling the self-repairing process. In fact, if the disordered polymeric structure is extracted from UHV and annealed in a humid environment, the order of the film can be significantly improved.^[78,79] The same conclusions apply to analogous reactions including the formation of imines,^[80] which is a promising

process to obtain COFs but, again, in UHV conditions does not allow to achieve similar results.^[81,82]

The question that spontaneously arises is then: why has one to work in vacuum wherein the defects cannot be cured? Is it not easier to work at the solid-liquid interface in order to achieve the needed microscopic reversibility? Firstly because the absence of the solvent allows to explore a greater range of temperatures, limited only by the stability of the precursor itself, and therefore to take advantage of new reaction schemes which are not observed in solution. As an example, dehydrogenation reactions are widely used in solution to obtain large planar polyaromatic hydrocarbons by means of Lewis acids. However, at metal/vacuum interfaces the same reaction can be easily applied to synthesize both 0D objects, such as fullerenes,^[83,84] and 1D and 2D polymers. The regio-selective coupling of long alkane chains on Au(110),^[85] the bidimensional phthalocyanine networks obtained by means of the Huijens reaction^[86], as well as the surface-assisted dehydrogenative homocoupling of porphine molecules^[87] are some examples of what the vacuum offers. Moreover, post-synthesis treatments enable the exploration of peculiar conditions, such as the intercalation of atomically thin insulators (NaCl) underneath the covalent network,^[88,89] and to obtain products not obtainable in solution, such as the on-surface metalation of porphyrin macrocycles.^[90–92] Last but not least, UHV allows one to combine multiple complementary techniques in situ, directly on the as-prepared sample, without the need to take it out of vacuum and thus avoiding further contaminations. Microscopy (STM and STS) allows to probe and to control the structure of the sample with atomic resolution and to measure the electronic properties, the conductance, the density of states, of single molecules. Differently, synchrotron based techniques (XPS, NEXAFS, ARPES) give access to surface-averaged data like molecular orientation, stoichiometry and oxidation states of the compounds, to the band structure of conjugated polymers (filled states) and can also sample their empty electronic states.

To date, on-surface coupling has been activated mainly through three different methods: heat treatments, light stimuli and bias-pulses by the STM tip.^[57,93,94] Apart from the latter, which does not seem promising for up-scaling, the first two will be discussed in the following sections. Although over the years, several reactions have been adapted from the solution to the solid/UHV interface, only the more promising ones and those that gave significant results will be reported.

Thermal Activations

In case of thermally activated reactions, the precursor can be either deposited on the surface maintained at low temperature and then heated, or sublimed onto a substrate kept at high temperature. Although the differences between the two methods are strictly dependent on the type of reaction, deposition flux, metal and precursor used, deposition on a hot surface appears to give better results. In fact, starting from a completely covered surface by unreacted monomers and then heating it, the relatively high temperatures usually required may lead to the activation of secondary processes such as desorption and decomposition,^[95,96] especially if the precursor is thermolabile. Therefore, a gradual activation usually leads to a less covering layer with respect to those obtained by sublimating directly on the hot surface.^[97] Once again, these differences are particularly dependent on the system studied, as much as the crystallinity of the obtained polymer is related to the molecule / substrate combination.

The thermal treatment is the simplest way to provide sufficient energy to the reactants to overcome the activation barrier for the desired reaction. As adaptations of processes that take place in solution, several reactions have been tested in UHV conditions such as esterification,^[98] addition of isocyanates^[99,100] and cyanates to amines, formation of imines,^[81] imides,^[101,102] amides from acyl halides^[103,104] and click-reactions.^[105] However, the absence of the solvent also allows the usage of other processes that in solution would not provide similar results: the homolytic dissociations. Any book of general chemistry reports tables of the average bond enthalpy.

Average Bond Enthalpies (kJ/mol)							
Single Bonds							
C—H	413	N—H	391	O—H	463	F—F	155
C—C	348	N—N	163	O—O	146		
C—N	293	N—O	201	O—F	190	Cl—F	253
C—O	358	N—F	272	O—Cl	203	Cl—Cl	242
C—P	485	N—Cl	200	O—I	234		
C—Cl	328	N—Br	243			Br—F	237
C—Br	276			S—H	339	Br—Cl	218
C—I	240	H—H	436	S—F	327	Br—Br	193
C—S	259	H—F	567	S—Cl	253		
		H—Cl	431	S—Br	218	I—Cl	208
Si—H	323	H—Br	366	S—S	266	I—Br	175
Si—Si	226	H—I	299			I—I	151
Si—C	301						
Si—O	388						
Multiple Bonds							
C=C	614	N=N	418	O ₂	495		
C≡C	839	N≡N	941				
C=N	615			S=O	523		
C≡N	891			S=S	418		
C=O	799						
C≡O	1072						

Table 1: Average Bond Dissociation Enthalpies in kJ per mole.

This quantity refers to the change in enthalpy associated with the homolytic dissociation of the particular bond in the gas phase, averaged since it is mediated on various compounds.

It is therefore clear that it is possible to activate the dissociation of a particular class of bonds by simply providing enough thermal energy. Obviously, table 1 has to be read with care, since the exact temperature that has to be reached experimentally depends on the employed molecule, on its bonding scheme (e.g. whether there is electron delocalization) and on the used surface, i.e. on the catalytic activity of the metal. Consequently, a couple of radicals is formed and they will diffuse on the surface ready to bind with similar species in order to saturate the coordination. This kind of approach seems to be more promising than substitution/addition reactions, as proved by the higher number of publications devoted to it. As stated before, even for these reactions, the C-C bond formation is an irreversible process, but it occurs on the metal surface with an intermediate organometallic network that is relatively stable, isolable and characterisable in a defined temperature range (except for the reactions on gold). Compared to covalent linking, coordination and organometallic bonds have the advantage that bond formation is reversible, and therefore, defects in the translational symmetry can heal through bond scission and reformation. At higher temperatures, the metal atoms are released and carbon-carbon bonds are formed. Since the formation of carbon-carbon bonds thus passes through a reversible intermediate state, it should in principle be possible to obtain well-ordered covalent structures, albeit previous attempts in this direction were not particularly successful.

Ullmann coupling

Ullmann coupling is the most applied C-C coupling reaction and several studies have been devoted to characterize the influence of the reaction conditions, the mechanism and the electronic properties of each intermediate. As for other reactions, this one has been successfully applied in solution to bind aryl halides in the presence of finely divided copper.^[106,107] Hence, it appears reasonable that the reaction has been tested initially on copper surfaces.

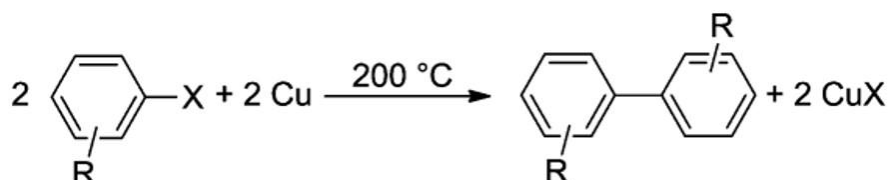


Figure 8: Diagrammatic representation of Cu-mediated Ullmann-coupling between two aryl halides.

In 2000, Meyer et al.^[108] have sublimated iodobenzene molecules on a Cu(111) at low-temperature and STM was used to step-by-step characterize the coupling. Pulses were used to selectively dissociate the C-I bonds of two adjacent molecules adsorbed at the step edge and then, by dragging and pulsing again, the biaryl product was synthesized in real time. Only later, Grill and coworkers^[109] have published a ground-breaking work showing the capabilities of this reaction to produce 1D and 2D networks. Functionalized tetra-phenyl porphyrins were used in that case. Nowadays, the Ullmann coupling is a widely applied way to tailor the synthesis of 1D and 2D nanostructures and its applicability has been proven on several different metal surfaces beyond copper.^[110] The reaction is extremely versatile, since the topology of the covalent structure is defined only by the substitution pattern of the precursor. Hence, 1D polymers are fabricated from two-fold halogenated building blocks, whereas if the monomers carry three or more halogen atoms a 2D network is obtained.

Reaction mechanism

The initial step of the on-surface Ullmann coupling is the dissociation of the heteroatom from the monomer. Looking at table 1, dissociation of carbon-halogen bonds (I, Br and Cl) needs lower energy than required for the C-C ones. These energy differences allow the selective dissociation of the weaker C-X bond without affecting the molecular scaffold. Hence, this reaction starts with an initial scission of

the carbon–halogen bond, followed by the reversible formation of intermediate metastable carbon–metal–carbon bonds (C–Me–C), the so-called “protopolymer”.^[111,112] In a second reaction step, at higher temperature than the

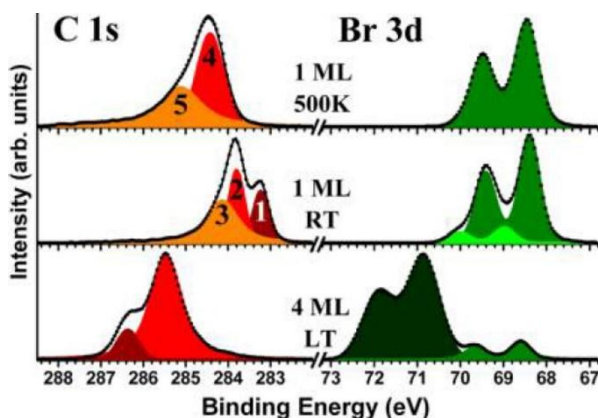


Figure 9: C 1s and Br 3d core level spectra acquired at different stages of the synthesis of polyparaphenylene chains on Cu(110) from p-dibromo-benzene: bottom 4 monolayers deposited at LT, middle 1 ML deposited at RT and top the same surface annealed at 500 K. Adapted with permission from ref. ^[115]. Copyright 2013 American Chemical Society.

brominated molecules, both the 3p and 3d levels (Br 3p_{3/2} = 184.2 eV, Br 3d_{5/2} = 69.9 eV, from measurements on multilayers at low temperature) show a significant shift (2 eV) towards lower binding energy once the first reaction step is activated.^[95,114,115] The direction of the shift toward lower BE is consistent with an increased electron density at the Br atoms, as would be expected by the formation of a bromide-like species. On Cu and Ag the area subtended by the initially carbon-bonded bromine is about the same of that of the chemisorbed species, indicating the quantitative retention of the species on the surface.^[114,116] Differently, on Au the reduction of the total subtended area (partial desorption) of the halogen is observed simultaneously with the dissociation, due to the lower binding energy of Br to gold.^[117–119] Although in principle the same behaviour could be expected for the C 1s feature, the situation is more complicated than one might think. In fact, even if the molecule contains inequivalent carbon atoms, C 1s is commonly observed as a single unresolved peak. Accurate deconvolutions, taking care of the stoichiometric constraints imposed by the molecular structure, are then needed to follow the evolution of individual

former, the metal atoms are released leading to the formation of a true organic polymer.^[95,113] Noble metal surfaces, Cu, Ag and Au, show some differences in the reaction steps due to different catalytic activity and the next section will deal with this issue.

Each reaction step can be experimentally characterized both by microscopy and by spectroscopy techniques. From the latter point of view, X-ray photoelectron spectroscopy (XPS) provides important information, since the binding energy of the core levels is a fingerprint of the oxidation state of the species under consideration. If we take the example of

components.^[115] If we consider the C-Br component, a shift toward lower binding energy is observed due to the replacement of a very electronegative (Br) species with a softer (metal atom). However, not only this component but also the entire C 1s peak moves gradually in the same direction.^[114,119] The low-BE shift of the C 1s peak can be explained by a coaction of two factors: firstly, adsorbed Br atoms are known to increase the work function of the metal. If the organic backbone of the molecules interacts with the surface mainly via van der Waals forces, the appropriate reference level for the molecular states is the vacuum level. In such situation, the Br-induced work function increase causes a C 1s peak shift to lower BE, as observed. Secondly, the metal atoms in the organometallic network are at a short distance from the surface and thus pull-down the molecular backbone. The reduced distance between the adsorbate and the metal surface is expected to allow for a more efficient screening of the core hole leading to a shift towards lower BE. Thus, photoemission data have to be handled with care.

Even though microscopy techniques provide extremely localized information, the C-X bond dissociation event is easily identifiable.

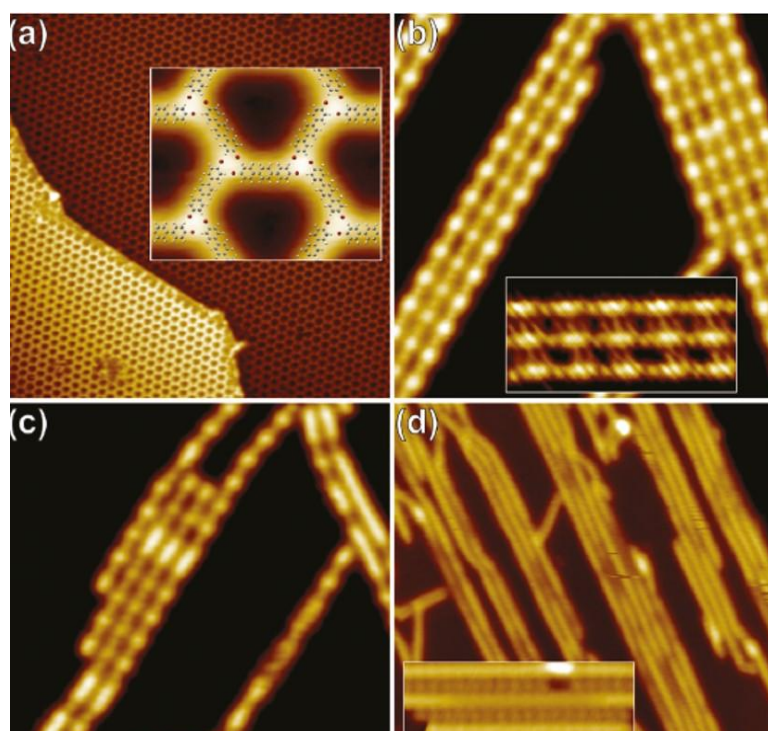


Figure 10: Series of STM images acquired during the synthesis of poly-paraphenylene chains on Cu(111). **a)** self-assembled precursors at 77 K, **b)** organometallic network formed after annealing at 300 K, **c)** annealing at 393 K causes the partial release of some Cu adatoms, leading to the formation of poly-paraphenylene oligomers, **d)** the C-C coupling is completely activated after annealing at 473 K. Adapted with permission from ref. ^[123]. Copyright 2011 American Chemical Society.

Simultaneously with the core level shift of the halogen, STM shows significant variations in the surface structure. In fact, the non-reacted precursors, before annealing, organize in order to optimize the lateral interactions by mean of halogen bonds and they lie in vortex or staggered geometry.^[120,121] On the other hand, the organometallic bond requires a linear geometry.^[122] Therefore, a phase transition between two ordered structures is observed contextually to the activation of the C-Br dissociation.^[123] The inserted metal appears as a bright protrusion that connects two precursors, and the centre-to-centre distance is generally accepted as a tool to prove the formation of the organometallic structure. Since the metal acts as a bridge between two organic molecules, distances greater than those expected (DFT modelling) for direct coupling are commonly observed.^[124,125] However, this method is an indirect way to prove the presence of the metal, and for this reason scanning tunnelling spectroscopy (STS) and DFT simulations have been used to highlight the different nature of the organic part and the metallic junctions.^[123,126] The comparison of the probed density of states measured at different points along the network with that predicted theoretically further corroborates this mechanism.

The second step of the synthesis, the C-C bond formation, has been characterized by using arguments similar to those reported before. Photoemission reveals that the C 1s peak shifts back to higher BE:^[114,115,119] the release of Me atoms from the C-Me-C bonds and the formation of C-C bonds increase the average distance between the organic backbone and the surface. By applying the same argument as above, this leads to a less efficient screening and thus to a shift towards higher BE. Even the shape of the peak changes due to the transformation of the C-Me into a C-C component. Differently, halogen signals are not affected by this treatment, and only a partial desorption is observed on Cu and Ag. STM, instead, provides a more interesting point of view. The release of the metal causes the contraction of the centre-to-centre distances between the monomers and the molecules are observed with a more uniform intramolecular contrast, i.e. without internal bright protrusions.^[116,127,128] Finally, the long-range order of the 2D polymers get worse at this stage.^[95,110] Holes, under-coordinated monomers, side-reactions and irregular closures are the result of the irreversible reaction condition.

Role of the metal surface

In addition to the dependence on the halogen type, as reported in table 1, the on-surface synthesis by Ullmann coupling also depends on the catalytic properties of the substrate. In fact, the surface not only acts as a support, constraining the molecular motion into 2D, but also reduces the temperature required for the reactions. Recent DFT calculations have highlighted the main differences among the (111) facets of Cu, Ag and Au.^[129,130] Depending on the material, the lower the catalytic activity of the surface, the higher the temperature at which the splitting of halogen atoms occurs. Hence, dehalogenation is most favourable on Cu(111) and least on Au(111), as summarized in table 2.

Substrate	Debromination			Deiodination		
	E_{react} (eV)	E_{barrier} (eV)	Status (RT)	E_{react} (eV)	E_{barrier} (eV)	Status (RT)
Cu(111)	-0.68	0.66	complete	-0.81	0.40	complete
Ag(111)	-0.50	0.81	partial	-0.67	0.52	complete
Au(111)	-0.16	1.02	no	-0.44	0.71	complete

Table 2: DFT calculated reaction energy and energy barriers for the dehalogenation process on noble metal surfaces. The commonly observed status of the C-X dissociation process at RT is also reported.

The formation of the covalent nanostructures is governed by the reaction between surface-stabilized radicals, so that even the second step is metal-sensitive. The simulated path for the coupling of two phenyls into biphenyl as well as the associated energy diagram are reported in Figure 11. As visible, the recombination process is highly exothermic on all surfaces, but different metals show different energy barriers between the final and the initial state. This barrier is more or less non-existent for Au(111) (<0.01 eV) and rather small on Cu(111), while it is largest for Ag(111). However, on gold one has to spend 0.25 eV to bring two well-separated phenyls to the intermediate state.

From a theoretical point of view, a large recombination barrier, coupled

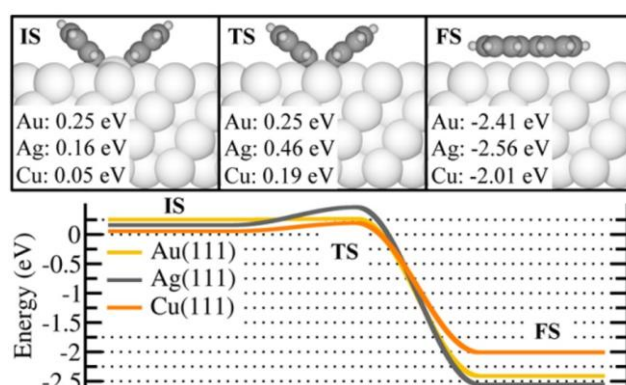


Figure 11: DFT calculated energy diagram for the coupling of two surface-stabilized phenyls into biphenyl on Cu(111), Ag(111) and Au(111). The top panel reports the geometrical structure of the initial (IS), transition (TS) and final state (FS). Adapted with permission from ref. ^[129]. Copyright 2013 American Chemical Society.

to a small diffusion barrier, is beneficial for self-assembly of regular 2D networks.^[130] In fact, the activation barrier avoids a fractal-like growth mode, that leads to rather defective structures, and favours the occupation of sites with higher lateral coordination if the monomers can easily diffuse. For these reasons, judging from theoretical predictions, Ag(111) seems to be the most promising substrate, but the experimental trend does not seem to be well defined.

The conversion of organometallic into carbon-carbon bonds requires a higher temperature annealing than the first reaction step. On copper and silver surfaces the temperature is usually close to 180-250°C^[95,110,116] and it is not always possible to reach this value due to stability problems of the precursor. Differently, on gold the organometallic network is not commonly observed, so that once the C-X bond is activated, the direct formation of the covalent network is observed.^[97] Exceptions are sterically hindered molecules.^[112,131]

Homo-coupling of terminal alkynes

Among the various allotropes of carbon, some have been theorized, whose existence has yet to be proved. Two of these species are two-dimensional materials known as graphyne and graphdiyne, which are considered promising alternatives to graphene. These crystalline sheets can be regarded as carbon polymers and a retrosynthetic analysis can be carried out in this sense. Moreover, much like with graphene, various one-dimensional counterparts, such as nanoribbons or nanotubes, can be drawn by cutting the graphyne and graphdiyne sheets along particular directions. Even these systems are of particular interest and significant efforts were devoted to theoretically characterize their properties.^[132]

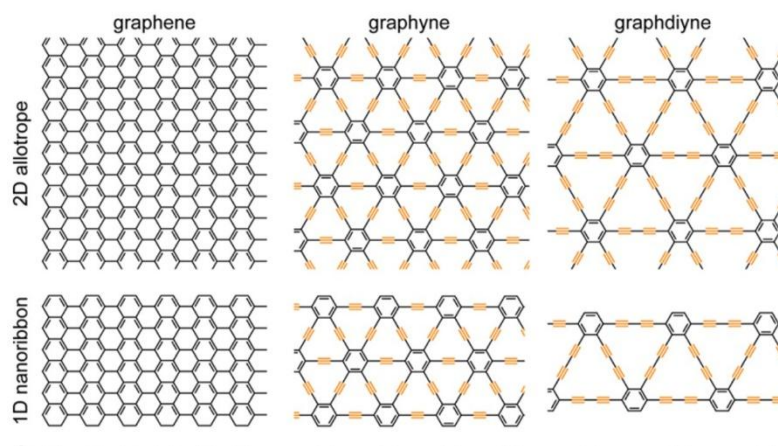


Figure 12: chemical structures of 2D carbon allotropes and related nanomaterials. The sp-hybridized carbon atoms are highlighted in orange. Adapted with permission from ref. ^[132]. Copyright 2015 American Chemical Society.

The emerging field of on-surface synthesis is tackling this challenge, and in particular the coupling of terminal alkynes seems to be promising. The demonstration of the synthesis of covalent nanostructures obtained from the coupling of terminal alkyne was achieved in 2012.^[133] Zhang et al. have sublimated two tritopic precursors (1,3,5-triethynyl-benzene (TEB) and 1,3,5-tris(4-ethynylphenyl)benzene) on Ag(111) and upon increasing the temperature dimers and fully reticulated covalent networks evolved, locally formed by hexagonal pores. However, long range order was missing due to the formation of pentagons and heptagons and to the occurrence of spurious side reactions. Differently, on Au(111) the same monomers are engaged in cyclotrimerization reactions that lead to the expression of regular domains.^[134,135] These results suggest that by changing the nature of the substrate, the preferred coupling type of the terminal alkyne can be steered.

Reaction pathway

Although it may seem intuitive that the reaction proceeds via dehydrogenation of the terminal carbon followed by the coupling of the surface-stabilized radical, DFT calculations reveal a different scenario.^[132]

There have been two independent reports about the reaction mechanism and the common main message is that the coupling starts with the reaction between two end groups, followed by twofold dehydrogenation of the generated intermediate.^[136,137] The latter is stabilized by chemisorption to the metal surface, and the dehydrogenation processes may be associated with a homolytic mechanism. The alternative path, i.e. the initial dehydrogenation, with TEB on Ag(111), has a barrier about twice as large as the energy needed to induce a coupling reaction. Moreover, even if dehydrogenation occurs in some way, these interfacial species will couple less effectively to each other than intact molecules since their barrier exceeds by roughly 0.3 eV that of the latter. Finally, concerning the different reactivity on Au(111) with respect to Ag(111), the underlying reasons are still unclear due to the rather limited theoretical insight into the mechanisms.

Decarboxylation of organic acids

Metal-catalysed polymerization of 2,6-naphthalenedicarboxylic acid (NDCA) is an important achievement in the on-surface coupling research field.^[138] By adopting carboxylic groups for the synthesis of polymeric materials, it offers the opportunity to easily design the organization of the monomers, through the hydrogen bond

interactions, and thus, to steer the growth of the covalent layer. This is a particularly powerful strategy if the carboxylic groups are used in the presence of other functional groups in order to exploit a sequential and selective activation (hierarchical approach).

As a model system, C-C coupling of NDCA was compared on three noble metal surfaces^[138] and it was found that on Au(111) the reaction seems not to proceed, while on Ag and Cu the heating treatment results in the formation of long 1D polymers. Three reaction steps can be identified as the surface temperature is gradually increased: the first is a dehydrogenation process to provide the corresponding metal carboxylate, then the decarboxylation takes place and the formation of polymeric bis-naphthyl-metal chains is observed (protopolymer). Finally, as for the Ullmann coupling, the metal adatoms are released leading to the C-C coupling.

Dehydrogenation reactions

C-H bonds are by far the functional groups most abundantly present in organic molecules. Hence, the controlled activation of some C-H bonds can lead to new promising synthetic pathways. Dehydrogenation and cyclo-dehydrogenation reactions are commonly employed in heterogeneous catalysis, especially in combination with the outstanding properties of platinum in activating the C-H bond.^[139,140] Thus, a large number of small polyaromatic hydrocarbons have been initially studied on the Pt(111) surface in order to obtain 0D objects such as fullerene, aza-fullerene and triangular-shaped nano-graphene.^[83,141]

One of the most important applications of the cyclo-dehydrogenation processes is by far the topologically controlled growth of atomically precise graphene nanoribbons: chevron type and linear armchair nanoribbons can be easily synthesized from halogenated polyanthrylene precursors.^[142] Intermolecular coupling has been also reported to take place on noble metal surfaces. Amabilino et al.^[143] demonstrated a surface-assisted radical homocoupling of tetra(mesityl)porphyrins on Cu(110), Gade and coworkers^[144] have shown the synthesis of 1D wires from 1,3,8,10-tetraazaperopyrene, while on Ag(111) the homocoupling of free-base porphyrines by thermal activation results in the formation of a variety of dimers and larger oligomers.^[87] More recently, dehydrogenative coupling and Ullmann coupling have

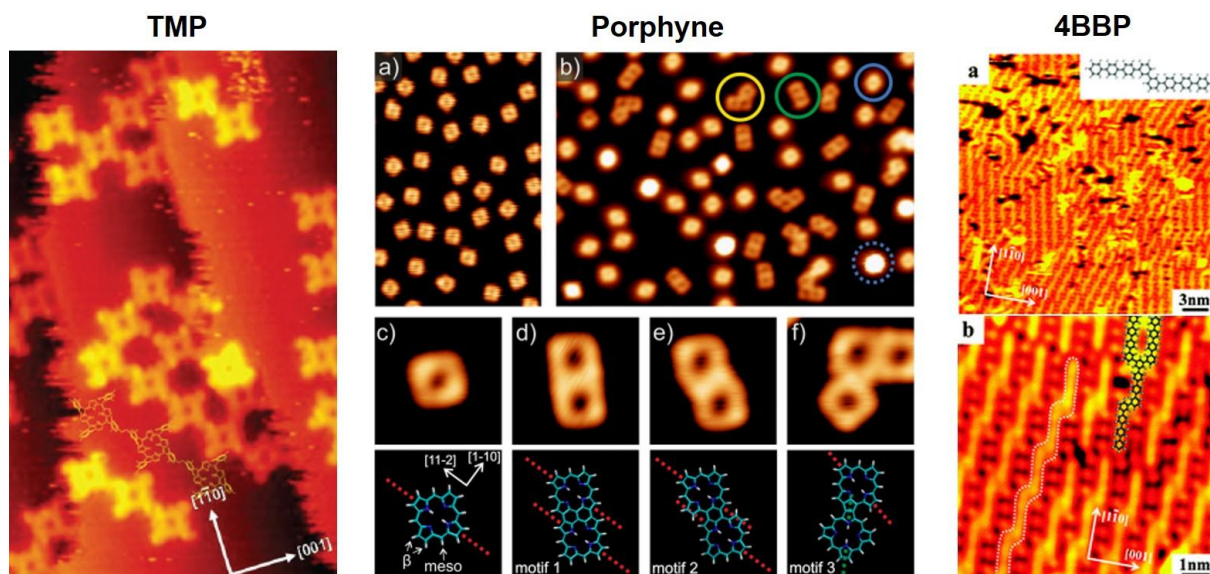


Figure 13: some of the products obtained by on-surface dehydrogenative intermolecular coupling are reported. **Left:** 2D network obtained on Cu(110) from tetra(mesityl)porphyrins (TMP), **middle:** porphyrine homocoupling on Ag(111), **right:** hierarchical synthesis of polyparaphenylene chains on Cu(110) from 4-bromobiphenyl (4BBP). Reprinted with permission from ref. ^[143] (left), ^[87] (centre, Copyright 2014 American Chemical Society) and ^[145] (right).

been applied sequentially to produce small 2D object from 4-bromobiphenyl.^[145] This study is relevant because it shows the ability to perfectly separate the reactivity of the C-Br sites from the C-H one.

However, the small H atom is difficult to be detected experimentally and these types of reactions are undetected by STM and hardly followed by photoemission techniques. Hence, temperature programmed desorption (TPD) appears to be the most suitable technique to follow dehydrogenation in-situ in UHV conditions.^[146]

Photochemical activation

Mild reaction conditions able to preserve the initial self-assembled structure of the unreacted monomers are of paramount importance when the goal is to achieve ordered covalent structures. To this end, photons are a promising alternative to the heating treatments. Indeed, molecular mobility is strictly related to the substrate temperature by the relation:

$$D = D_0 \exp\left(-\frac{E_{\text{dif}}}{RT}\right)$$

where D is the diffusion coefficient, D_0 the diffusion prefactor, E_{dif} is the activation energy for diffusion, R is the ideal gas constant and T is the temperature. By using a light source with a power density on the surface lower than 100 mW/cm^2 , thermal effects are mainly avoided, so in principle it is possible to trigger the reaction without affecting the surface dynamics. One of the most attractive aspects of this method is the possibility to leave the overlayer lattice parameters nearly unchanged if in the starting superstructure the reactive functional groups are properly oriented. Various experiments have shown the power of this method by using the topochemical polymerization of diacetylenes, see Figure 14. Ozaki et al.^[53] demonstrated a 2D polymerization within a crystalline monolayer with an alkyne containing monomer.

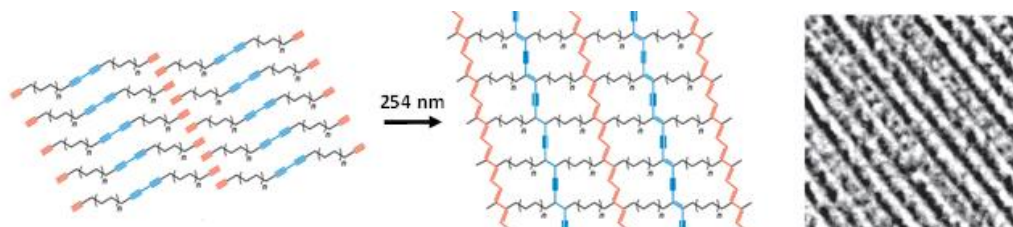


Figure 14: Irradiation of alkyne-containing monomers induces simultaneous topochemical polymerizations that yield a 2D polymer comprising linear polyacetylene and polydiacetylene chains linked by alkanes. STM image of the resulting polymer is also shown. Adapted with permission from ref. ^[53].

Analysis by STM indicated that both the internal diyne and terminal alkyne moieties were aligned appropriately for topochemical reaction and a perfect 2D network was obtained as a result of UV irradiation, in which the lattice parameters were nearly unchanged from the monomeric form. This example shows that a proper design of the molecular building block is the key of an efficient polymerization and the result is also the first known true covalently linked 2D polymer. Although covalent bonds can be formed in many ways by photochemistry in solution, there are very few studies of their application in this field. Hence, in this work we report our results on the optimization of a set of reactions for the realization of regular molecular networks

held together by relatively strong covalent bonds formed by photochemical reactions at sub-monolayer level.

A little bit of theory²

Physisorption of molecules on surfaces induces changes in their electronic properties that can lead to a strongly modified reactivity; this is the basis of many surface effects, notably of heterogeneous catalysis. Reactivity is also possible between electronically excited states of molecules, which is the basis of photochemistry. Even these excited states will be modified by the coupling with the substrate and the induced changes include, in addition to more or less subtle changes of the energy levels position, the possibility to exchange charge and energy between the molecules and the substrate via the latter's surface.

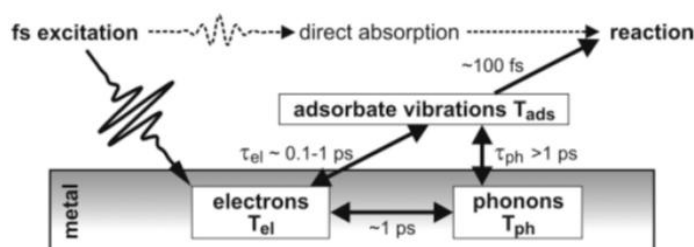


Figure 15: Schematic diagram of the energy flow at a metal surface after femtosecond-laser excitation. Time scales of energy exchange among various subsystems are also shown. While direct absorption in the adsorbate can be neglected in thin atomic or molecular layers, the laser radiation excites the electronic system of the substrate, which then equilibrates with the lattice phonons. Adapted with permission from ref. ^[151]. Copyright 2006 American Chemical Society.

This is particularly important on metal surfaces in which the typical quenching time lies between 10^{-15} - 10^{-13} s, depending on the character of the relaxation process.

Characteristic fluorescence and phosphorescence times are 10^{-9} s or longer, so they are strongly attenuated on metallic surfaces. On the other hand, rapid bond cleavage could compete with substrate relaxation because characteristic dissociation times along repulsive potential energy curves as short as 10^{-13} to 10^{-14} s. The adsorbate/metal coupling can be described generically in terms of charge and energy transfer processes initiated by photons interacting with metal-based electronic states. Thus there are two possibilities for photon absorption: (1) by the adsorbate or adsorbate-substrate complex, and (2) by substrate excitation. Figure 15 illustrates the energy flow among the different subsystems and gives characteristic time constants for the respective energy transfer.^[147-150]

² This section has been adapted with permission from ref. ^[147].

Processes driven by direct excitation

If the initial excitation takes place strictly within the adsorbate, the wavelength response should follow that of the gas-phase or condensed phase adsorbate molecule. In a single particle formulation, the excitation rate (R_{if}) between the initial (ϕ_i) and final state (ϕ_f) is given by Fermi's Golden rule:

$$R_{if} = \left(\frac{4\pi^2}{\hbar} \right) |\langle \phi_f | \hat{\mu} | \phi_i \rangle|^2 \delta(\Delta E_{if} - \hbar\nu)$$

where \mathbf{E} is the electric field vector; $\boldsymbol{\mu}$ is the transition dipole moment vector; ΔE_{if} is the energy difference between the initial and final state; $\hbar\nu$ is the photon energy; and e and m are electron charge and mass. The δ -function enforces the resonance requirement, that is $\Delta E_{if} = \hbar\nu$. One good example for a weakly held adsorbate is the photolysis of $\text{Mn}(\text{CO})_6$ on Si(111), graphite, Cu(111) and Ag(111) where the wavelength dependence correlates qualitatively with that in the gas phase.^[147] Generally, however, we cannot neglect the substrate. The presence of a metal surface induces perturbations in the electronic structure of the ground- and the excited-state adsorbate, even when the adsorbate is weakly held. Transitions involving these levels are broadened and shifted by as little as 0.1 eV to as much as 1 eV.

The role played by direct transitions is mostly established for photochemistry on insulators rather than on metals because, using UV light, single photon substrate excitation does not occur. On metals, one can never escape from substrate excitation, at least for thin adsorbate overlayers; such layers are optically thin and all metals readily absorb UV light. Nevertheless, there are numerous instances where direct absorption occurs; most of the evidence is for photochemistry occurring in the second and higher layers. There are few monolayer-on-metal cases where there is good evidence for direct excitation such as metal carbonyl, phosgene and diiodomethane.^[147]

Processes driven by substrate excitation

The excited substrate electrons play an important role in surface photochemistry at adsorbate/metal interfaces. These electrons can be divided into two categories: those that have and those that have not sufficient kinetic energy to surmount the measured work function at the vacuum/solid interface. For low energies, typically produced by ultraviolet and vacuum ultraviolet radiation, ionization is not possible. It is possible to consider the substrate-mediated surface photochemical process as

comprising three distinct and time-separable steps: (1) the optical excitation of electrons in the bulk substrate; (2) the migration of excited electrons and holes through the crystal lattice to the surface and (3) the transfer of these excited electrons or holes to the adsorbate to form an excited state. The incident photon pulse excites a non-equilibrium continuous distribution of hot electron with energies in the range $E - E_F = 0 - 1.55$ eV where E_F is the Fermi level of the substrate. This is demonstrated in 2-photon photoemission (2PPE) spectra such as those shown in Figure 16.^[151,152] Here the initial excitation is via $h\nu_1 = 1.55$ eV photons that create the initial nearly flat electron energy distribution up to a maximum energy of 1.55 eV with respect to E_F . Not surprisingly, the larger the fluence, the higher is the population in this distribution. Moreover, time-delayed experiments demonstrate that the lifetime of excited electrons is short, on the scale of 10^{-15} s or the like. Since typical group velocity is of the order of 10^8 cm/s, only those electrons emerging between 10^{-7} and 10^{-6} cm from the surface will retain their original energy.

These electrons may easily interact with the first monolayer, in particular electrons with suitable energy may tunnel into an adsorbate LUMO (Figure 17), thus creating a transient negative ion (TNI). Depending on the nature of the electronic state formed, in particular on the bonding or antibonding character of the orbital where the incoming electron resides, these intermediates can either dissociate or remain bound.

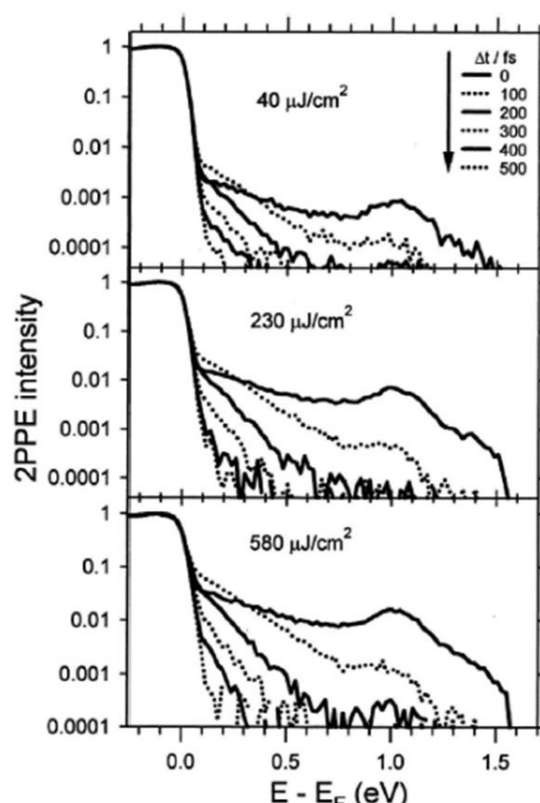


Figure 16: Logarithmic 2PPE spectra versus time delay at three indicated fluencies, pumped by $h\nu_1=1.55$ eV and probed by $h\nu_2=4.058$ eV. Reprinted with permission from ref ^[152].

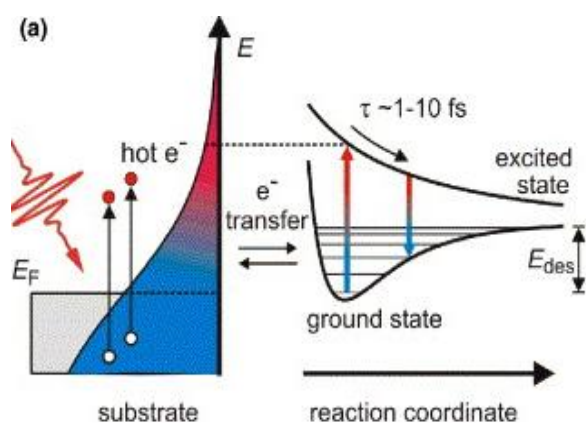


Figure 17: Sketch of the TNI process. Visible or near-UV photons are absorbed in the substrate and create hot electrons. If the energy fits, tunnelling into an unoccupied level of the adsorbate will occur. Reprinted with permission from ref. ^[151]. Copyright 2006 American Chemical Society.

As an example, for monolayer halides on Ag(111) the red shift in the thresholds ranges from chloride 2.0-2.2 eV (chloride) through ~1.5 eV (bromide) to ~1.0 eV (iodide). These shifts depend on the position of the molecular LUMO level with respect to the substrate Fermi energy.

In summary, radical photodissociation reactions could occur on metal surfaces through two mechanisms. Literature overview shows that indirect transitions mediated by metal absorption is the commonly observed reaction pathway when the molecules are weakly adsorbed on the surface at the submonolayer level. Molecular orbitals alignment with respect to metal's Fermi energy affects the photodissociation threshold and in general the reaction takes place at longer wavelength than in the gas phase.

Several papers^[147,153] report on surface photochemistry driven by photon excitation of electrons in the metal substrate. These include photodesorption of NO on Pt(111); photodesorption and dissociation of O₂ on Pd(111) and Ag(110); SO₂, C₂H₅Cl, CH₃Br, CH₃I, ClC₂H₄Br, C₆H₅Cl and C₆H₅OH on Ag(111), CO on Cu(111). Compared to the gas phase, for all the adsorbates the photon energy thresholds are red-shifted for the monolayer;

Summary and Outlook

Although several reactions have been tested on low-Miller index surfaces, it seems clear that to achieve two-dimensional ordered monolayers more complex approaches than those tested so far are needed. In fact, few cases have provided networks characterized by translational symmetry and, therefore, these appear as unique cases.

The irreversibility of the covalent bonding step in UHV hampers the self-healing mechanism during the formation of the supramolecular networks, thus obstructing the formation of defined and regular 1D or 2D scaffolds. For the formation of sophisticated molecular nanostructures, distinctly separated reaction pathways may be useful for partitioning the synthesis into individual steps and controlling their sequence, thus guiding the assembly by kinetic control.^[145,154–156] The way to adopt is the stepwise activation of distinct reactive sites. Different functional groups that can be activated in a defined order have to be incorporated in the initial molecular precursor. It has been showed^[154] that this approach allows to significantly improve the quality of the resulting structure, but further progresses can be done by exploring different combinations of functional groups, such as carboxylic acid/halogen, halogen/alkyne, alkyne/carboxylic acid and their photochemical activation.

A further approach toward improved control over on-surface synthesis protocols is provided by templating.^[157,158] By using specific vicinal surfaces it is possible to steer the alignment of the monomers in a favourable fashion. This is particularly useful for the synthesis of 1D nanowires, because it is possible to effectively suppress unwanted side reactions. Indeed, as an example, the vicinal Ag(887) has been successfully employed to obtain extended graphdiyne chains,^[157] a result that cannot be achieved on the flat Ag(111) surface. Finally, despite their significance in organic synthesis, a still unexplored synthetic approach regards the controlled cross-coupling reactions between different building blocks. Up to now, few papers report Sonogashira Cross-Coupling on Ag(100) and Au(111)^[159] and only two^[160,161] shows the fully controlled synthesis of an alternating copolymer by mean of complementary steric hindrance.

Results

This section reports on the most significant results obtained during the triennial activity. Following the same organization of the previous chapter, the thermal syntheses are reported first, followed by the photochemical ones. An introduction summarizes the main justifications and the implications of the work in the on-surface synthesis topic.


Molecules-Oligomers-Nanowires-Graphene Nanoribbons: a bottom-up stepwise on-surface covalent synthesis preserving long-range order

The sequential synthesis of two-dimensional polymers is reported in this work. In particular, extended poly-paraphenylene and $N=6$ graphene nanoribbons have been synthesized on Au(111), where N indicates the number of dimer carbon lines across the ribbon itself.

Besides reporting for the first time the synthesis of this type of nanoribbons, i.e. the smallest of the $N=3n$ class, this protocol shows that the gold surface is well suited for the production of polymeric materials through a hierarchical approach: Ullmann coupling and subsequent dehydrogenative coupling. C-Br bonds are thermally activated and the resulting adsorbed halogen atoms mainly desorb from the surface, thus allowing the formed oligomers to optimize their lateral interactions.

The avoided surface poisoning combined with the high mobility of the species on Au, compared to the other noble metal surfaces, provide the formation of long-range ordered superstructures, as proved by the well-defined LEED patterns.

An important role is played by the similarity of the self-organized structure of the precursor with that of the covalently-linked product. In fact, a small sliding of the molecular precursor allows it to be exactly at the final position it will occupy within the polymer, since the functional groups on the monomer are already perfectly oriented within the supramolecular network prior to polymerization.

Finally, by combining photoemission and microscopy techniques it has been shown that the lifting of the  surface reconstruction upon reaction is directly involved in the sequential shifting of the C 1s core level of the overlayer.

Molecules–Oligomers–Nanowires–Graphene Nanoribbons: A Bottom-Up Stepwise On-Surface Covalent Synthesis Preserving Long-Range Order

Andrea Basagni,^{*,†} Francesco Sedona,^{*,†} Carlo A. Pignedoli,[‡] Mattia Cattelan,[†] Louis Nicolas,^{§,†} Maurizio Casarin,[†] and Mauro Sambì[†]

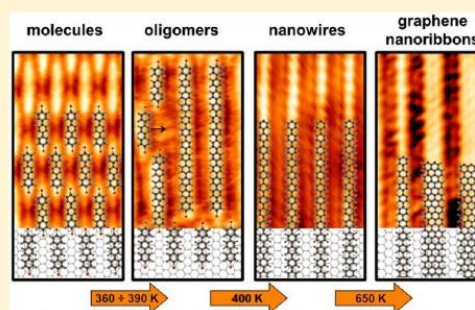
[†]Dipartimento di Scienze Chimiche, Università degli Studi di Padova and Consorzio INSTM, Via Marzolo 1, 35131 Padova, Italy

[‡]NCCR MARVEL, Empa, Swiss Federal Laboratories for Materials Science and Technology, nanotech@surfaces laboratory, 8600 Dübendorf, Switzerland

[§]Ecole Normale Supérieure de Cachan 61, avenue du Président Wilson, 94235 Cachan cedex, France

S Supporting Information

ABSTRACT: We report on a stepwise on-surface polymerization reaction leading to oriented graphene nanoribbons on Au(111) as the final product. Starting from the precursor 4,4'-dibromo-*p*-terphenyl and using the Ullmann coupling reaction followed by dehydrogenation and C–C coupling, we have developed a fine-tuned, annealing-triggered on-surface polymerization that allows us to obtain an oriented nanomesh of graphene nanoribbons via two well-defined intermediate products, namely, *p*-phenylene oligomers with reduced length dispersion and ordered submicrometric molecular wires of poly(*p*-phenylene). A fine balance involving gold catalytic activity in the Ullmann coupling, appropriate on-surface molecular mobility, and favorable topochemical conditions provided by the used precursor leads to a high degree of long-range order that characterizes each step of the synthesis and is rarely observed for surface organic frameworks obtained via Ullmann coupling.



INTRODUCTION

In the last years, the research interests in the field of surface-supported organic monolayers have been focused on two main topics: the growth of epitaxial graphene and the production of surface covalent organic frameworks (SCOFs).^{1–8}

Since graphene layers on metal surfaces represent the global thermodynamic minimum of all conjugated carbon allotropes, simple on-surface thermal decomposition of hydrocarbons⁹ or surface segregation of carbon-containing alloys¹⁰ are becoming the methods of choice to prepare large-area graphene films on various transition-metal surfaces. At the same time, the absence of a band gap in graphene, which is required in order to implement it as a component in field-effect transistor (FET) devices,^{11,12} has stimulated the development of “defective” graphene-like materials by means of chemical modification,^{13,14} defects engineering,^{15,16} and confinement of charge carriers within quasi-one-dimensional (1D) ribbons^{11,17} or quantum nanodots.¹⁸

The versatility of organic functionalization has directed research toward the bottom-up synthesis of graphene-like structures, with the aim of inserting functional groups in the starting building units to tailor the properties at one’s own choice.^{19–21} However, well-ordered SCOFs are rarely obtained under ultrahigh-vacuum conditions^{22–24} because several local thermodynamic minima can be reached starting from a selected

precursor.²⁵ For this reason, the degree of order in a bidimensional covalent layer can be improved only by careful control of the reaction kinetics.^{25–27}

To date, one of the most successful meeting points between the two mentioned research areas has been the precise production of graphene nanoribbons (GNRs) and heterojunctions starting from the precursor 10,10'-dibromo-9,9'-bianthryl (DBBA) or similar molecules.^{28–30} In addition, several other molecular building blocks have been tested to obtain “defective” graphene-like materials, but with less impressive results due to the difficulty of obtaining large regular domains.^{31–34}

Herein we propose a novel finely tuned annealing protocol to perform a stepwise on-surface polymerization reaction leading to oriented GNRs as the final product. In particular, GNRs can be grown using 4,4'-dibromo-*p*-terphenyl (DBTP) as the precursor according to the mechanism shown in Figure 1. On Au(111), the first step is the Ullmann coupling between brominated precursor units^{35–40} in order to form ordered and extended poly(*p*-phenylene) (PPP) wires, which subsequently act as precursors for the synthesis of GNRs after C–H bond activation.^{41–46}

Received: October 7, 2014

Published: January 13, 2015

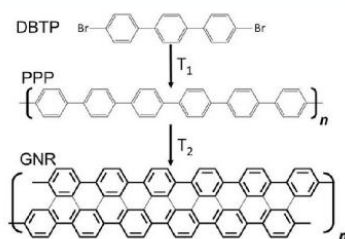


Figure 1. Schematic representation of the bottom-up synthesis of GNRs from the precursor DBTP.

This new approach allowed us to fine-tune the degree of polymerization by controlling the annealing temperature and, if required, to stop the synthesis at a particular intermediate prior to the formation of GNRs, namely, *p*-phenylene oligomers with reduced length dispersion or submicrometric molecular wires of PPP. Moreover, a higher annealing temperature promoted the formation of an oriented nanomesh of GNRs. As a result of the close match between the self-assembled structure of the as-deposited DBTP molecules and the motif of PPP wires, short-range molecular displacements lead from the starting structure to the final structure with no need for long-range on-surface diffusion. Basically for this reason every intermediate product of the synthesis is characterized by extended 2D order, which leads to oriented growth of GNRs with their main axes mostly parallel to the substrate main directions.

RESULTS AND DISCUSSION

The models and experimental scanning tunneling microscopy (STM) images in Figure 2 summarize the main steps in the synthesis of GNRs starting from DBTP, along with the structural features of every intermediate ordered nanostructure. Larger STM images are reported in Figure 3 for the same structures in order to show the extended bidimensional order and the behavior of the herringbone (HB) Au(111) surface reconstruction underneath the reacting molecular layer.

The deposition of a submonolayer of DBTP at room temperature (RT) on Au(111) results in an ordered, close-packed array of unreacted monomers, as shown in Figures 2a and 3a, where molecules can be clearly resolved as linear features oriented with their main axes parallel to the $[1\bar{2}1]$ substrate direction. RT X-ray photoelectron spectroscopy (XPS) outcomes ultimately indicate that the molecules are intact when they adsorb on the surface. Indeed, the C 1s peak (Figure 4d) is characterized by a major component at a binding energy (BE) of 284.2 eV, associated with the phenyl ring, and a smaller feature at BE = 285.1 eV due to bromine-bonded carbon atoms.⁴⁷ Consistent with nondissociative adsorption of DBTP, as observed for similar halogenated molecules on Au(111),^{26,47–51} the stoichiometric ratio (SR) of the two components is 1:8. This is further supported by the Br 3d spectra, which reveal the presence of carbon-bonded bromine only (Br 3d_{5/2} at BE = 69.9 eV; Figure 4a), with no detectable trace of chemisorbed atomic bromine.^{48,49} This close-packed self-assembled structure, described by the $[3\ 1, 2.5\ 5.5]$ matrix (see the low-energy electron diffraction (LEED) pattern in Figure S1a in the Supporting Information), is stabilized by lateral Br⋯H–C hydrogen bonds and Br⋯Br X bonds, as sketched in the inset of Figure 2a and in line with other recently described brominated molecules.^{51,52}

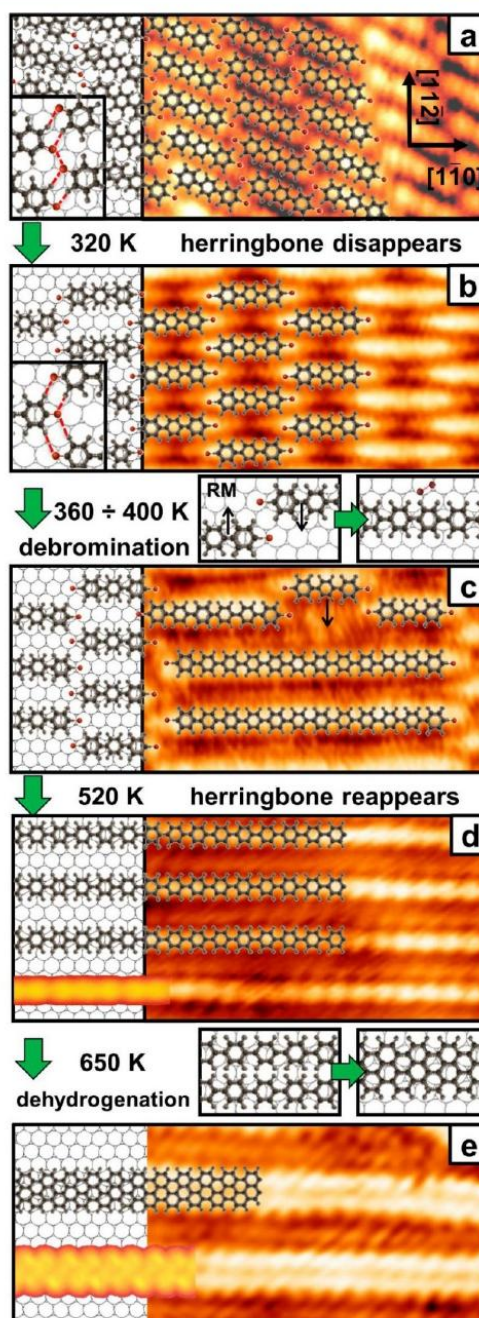


Figure 2. Diagrammatic representation of the different structures obtained during the synthesis of GNRs. For each reaction step, the annealing temperature and the main structural and chemical effects on the system are indicated. All of the images are aligned as reported in (a). The bottom left insets in panels (d) and (e) report DFT-based STM simulations ($V = -0.4$ V) of the PPP wire and a GNR with $N = 6$, respectively, for comparison with the experimental images.

After postdeposition annealing of the structure reported in Figure 2a to 320 K, the network is converted into the less dense

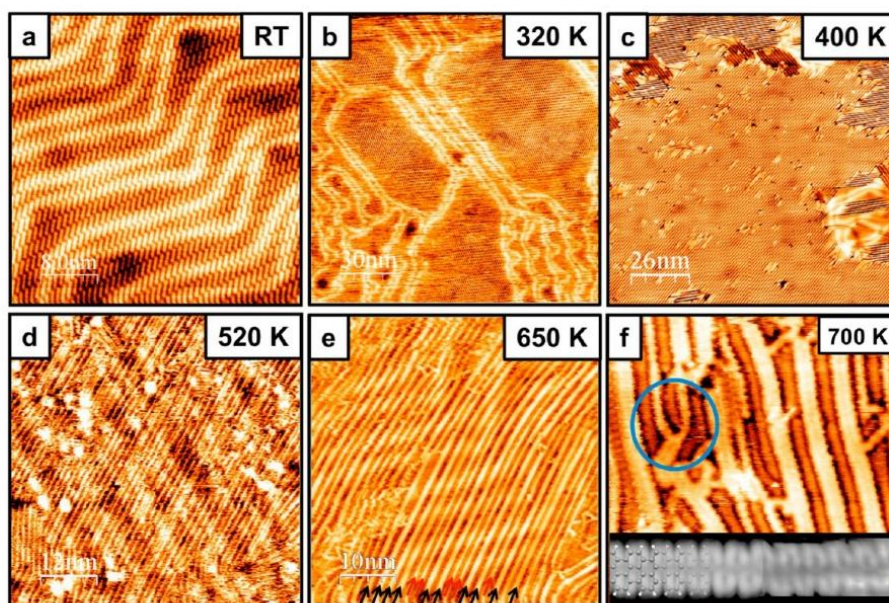


Figure 3. STM images of the Au(111) surface after each thermal treatment step, evidencing the range of the bidimensional order and the behavior of the Au(111) HB surface reconstruction. (a) Molecules deposited at RT. The HB is clearly visible underneath the molecules. (b) After annealing at 320 K, the HB disappears beneath the $[4\ 2, 2\ 6]$ structure and is visible only on the uncovered areas. (c) After annealing at 400 K, long PPP wires are formed, and the HB reappears under the molecules. (d) After annealing at 520 K, PPP wires have a more wavy geometry, and the HB reappears under the molecules. (e) After annealing at 650 K, parallel GNRs (black arrows) are formed from the PPP wires (red arrows). (f) The blue circle highlights two PPP wires extending from the head of a GNR. The bottom inset reports a comparison between a DFT-based simulation ($V = -0.7$ V) with a partially superimposed molecular model (left) and an experimental high-resolution STM image ($V = -0.7$ V, $I = 1$ nA) (right) of a GNR with $N = 6$.

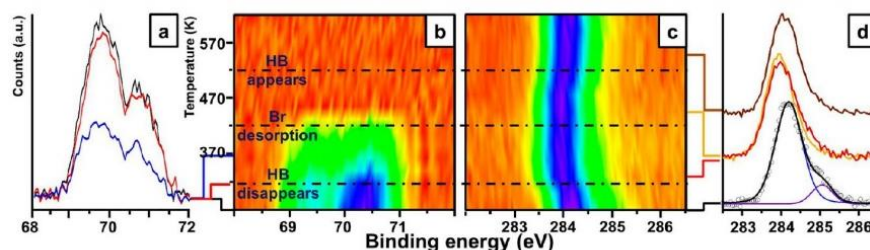


Figure 4. (a, b) Br 3d and (c, d) C 1s X-ray photoelectron spectra as functions of temperature for DBTP/Au(111). The three dash-dotted lines correspond to the onset temperatures for herringbone (HB) reconstruction lifting, bromine desorption, and HB reappearance. Selected spectra acquired at different temperatures are shown in (a) for Br 3d and in (d) for C 1s.

$[4\ 2, 2\ 6]$ structure (see the LEED pattern in Figure S1b), where the molecules lie parallel to the $[\bar{1}10]$ direction, as shown in Figure 2b. Moreover, direct comparison of panels (a) and (b) in Figure 3 shows that at RT the Au(111) HB reconstruction is visible under the molecules, while it disappears underneath the new phase after the annealing. Figure 4 shows that the C 1s XPS peak is the only one affected by this phase transition, with a 0.3 eV shift toward lower BE, while the Br 3d doublet retains its initial position and area. Since at this temperature the chemical identity of DBTP molecules is preserved, we associate the bright protrusions clearly visible at the head and tail of each molecule (Figure 2b) to Br atoms. To confirm this conclusion, we simulated the STM images of the $[4\ 2, 2\ 6]$ structure by assuming both the brominated molecule and the debrominated biradical (Figure

S2), and we concluded that only the first choice matches the experimental images.

In a recent spectroscopic study of the Ullmann coupling reaction of DBBA on Au(111),⁴⁸ a similar C 1s shift was associated with dehalogenation of the molecules as a result of the concurrent shift of Br-related peaks at BE values compatible with the presence of chemisorbed bromine atoms on the surface. In our case, the C 1s shift cannot be associated with any change in the Br 3d XPS peak. For this reason, we propose that the new superstructure is not related to a chemical reaction but rather to a different vertical interaction between the DBTP molecules and the substrate. Indeed, the RT nanostructure is very compact, and the nearest-neighbor intermolecular H–H distance is compatible only with partially tilted molecules; in the lower-density phase, however, molecules can lie flat on the

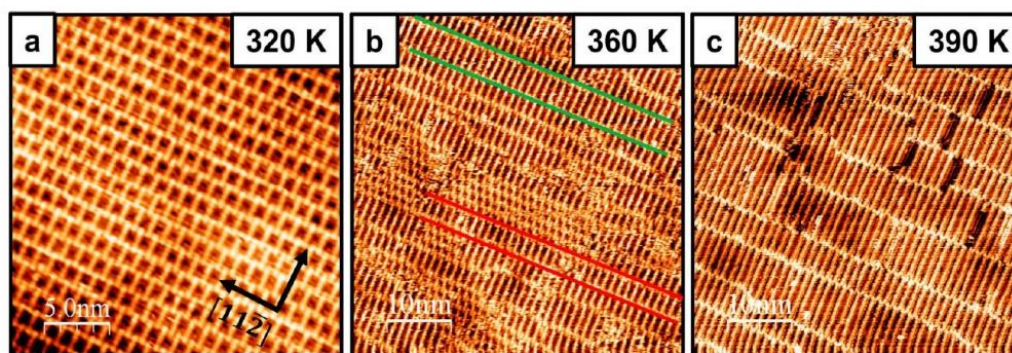


Figure 5. STM images of the self-assembled structures formed by (a) monomers and (b, c) oligomers after annealing at different temperatures, as indicated for each image. Same-length oligomers form rows parallel to the $[11\bar{2}]$ direction, as highlighted by the red and green segments in (b) for dimers and trimers, respectively.

surface, and the local lifting of the HB reconstruction appears to be due to adsorbate-induced stress, similar to what is observed for polycyclic aromatic hydrocarbons adsorbed on the same surface.^{53,54}

Further annealing at temperatures ranging between 360 and 390 K promotes the formation of longer oligomolecular units, as shown in Figures 2c and 5. Since these molecules are slightly shorter than an integer multiple of the individual monomers and appear with a uniform height profile, we conclude that they are oligomers of *p*-phenylene such as dimers, trimers, tetramers, and so on (see Figure S3). As sketched by the arrow in Figure 2c, the DBTP molecules in the $[4\ 2, 2\ 6]$ structure are properly aligned to form oligomers by a little sliding motion along the $[11\bar{2}]$ direction, associated with the elimination of a bromine molecule and the concurrent formation of a C–C bond. Indeed, during this step the area of the Br 3d doublet decreases monotonically as a function of temperature without the formation of chemisorbed bromine atoms (Figure 4a,b), and at the same time the C 1s peak becomes more symmetric. In particular, the decrease in the higher-BE side is associated with the increase in the lower-BE side, in accordance with the formation of new C–C bonds at the expense of the C–Br ones (see the superposition of the red and yellow spectra in Figure 4d).

As shown in Figure 5b, oligomers of the same length form rows along the $[11\bar{2}]$ direction (isolated oligomers are rarely observed). This observation implies that a shift of a DBTP molecule along the $[11\bar{2}]$ direction leads to coupling between units along the molecular main axis, and this movement in turn favors a cooperative shift of all of the subsequent molecules in the same $[11\bar{2}]$ -aligned row as a consequence of the increased steric hindrance between nearest neighbors due to Pauli repulsion, according to the typical Sergeant–Soldier mechanism. Moreover, careful control of the surface temperature between 360 and 390 K promotes the formation of longer oligomers such as heptamers, octamers, and so on (see the statistical analysis reported in Figure S4).

Increasing the temperature over 400 K results in a network of PPP wires characterized by unprecedented long-range order, as confirmed by the presence of the well-defined LEED pattern shown in Figure S1c, which was previously unreported for on-surface Ullmann-produced polymers and is compatible with a commensurate $[4\ 2, 0\ 3]$ structure. The dimensions of the PPP wires are limited only by the grain boundaries of the islands, as

shown in Figure 3c, and can reach 200 nm, even if typical values are around 70 nm. The PPP wires are stable up to 650 K, but an important change shows up after the annealing at 520 K: above this temperature the overlayer LEED pattern disappears, and STM imaging revealed that the molecular wires acquire a more wavy geometry, with the contextual restoration of the HB reconstruction underneath the molecular layer (Figure 3d). At the same annealing temperature, we observed a 0.2 eV shift in the C 1s XPS peak toward higher BE, as visible in Figure 4c,d. Again, there is an evident correlation between the C 1s shift and the restoration of the HB reconstruction, at variance with recent spectroscopic studies of similar systems⁴⁸ that revealed a correlation between this second C 1s shift and the complete desorption of bromine, which in our case is completed at distinctly lower temperatures, as reported in Figure 4b.

We next explored the carbon–carbon coupling reaction through direct C–H activation in order to achieve the side coupling between adjacent PPP wires. After the treatment at 650 K, we observed the formation of wider molecular stripes, mainly oriented parallel to the PPP wires (see Figures 2e and 3e) and having the same apparent height. A closer inspection of the STM images reveals the presence of some branches arising from the stripe structures. In particular, it appears that some ribbons split into two distinct branches, both having the same shape and dimensions of a single PPP wire, as highlighted in Figure 3f. We conclude that the wider nanostructures formed after thermal annealing at 650 K are GNRs. Our conclusion is further supported by a comparison of the high-resolution STM images reported in Figures 2e and 3f with density functional theory (DFT) simulations obtained by assuming the formation of an armchair GNR with $N = 6$, as expected for the condensation of two PPP wires (see Figure 1) but a novel geometry with respect to GNRs obtained previously by means of on-surface synthesis.^{28,46} In detail, the simulated images show that the edge is characterized by an antiphase zigzag domain boundary, a feature revealed by STM imaging. Moreover, Raman spectra (see Figure S5) conclusively demonstrate the formation of GNRs, since the G' , $D + D'$, and $2G$ bands, which are very sensitive fingerprints of the presence of graphenic materials,^{55,56} show up after annealing at 650 K. Although the dispersion of the lengths is large, ranging from 10 to 70 nm, this reaction protocol affords mostly aligned GNRs, as is evident in Figure 3e. Almost all of the nanoribbons terminate in one or two wires as a result of nonperfect zipping

of two PPP molecules. This leads to nanoribbons serially connected by PPP wires.

Annealing at temperatures near the threshold for C–H bond activation (650 K) mainly promotes the coupling of two PPP wires, while treatments at higher temperatures (up to 800 K) activate the condensation of unreacted wires, leading to wider GNRs, as shown by the STM image reported in Figure 6a.

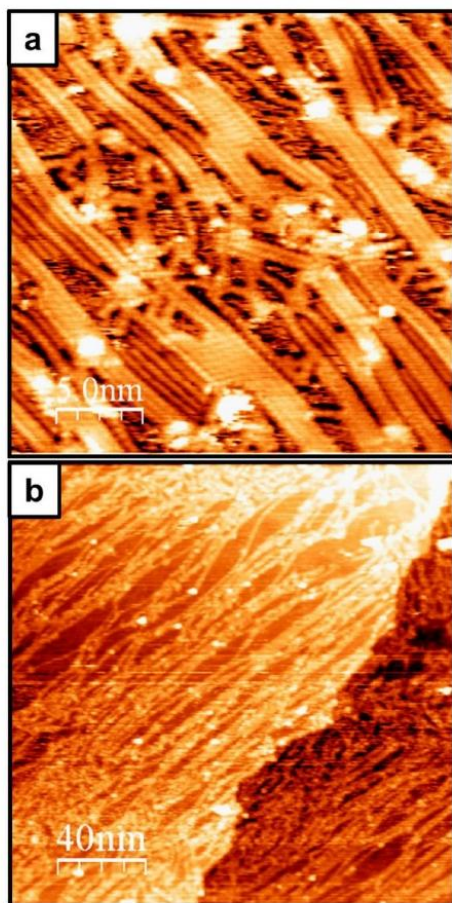


Figure 6. (a) STM image of wider GNRs due to the coupling of more than two PPP wires prepared after annealing PPP wires at 800 K. (b) Large-scale image showing the preferential azimuthal orientation of the defective GNR mesh.

However, this reaction step is not driven by self-assembly any more, but rather by long-range, random diffusional events activated by the high temperature. For this reason, the coupling between aryl groups occurs randomly, leading to the formation of branches that interconnect the nanoribbons; the resulting structure is a sort of highly defective GNR mesh in which a clear preferential azimuthal orientation deriving from the hierarchical procedure is still evident (see Figure 6b).

CONCLUSIONS

We have reported a bottom-up synthesis of submicron-length, long-range-ordered PPP as an intermediate product and large, oriented graphene nanoribbons as the final product using 4,4'-

dibromo-*p*-terphenyl as the molecular precursor on Au(111). Moreover, fine-tuning of the reaction conditions allows the degree of polymerization in the Ullmann coupling reaction to be controlled with almost monomolecular precision.

The comparison of results reported here with those obtained by Lin and co-workers⁵⁷ on Cu(111) is particularly interesting. On Cu(111), the DBTP self-assembled structure is converted into an organometallic network prior to the formation of PPP wires, and a limited 2D order is obtained. This intermediate is not observed on gold, in agreement with what has been observed previously for other halogenated molecules on the same surface.^{50,58,59} In this respect, as inferred by Lackinger and co-workers,²⁶ the gold surface might still be the best compromise between sufficient catalytic activity, high molecular mobility, and weak adsorption energy for the halogen leaving group. In the present case, gold acts as the catalyst for the Ullmann reaction, but it does not form an organometallic network with the selected debrominated precursor. A direct consequence is that the molecules can self-organize freely, and only when they are properly aligned does the reaction occur, as reported previously in the case of GNRs obtained from the precursor DBBA.²⁸

An interesting difference between the cases of GNRs formed from DBBA and from DBTP is the behavior of bromine, as revealed by XPS analysis: in the former case, Br atoms detach from the monomer and adsorb on the Au(111) substrate by annealing between 400 and 500 K and then desorb as Br₂ molecules after annealing at 550 K, whereas when DBTP is used on the same substrate, bromine desorbs in the much lower temperature range of 360–400 K and no adsorbed atomic bromine is detected by XPS.⁴⁹ This difference can be easily explained when the different structures formed by the deposited molecules before the debromination step are analyzed. In the case of DBBA, the brominated molecules form ordered rows with the Br atoms relatively far from each other.⁵⁹ As a consequence, annealing induces the adsorption of isolated Br atoms on the surface, too far from each other to form Br₂ molecules unless thermal diffusion sets in. Conversely, DBTP molecules arrange in the [4 2, 2 6] structure, where the apical Br atoms residing on nearest-neighbor molecules are close to each other, and therefore, thermally triggered C–Br bond cleavage puts two nearby Br atoms at a mutual bonding distance, thereby promoting the formation and contextual desorption of a Br₂ molecule. Concurrently, with a little sliding motion along the [112] direction, the two remaining radicals can react to form a C–C bond. In summary, in the DBBA case the rate-limiting step for bromine desorption is most likely set by the rate of Br₂ formation as a result of random diffusion of adsorbed atomic Br, whereas in the present case the rate-limiting step appears to be C–Br bond cleavage, with the spatial confinement of Br couples due to the starting geometry favoring almost immediate subsequent formation and desorption of molecular bromine.

As a final remark, this work confirms once more²³ that one of the most efficient ways to obtain large domains of long-range ordered SCOFs using nonreversible covalent coupling, as in the case of Ullmann-type reactions, is to start from a supra-molecular arrangement of precursors that is able to rearrange into the final covalent nanostructure with small local positional/orientational adjustments, thus avoiding long-range on-surface diffusion, which typically leads to highly defective final structures. In this way it has been possible to obtain large ordered domains of PPP and GNRs with their main axes mostly

parallel to the substrate main directions. In perspective, the reported synthesis seems to be the most favorable candidate for the growth of unidirectional and size-controlled ribbons by exploiting a surface templating effect.^{60,61} By confining the rodlike molecules onto the reduced-width terrace of a vicinal surface, we expect to achieve both a highly anisotropic material on the macroscopic length scale and fine control of the dimensional dispersion. Moreover, this method is not limited to the synthesis of carbon-rich materials but should be applicable to the introduction of dopant atomic species or functional groups in specific positions if a proper rodlike precursor is employed.

EXPERIMENTAL SECTION

STM Imaging. Experiments were performed under ultrahigh-vacuum conditions at a base pressure of 2×10^{-10} mbar with an Omicron scanning tunneling microscope (VT-STM). All of the STM measurements were carried out at RT in constant-current mode using an electrochemically etched Pt–Ir tip. Typical parameters were a sample bias voltage (V_{bias}) of ± 1 V and a tunneling current (I) of 2–5 nA. The STM data were processed with the WSxM software.⁶² Moderate filtering was applied for noise reduction.

Sample Preparation. The Au(111) crystal was cleaned by repeated cycles of 1 keV Ar⁺ sputtering and annealing at 820 K until a clean surface with sufficiently large terraces was confirmed by STM imaging. Commercially available DBTP molecules were deposited from a pyrolytic boron nitride crucible held at ~ 390 K. The coverage was 0.7 monolayer (ML) in all of the experiments, as calibrated on the C 1s XPS signal, where 1 ML is defined as a surface fully covered by the [3 1, 2.5 5.5] structure. The molecular source was outgassed until the pressure did not increase during the sublimation. During deposition the surface was always held at RT, and the polymerization was activated by subsequent thermal annealing. The final temperature was kept for at least 3 h to allow the system to evolve until it reached a stationary state under the given conditions; the samples were then cooled to RT and analyzed. STM images were statistically analyzed by molecular counting. Molecules were only considered when they were completely resolved, and the analysis encompassed at least 3000 molecules for each temperature.

X-ray Photoelectron Spectroscopy. Measurements were performed in situ at RT using a VG Scienta XM 650 X-ray source. The X-rays produced were monochromatized using a VG Scienta XM 780 monochromator optimized for Al K α radiation (1486.7 eV). Photoelectrons were collected and analyzed with a Scienta SES 100 electron analyzer fitted to the STM preparation chamber.

Simulations. Simulations of DBTP networks adsorbed on the Au(111) surface were performed using DFT in the mixed Gaussian plane waves framework as implemented in the CP2K code.⁶³ We used the Perdew–Burke–Ernzerhof (PBE) parametrization of the exchange–correlation functional. DFT-D3 dispersion corrections were included.⁶⁴

The Au(111) substrate was modeled within the repeated slab geometry⁶⁵ using orthorhombic simulation cells containing four layers of gold and one layer of hydrogen atoms to suppress the surface state of Au(111) on one side of the slab. The lateral size of the unit cell corresponded to 200 unit cells (10×10 rectangular units), and more than 20 Å of vacuum was included. The geometries of the topmost two Au(111) layers and the adsorbed molecular species were fully optimized until forces on atoms were lower than 10^{-4} a.u. STM simulations were performed in the Tersoff–Hamann approximation⁶⁶ in constant-current mode. To overcome limitations of localized basis sets for nonperiodic systems, the electronic states were extrapolated into the vacuum region.⁶⁷ Since the tip shape and the tip–sample distance were not accessible experimentally, a quantitative simulation of the experimental tunneling current was not attempted here. We chose the charge-density isovalue to provide a realistic tip–sample distance on the order of 5 Å.

Raman Spectroscopy. Raman spectra were acquired with a ThermoFisher DXR Raman microscope using a 532 nm laser (3.0 mW) focused on the sample with a 50 \times objective (Olympus) to obtain a spot size of about 1 μm . A single acquisition lasted no more than 20 min to avoid laser-induced damage of the sample.

ASSOCIATED CONTENT

Supporting Information

Detailed descriptions of experimental procedures, LEED results, simulation of DBTP STM images, STM statistical analysis, and Raman measurements. This material is available free of charge via the Internet at <http://pubs.acs.org>.

AUTHOR INFORMATION

Corresponding Authors

*andrea.basagni@studenti.unipd.it

*francesco.sedona@unipd.it

Notes

The authors declare no competing financial interest.

ACKNOWLEDGMENTS

This work was partially funded by MIUR (PRIN 2010/11, Project 2010BNZ3F2: “DESCARTES”), Progetti di Ricerca di Ateneo (CPDA118475/11), and Progetto Futuro in Ricerca 2012 (RBFRI28BEC). The Swiss Federal Supercomputing Center (CSCS) is acknowledged for computational resources (Project s507).

REFERENCES

- Colson, J.; Dichtel, W. *Nat. Chem.* **2013**, *5*, 453–465.
- Lafferentz, L.; Eberhardt, V.; Dri, C.; Africh, C.; Comelli, G.; Esch, F.; Hecht, S.; Grill, L. *Nat. Chem.* **2012**, *4*, 215–220.
- Sakamoto, J.; van Heijst, J.; Lukin, O.; Schlüter, A. D. *Angew. Chem., Int. Ed.* **2009**, *48*, 1030–1069.
- Grill, L.; Dyer, M.; Lafferentz, L.; Persson, M.; Peters, M. V.; Hecht, S. *Nat. Nanotechnol.* **2007**, *2*, 687–691.
- Mas-Ballesté, R.; Gómez-Navarro, C.; Gómez-Herrero, J.; Zamora, F. *Nanoscale* **2011**, *3*, 20–30.
- Wofford, J. M.; Starodub, E.; Walter, A. L.; Nie, S.; Bostwick, A.; Bartelt, N. C.; Thürmer, K.; Rotenberg, E.; McCarty, K. F.; Dubon, O. *New J. Phys.* **2012**, *14*, No. 053008.
- Geim, A. K.; Novoselov, K. S. *Nat. Mater.* **2007**, *6*, 183–191.
- Seyller, T.; Bostwick, A.; Emtsev, K. V.; Horn, K.; Ley, L.; McChesney, J. L.; Ohta, T.; Riley, J. D.; Rotenberg, E.; Speck, F. *Phys. Status Solidi B* **2008**, *245*, 1436–1446.
- Gao, L.; Guest, J. R.; Guisinger, N. P. *Nano Lett.* **2010**, *10*, 3512–3516.
- Sutter, P. W.; Flege, J.-I.; Sutter, E. A. *Nat. Mater.* **2008**, *7*, 406–411.
- Wang, X.; Ouyang, Y.; Li, X.; Wang, H.; Guo, J.; Dai, H. *Phys. Rev. Lett.* **2008**, *100*, No. 206803.
- Lv, R.; Terrones, M. *Mater. Lett.* **2012**, *78*, 209–218.
- Elias, D. C.; Nair, R. R.; Mohiuddin, T. M. G.; Morozov, S. V.; Blake, P.; Halsall, M. P.; Ferrari, A. C.; Boukhvalov, D. W.; Katsnelson, M. I.; Geim, A. K.; Novoselov, K. S. *Science* **2009**, *323*, 610–613.
- Nair, R. R.; Ren, W.; Jalil, R.; Riaz, I.; Kravets, V. G.; Britnell, L.; Blake, P.; Schedin, F.; Mayorov, A. S.; Yuan, S.; Katsnelson, M. I.; Cheng, H.-M.; Strupinski, W.; Bulusheva, L. G.; Okotrub, A. V.; Grigorieva, I. V.; Grigorenko, A. N.; Novoselov, K. S.; Geim, A. K. *Small* **2010**, *6*, 2877–2884.
- Terrones, H.; Lv, R.; Terrones, M.; Dresselhaus, M. S. *Rep. Prog. Phys.* **2012**, *75*, No. 062501.
- Banhart, F.; Kotakoski, J.; Krasheninnikov, A. V. *ACS Nano* **2011**, *5*, 26–41.
- Yan, Q.; Huang, B.; Yu, J.; Zheng, F.; Zang, J.; Wu, J.; Gu, B.-L.; Liu, F.; Duan, W. *Nano Lett.* **2007**, *7*, 1469–1473.

- (18) Lee, J.; Kim, K.; Park, W. I.; Kim, B.-H.; Park, J. H.; Kim, T.-H.; Bong, S.; Kim, C.-H.; Chae, G.; Jun, M.; Hwang, Y.; Jung, Y. S.; Jeon, S. *Nano Lett.* **2012**, *12*, 6078–6083.
- (19) Xu, L.; Zhou, X.; Yu, Y.; Tian, W. Q.; Ma, J.; Lei, S. *ACS Nano* **2013**, *7*, 8066–8073.
- (20) Dienstmaier, J. F.; Medina, D. D.; Dogru, M.; Knochel, P.; Bein, T.; Heckl, W. M.; Lackinger, M. *ACS Nano* **2012**, *6*, 7234–7242.
- (21) Tanoue, R.; Higuchi, R.; Ikebe, K.; Uemura, S.; Kimizuka, N.; Stieg, A. Z.; Gimzewski, J. K.; Kunitake, M. *J. Electroanal. Chem.* **2014**, *716*, 145–149.
- (22) Basagni, A.; Colazzo, L.; Sedona, F.; DiMarino, M.; Carofiglio, T.; Lubian, E.; Forrer, D.; Vittadini, A.; Casarin, M.; Verdini, A.; Cossaro, A.; Floreano, L.; Sambri, M. *Chem.—Eur. J.* **2014**, *20*, 14296–14304.
- (23) Sedona, F.; Di Marino, M.; Sambri, M.; Carofiglio, T.; Lubian, E.; Casarin, M.; Tondello, E. *ACS Nano* **2010**, *4*, 5147–5154.
- (24) Deshpande, A.; Sham, C.-H.; Alaboson, J. M. P.; Mullin, J. M.; Schatz, G. C.; Hersam, M. C. *J. Am. Chem. Soc.* **2012**, *134*, 16759–16764.
- (25) Ourdjini, O.; Pawlak, R.; Abel, M.; Clair, S.; Chen, L.; Bergeon, N.; Sassi, M.; Oison, V.; Debierre, J.-M.; Coratger, R.; Porte, L. *Phys. Rev. B* **2011**, *84*, No. 125421.
- (26) Eichhorn, J.; Nieckarz, D.; Ochs, O.; Samanta, D.; Schmittl, M.; Szabelski, P. J.; Lackinger, M. *ACS Nano* **2014**, *8*, 7880–7889.
- (27) Eichhorn, J.; Strunskus, T.; Rastgoo-Lahrood, A.; Samanta, D.; Schmittl, M.; Lackinger, M. *Chem. Commun.* **2014**, *50*, 7680–7682.
- (28) Cai, J.; Ruffieux, P.; Jaafar, R.; Bieri, M.; Braun, T.; Blankenburg, S.; Muoht, M.; Seitsonen, A. P.; Saleh, M.; Feng, X.; Müllen, K.; Fasel, R. *Nature* **2010**, *466*, 470–473.
- (29) Blankenburg, S.; Cai, J.; Ruffieux, P.; Jaafar, R.; Passerone, D.; Feng, X.; Müllen, K.; Fasel, R.; Pignedoli, C. A. *ACS Nano* **2012**, *6*, 2020–2025.
- (30) Cai, J.; Pignedoli, C. A.; Talirz, L.; Ruffieux, P.; Söde, H.; Liang, L.; Meunier, V.; Berger, R.; Li, R.; Feng, X.; Müllen, K.; Fasel, R. *Nat. Nanotechnol.* **2014**, *9*, 896–900.
- (31) Bieri, M.; Treier, M.; Cai, J.; Ait-Mansour, K.; Ruffieux, P.; Gröning, O.; Gröning, P.; Kastler, M.; Rieger, R.; Feng, X.; Müllen, K.; Fasel, R. *Chem. Commun.* **2009**, 6919–6921.
- (32) Fan, Q.; Wang, C.; Liu, L.; Han, Y.; Zhao, J.; Zhu, J.; Kuttner, J.; Hilt, G.; Gottfried, J. M. *J. Phys. Chem. C* **2014**, *118*, 13018–13025.
- (33) Gutzler, R.; Walch, H.; Eder, G.; Kloft, S.; Heckl, W. M.; Lackinger, M. *Chem. Commun.* **2009**, 4456–4458.
- (34) Bieri, M.; Blankenburg, S.; Kivala, M.; Pignedoli, C. A.; Ruffieux, P.; Müllen, K.; Fasel, R. *Chem. Commun.* **2011**, *47*, 10239–10241.
- (35) Fan, Q.; Wang, C.; Han, Y.; Zhu, J.; Hieringer, W.; Kuttner, J.; Hilt, G.; Gottfried, J. M. *Angew. Chem., Int. Ed.* **2013**, *52*, 4668–4672.
- (36) Lin, T.; Shang, X. S.; Adisoejoso, J.; Liu, P. N.; Lin, N. J. *Am. Chem. Soc.* **2013**, *135*, 3576–3582.
- (37) Krasnikov, S. A.; Doyle, C. M.; Sergeeva, N. N.; Preobrajenski, A. B.; Vinogradov, N. A.; Sergeeva, Y. N.; Zakharov, A. A.; Senge, M. O.; Cafolla, A. A. *Nano Res.* **2011**, *4*, 376–384.
- (38) Fan, Q.; Wang, C.; Han, Y.; Zhu, J.; Kuttner, J.; Hilt, G.; Gottfried, J. M. *ACS Nano* **2014**, *8*, 709–718.
- (39) Lipton-Duffin, J. A.; Ivasenko, O.; Perepichka, D. F.; Rosei, F. *Small* **2009**, *5*, 592–597.
- (40) Di Giovannantonio, M.; El Garah, M.; Lipton-Duffin, J.; Meunier, V.; Cardenas, L.; Fagot Revurat, Y.; Cossaro, A.; Verdini, A.; Perepichka, D. F.; Rosei, F.; Contini, G. *ACS Nano* **2013**, *7*, 8190–8198.
- (41) Zhong, D.; Franke, J.-H.; Podiyanchari, S. K.; Blömker, T.; Zhang, H.; Kehr, G.; Erker, G.; Fuchs, H.; Chi, L. *Science* **2011**, *334*, 213–216.
- (42) Sun, Q.; Zhang, C.; Kong, H.; Tan, Q.; Xu, W. *Chem. Commun.* **2014**, *50*, 11825–11828.
- (43) Müllegger, S.; Winkler, A. *Surf. Sci.* **2006**, *600*, 1290–1299.
- (44) In't Veld, M.; Iavicoli, P.; Haq, S.; Amabilino, D. B.; Raval, R. *Chem. Commun.* **2008**, 1536–1538.
- (45) Müllegger, S.; Winkler, A. *Surf. Sci.* **2006**, *600*, 3982–3986.
- (46) Huang, H.; Wei, D.; Sun, J.; Wong, S. L.; Feng, Y. P.; Neto, A. H. C.; Wee, A. T. S. *Sci. Rep.* **2012**, *2*, No. 983.
- (47) Kanuru, V. K.; Kyriakou, G.; Beaumont, S. K.; Papageorgiou, A. C.; Watson, D. J.; Lambert, R. M. *J. Am. Chem. Soc.* **2010**, *132*, 8081–8086.
- (48) Batra, A.; Cvetko, D.; Kladnik, G.; Adak, O.; Cardoso, C.; Ferretti, A.; Prezzi, D.; Molinari, E.; Morgante, A.; Venkataraman, L. *Chem. Sci.* **2014**, *5*, 4419–4423.
- (49) Simonov, K. A.; Vinogradov, N. A.; Vinogradov, A. S.; Generalov, A. V.; Zagrebina, E. M.; Mårtensson, N.; Cafolla, A. A.; Carpy, T.; Cunniffe, J. P.; Preobrajenski, A. B. *J. Phys. Chem. C* **2014**, *118*, 12532–12540.
- (50) Blunt, M. O. M.; Russell, J. J. C.; Champness, N. R.; Beton, P. H. *Chem. Commun.* **2010**, *46*, 7157–7159.
- (51) Pham, T. A.; Song, F.; Nguyen, M.-T.; Stöhr, M. *Chem. Commun.* **2014**, *50*, 4–7.
- (52) Jang, W. J.; Chung, K.-H.; Lee, M. W.; Kim, H.; Lee, S.; Kahng, S.-J. *Appl. Surf. Sci.* **2014**, *309*, 74–78.
- (53) Iski, E. V.; Jewell, A. D.; Tierney, H. L.; Kyriakou, G.; Sykes, E. C. H. *Surf. Sci.* **2012**, *606*, 536–541.
- (54) Sellam, F.; Schmitz-Hübsch, T.; Toerker, M. *Surf. Sci.* **2001**, *478*, 113–121.
- (55) Dresselhaus, M. S.; Jorio, A.; Hofmann, M.; Dresselhaus, G.; Saito, R. *Nano Lett.* **2010**, *10*, 751–758.
- (56) Malard, L. M.; Pimenta, M. A.; Dresselhaus, G.; Dresselhaus, M. S. *Phys. Rep.* **2009**, *473*, 51–87.
- (57) Wang, W.; Shi, X.; Wang, S.; Van Hove, M. A.; Lin, N. J. *Am. Chem. Soc.* **2011**, *133*, 13264–13267.
- (58) Schlögl, S.; Heckl, W. M.; Lackinger, M. *Surf. Sci.* **2012**, *606*, 999–1004.
- (59) Koch, M. Growth and Characterization of Single Molecular Wires on Metal Surfaces. Ph.D. Thesis, Freie Universität Berlin, 2013.
- (60) Cirera, B.; Zhang, Y.-Q.; Björk, J.; Klyatskaya, S.; Chen, Z.; Ruben, M.; Barth, J. V.; Klappenberger, F. *Nano Lett.* **2014**, *14*, 1891–1897.
- (61) Cañas-Ventura, M. E.; Xiao, W.; Wasserfallen, D.; Müllen, K.; Brune, H.; Barth, J. V.; Fasel, R. *Angew. Chem., Int. Ed.* **2007**, *46*, 1814–1818.
- (62) Horcas, I.; Fernández, R.; Gómez-Rodríguez, J. M.; Colchero, J.; Gómez-Herrero, J.; Baro, A. M. *Rev. Sci. Instrum.* **2007**, *78*, No. 013705.
- (63) VandeVondele, J.; Krack, M.; Mohamed, F.; Parrinello, M.; Chassaing, T.; Hutter, J. *Comput. Phys. Commun.* **2005**, *167*, 103–128.
- (64) Grimme, S.; Antony, J.; Ehrlich, S.; Krieg, H. *J. Chem. Phys.* **2010**, *132*, No. 154104.
- (65) Pickett, W. E. *Comput. Phys. Rep.* **1989**, *9*, 115–197.
- (66) Tersoff, J.; Hamann, D. *Phys. Rev. B* **1985**, *31*, 805–813.
- (67) Tersoff, J. *Phys. Rev. B* **1989**, *40*, 990–993.

Tuning the one-dimensional band dispersion of on-surface synthesized organic nanowires

In this work we synthesize molecular semiconducting wires with tunable doping levels and great potential for molecular electronics applications. In addition, we direct their growth with regularly stepped surfaces to obtain uniaxially aligned wires. Such controlled alignment allows us to characterize the sample properties not only by local but also by sample averaging techniques. That is, we complement the information obtained from scanning tunneling microscopy and spectroscopy with the powerful information obtained from NEXAFS or angle resolved photoemission, as well as with state-of-the-art calculations. Altogether, we provide an exceptionally detailed characterization of the structural and electronic properties of semiconducting wires that are furthermore synthesized bottom-up with atomic precision, and with doping precisely tuned through the synthesis of the monomeric precursor.

The implications of our results are wide reaching. They provide the full band structure of greatly interesting one-dimensional materials. They demonstrate the tunable doping of semiconducting wires through proper selection of the precursor molecules, without affecting the charge transport response. Finally, they may additionally serve as inspiration towards new molecular precursors designed for further functionalization.

1
2
3
4
5
6
7
8
9
10
11
12
13
14
15
16
17
18
19
20
21
22
23
24
25
26
27
28
29
30
31
32
33
34
35
36
37
38
39
40
41
42
43
44
45
46
47
48
49
50
51
52
53
54
55
56
57
58
59
60

Tuning the one-dimensional band dispersion of on-surface synthesized organic nanowires

Andrea Basagni,¹ Guillaume Vasseur,^{2,3} Carlo A. Pignedoli,⁴ Manuel Vilas-Varela,⁵ Diego Peña,⁵ Louis Nicolas,^{1,6} Lucia Vitali,^{3,7} Jorge Lobo-Checa,^{8,9} Dimas G. de Oteyza,^{2,3,7,} Francesco Sedona,^{1,*} Maurizio Casarin,¹ J. Enrique Ortega,^{2,3,10} Mauro Sambi.^{1,11}*

¹ Dipartimento Scienze Chimiche Università Degli Studi Di Padova, Padova, Italy

² Donostia International Physics Center (DIPC), Paseo Manuel Lardizabal 4, E-20018 San Sebastián, Spain

³ Centro de Física de Materiales (CSIC/UPV-EHU) -Materials Physics Center, Paseo Manuel Lardizabal 5, E-20018 San Sebastián, Spain

⁴ NCCR MARVEL, Empa, Swiss Federal Laboratories for Materials Science and Technology, Dübendorf, Switzerland

⁵ Centro de Investigación en Química Biolóxica e Materiais Moleculares (CIQUS) and Departamento de Química Orgánica, Universidade de Santiago de Compostela, 15782, Spain

⁶ Ecole Normale Supérieure de Cachan, Cachan, France

⁷ Ikerbasque, Basque Foundation for Science, 48011 Bilbao, Spain

1
2
3
4
5
6
7
8
9
10
11
12
13
14
15
16
17
18
19
20
21
22
23
24
25
26
27
28
29
30
31
32
33
34
35
36
37
38
39
40
41
42
43
44
45
46
47
48
49
50
51
52
53
54
55
56
57
58
59
60

⁸ Instituto de Ciencia de Materiales de Aragón (ICMA), CSIC-Universidad de Zaragoza, E-50009 Zaragoza, Spain

⁹ Departamento de Física de la Materia Condensada, Universidad de Zaragoza, E-50009 Zaragoza, Spain

¹⁰ Departamento de Física Aplicada I, Universidad del País Vasco, E-20018 San Sebastián, Spain

¹¹ Consorzio INSTM, Unità di Ricerca di Padova, Padova, Italy

KEYWORDS: on-surface synthesis, doping, band structure, poly-para-phenylene, pyridinic functionalization.

ABSTRACT. The tunable properties of molecular materials place them among the favorites for a variety of future generation devices. Besides, to maintain the current trend of miniaturization of those devices, a departure from the present top-down production methods may soon be required and self-assembly appears among the most promising alternatives. On-surface synthesis unites the promises of molecular materials and of self-assembly, with the sturdiness of covalently bonded structures: an ideal scenario for future applications. Following this idea, we report the synthesis of functional extended nanowires by self-assembly. In particular, the products correspond to one-dimensional organic semiconductors. The uniaxial alignment provided by our substrate templates allows us to access with exquisite detail their electronic properties, including the full valence band dispersion, by combining local probes with spatial averaging techniques. We show how, by selectively doping the molecular precursors, the product's energy level alignment can be tuned without compromising the charge transport response.

1
2
3
4
5
6
7 Bottom-up covalent assembly is nowadays a versatile approach to synthesize low dimensional
8 materials.^{1,2,3} Its combination with well-defined substrates, typically termed as “on-surface
9 chemistry”, has achieved great progress over the past few years.^{4,5} Planar multifunctional
10 molecular precursors with different size and shape have been used to grow networks with
11 modular porosity and controlled connectivity,^{6,7,8,9} moreover, the use of different functional
12 groups and different substrates has afforded a significant increase of the degree of long range
13 order through either stepwise or hierarchical approaches.^{10,11,12,13} However, little attention and
14 few experimental studies have been so far devoted to the study of the electronic properties of
15 such surface supported polymers by averaging techniques.^{14,15,16} To some extent this is because
16 many of the produced surface-supported networks have a considerable level of structural
17 defectiveness on the large scale and the probed species not always represent the majority product
18 of the synthesis. Thus, intrinsically local probes such as scanning tunnelling microscopy (STM)
19 and spectroscopy (STS) have been the primary tools for exploring these surface-confined
20 products.^{17,18,19,20} For this reason, although significant computational efforts have been devoted to
21 investigate the electronic properties of 1D and 2D polymers,^{21,22} experiments providing full band
22 dispersion of such polymeric materials and thus a deeper understanding of their electronic
23 properties are still scarce. Such properties of the polymer/substrate interface are, however, of
24 utmost importance for the system’s ultimate functionality. Their understanding and how to tune
25 them by, for instance, chemical modifications, is thus a requisite towards the rational design and
26 electronic structure engineering of functional materials and interfaces.

27
28
29
30
31
32
33
34
35
36
37
38
39
40
41
42
43
44
45
46
47
48
49
50
51
52
53
54
55 Poly-*para*-phenylene (PPP, see Figure 1) is a rigid-wire π -conjugated polymer that has attracted
56 considerable attention. Its large band gap has been exploited to obtain blue light emitting
57
58
59
60

1
2
3 diodes²³ and its conductivity can be easily increased through oxidative or reductive doping.²⁴
4
5 Besides, the booming interest in armchair graphene nanoribbons (A-GNR) has recently
6
7 evidenced that PPP can be considered as the simplest A-GNR with N=3.^{25,26} However, direct
8
9 study of the electronic properties of pristine PPP, as well as its use in practical applications, have
10
11 been hampered by its lack of processability. Oligomers longer than six phenyl rings are insoluble
12
13 and infusible, and the material in both bulk and thin film forms is characterized by high
14
15 defectiveness.²⁷ For these reasons until now the electronic properties of “infinite” PPP wires
16
17 have been inferred from the properties of short, soluble (appropriately functionalized) or surface-
18
19 supported oligomers,^{19,28,29} rather than tested directly.

20
21
22 In this work we exploit on-surface synthesis to obtain extended and macroscopically ordered
23
24
25
26
27
28
29
30
31
32
33
34
35
36
37
38
39
40
41
42
43
44
45
46
47
48
49
50
51
52
53
54
55
56
57
58
59
60
In this work we exploit on-surface synthesis to obtain extended and macroscopically ordered
PPP wires and two different pyridinic derivatives. We report their full characterization by
combined local (STM, STS) and surface averaging techniques (ARPES, NEXAFS, XPS and
LEED), as well as by ab initio calculations based on density functional theory (DFT). Linking
theory and experimental work, the energy-momentum dispersion of extended PPP molecular
wires has been examined and their electronic structure dependence on nitrogen doping in specific
sites of the organic scaffold has been probed.

RESULTS AND DISCUSSION

Figure 1 summarizes the adopted synthetic protocol and shows the chemical structure of the
building blocks. Ullmann-like surface-assisted polymerization of brominated molecular
precursors has been carried out to produce the polymers. Some of us have recently reported a
detailed study on this synthesis protocol using 4,4'-dibromo-*p*-terphenyl (monomer **1** in figure 1)

on Au(111) and the structural characterization of the final products: PPP wires and graphene nanoribbons.²⁶

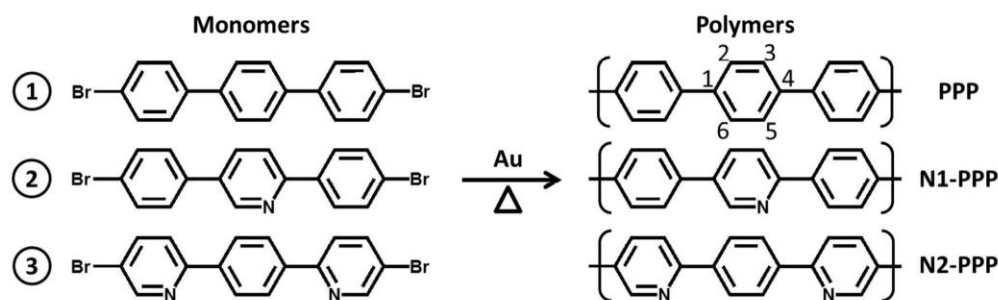


Figure 1. The molecular precursors with none (1), one (2) and two (3) pyridine rings are reported, along with the respective products PPP, N1-PPP and N2-PPP.

Since surface averaging momentum-resolved measurements require the macroscopic alignment of the PPP chains, the polymers were prepared by covalent coupling of 4,4''-dibromo-*p*-terphenyl (1) on clean Au(887). This surface is vicinal to the (111) plane and shows a periodic succession of narrow terraces (≈ 3.9 nm wide) with {111} plane orientation, whose monatomic steps run along the $[1\bar{1}0]$ direction. Because PPP wires grow on Au(111) with their main axis parallel to the $[1\bar{1}0]$ direction,²⁶ Au(887) allows one to align the polymers to obtain a highly anisotropic sample (see Figure 2a). As a result, the LEED pattern corresponds to a superstructure involving uniaxially aligned polymer chains commensurate with the substrate. A well-defined interchain spacing of ~ 10 Å along the $[11\bar{2}]$ direction is evidenced by the LEED spots marked with blue arrows in Figure 2. This spacing supports the presence of Br atoms in between the polymer chains, also observed by STM. Along the chains we infer a periodicity of ~ 8.4 Å (0.75 Å⁻¹), twice the phenyl-phenyl distance, which coincides with thrice the Au lattice. An epitaxial matrix $[4\ 2,0\ 3]$ is thus in excellent agreement with our LEED image. However, an unresolved striped

motif is observed due to the lack of phase relation between the phenyl rings of adjacent chains (see Figure SI1).

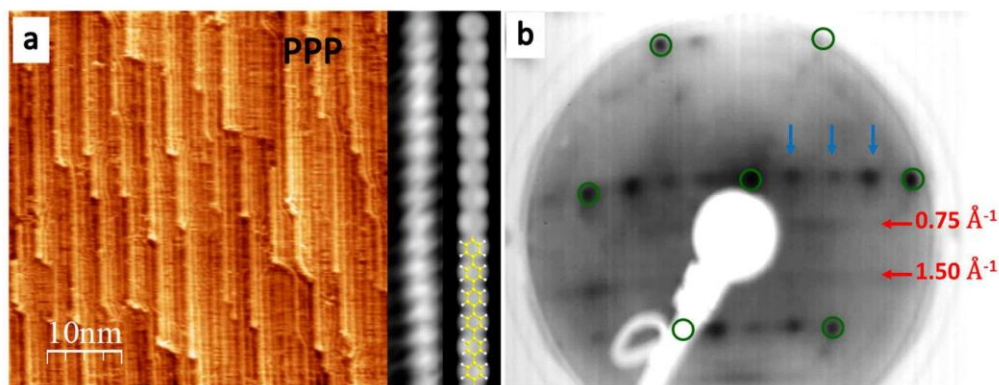


Figure 2. a) STM images of aligned PPP chains on Au(887) and comparison between experimental and DFT simulated STM images ($50 \times 50 \text{ nm}^2$ $V=0.60 \text{ V}$ $I=632 \text{ pA}$) and b) experimental LEED pattern ($E_p=50 \text{ eV}$) of the same surface. Model color code: C yellow, H white.

The experimental band structures, E versus k , of the clean and PPP-covered Au(887) are illustrated in Figure 3a and 3b, respectively. From this direct comparison it is clear that the valence band with maximum (VBM) at $E=-1.04 \text{ eV}$, $k_x=1.49 \text{ \AA}^{-1}$ and dispersing all the way to $E=-6.3 \text{ eV}$ at $\bar{\Gamma}$ originates from the polymeric wires (band marked with the green arrow in Figure 3b and in Figure SI2, where the ARPES second derivative is displayed). The derived real space periodicity (4.21 \AA) relates well with the expected inter-ring spacing of $\approx 4.3 \text{ \AA}$ (1.46 \AA^{-1})³⁰ assuming, as previously observed on *para*-sexiphenyl, that due to modulation of the photoemission transition matrices the measured band maximum corresponds to the polymer structure's second Brillouin zone. In addition, three non-dispersive bands at -2.7 eV , -4.6 eV and -6.22 eV are observed, marked by dotted lines in Figure 2b.

1
2
3
4
5
6
7
8
9
10
11
12
13
14
15
16
17
18
19
20
21
22
23
24
25
26
27
28
29
30
31
32
33
34
35
36
37
38
39
40
41
42
43
44
45
46
47
48
49
50
51
52
53
54
55
56
57
58
59
60

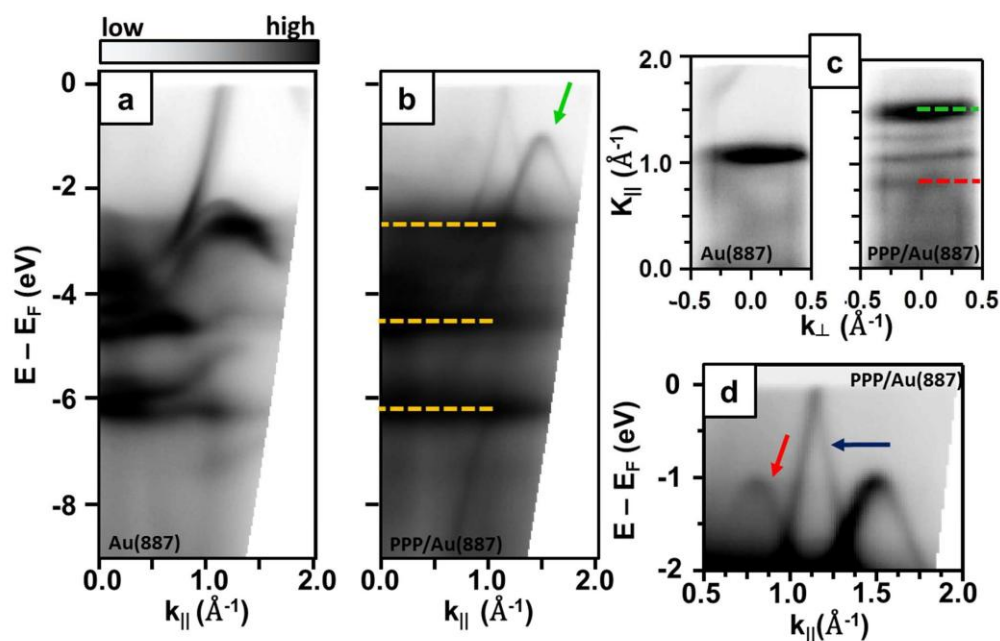


Figure 3. Angle resolved photoemission spectra (ARPES) $I(E-E_F, k_{||})$, where $k_{||}$ is along the $[1\bar{1}0]$ direction (parallel to the wires), of a) clean Au(887) and of b) the oriented PPP/Au(887) interface. c) Constant energy map $I(k_{||}, k_{\perp})$ at $E-E_F=-1.04$ eV of clean Au(887) (left) and of the oriented PPP/Au(887) (right) d) zoom-in of the spectra in b). Arrows and dashed lines highlight peculiar features, see text for details.

DFT calculated band structure (reported in Figure SI3) performed on free-standing polymers, as well as on Au(111)-supported PPP wires with the experimentally found geometry, reproduces correctly the main features of experimental ARPES, such as the curvature of the main dispersive band and the presence of quasi flat bands at energies comparable with the experiment. Calculations with and without the Br atoms remaining in between chains show that the linear arrangement of Br causes none of the bands mentioned above. Figure SI3 also evidences that the dispersive band can be rationalized by a linear combination of benzene orbitals with the major

1
2
3 weight at the linking carbon atoms (i.e. atoms 1 and 4 of each ring) resulting in a molecular
4 orbital delocalized along the PPP wire length, whereas the quasi-flat bands stem from localized
5 molecular orbitals resulting from linear combination of ring-localized benzene orbitals (i.e.
6 atoms 2, 3, 5 and 6 of each ring). Moreover it is important to remark that the energies of the three
7 experimentally observed non-dispersive bands coincide with the intensity maxima of the clean
8 substrate $3d$ bands (see Figure 3a and 3b). Therefore the origin of these experimentally observed
9 bands may be related to a combination of both substrate and PPP overlayer contributions.
10

11
12 Differently from the case of sexyphenyl, where a discretized dispersion has been observed,²⁹ our
13 on-surface polymer shows a continuous dispersion of the band due to the overlap of a higher
14 number of monomer orbitals. A theoretical study of the electronic structure dependence on the
15 length in polyphenylene oligomers has shown that for a molecule with 18 phenyl rings the
16 energy difference between successive states is so small that the situation is equivalent to the
17 formation of a continuous band.³¹ Hence our samples, where the chain length is usually longer
18 than 40 nm (>90 phenyl rings), can be regarded as a good representation of the electronic
19 structure of an infinitely long PPP chain.
20

21
22 Constant energy maps of the clean surface and of PPP wires at the VBM (Figure 3c) reveal that
23 its intensity is spread almost uniformly in k_{\perp} . That is, perpendicular to the wires (along [11-2])
24 the bands show negligible energy dispersion. Such flat bands imply that these orbitals are
25 localized within the wires, due to a negligible intermolecular coupling. The result therefore
26 reflects the occurrence of a truly one-dimensional band dispersion excluding electronic coupling
27 between PPP wires.
28
29
30
31
32
33
34
35
36
37
38
39
40
41
42
43
44
45
46
47
48
49
50
51
52
53
54
55
56
57
58
59
60

1
2
3
4
5
6
7
8
9
10
11
12
13
14
15
16
17
18
19
20
21
22
23
24
25
26
27
28
29
30
31
32
33
34
35
36
37
38
39
40
41
42
43
44
45
46
47
48
49
50
51
52
53
54
55
56
57
58
59
60

Additional weaker features are observed at lower momentum values, see the red arrow in Figure 3d. In particular, a replica of the main dispersive band of the polymer lies at $k_{\parallel} \approx 0.75 \text{ \AA}^{-1}$, i.e. at half of its Brillouin zone ($\pi/4.2 \text{ \AA}$). This is in excellent agreement with the system's periodicity as measured with LEED and may be understood as stemming naturally from the epitaxial relationship with the substrate (which shows commensuration at every second phenyl ring). However, the fact that the unit cell in the direct space is twice the Ph-Ph separation may also be interpreted by a twisted conformation of the PPP chain due to the steric hindrance between the *orto* hydrogen atoms of neighboring phenyl rings.^{32,33} Since the interaction with the substrate usually tends to flatten the molecules (in fact PPP chains are flat on Cu(110)³⁴ while sexyphehyl is twisted in thick films²⁹), the twisted conformation should be confirmed by independent means.

Polarization-dependent NEXAFS measurements have been performed to gather insight into the adsorption geometry of the PPP chains. The spectra were acquired by scanning the $[11\bar{2}]$ surface direction (perpendicular to chains) with the X-ray polarization projection. As observed in Figure 4a, the C K-edge exhibits four peaks at 285.07 (π_1^*), 288.97 (π_2^*), 293.69 (σ_1^*) and a broad peak at 301.59 eV (σ_2^*), in agreement with NEXAFS spectra collected from benzene physisorbed on metal surfaces.^{35,36} The tilt angle of the π^* orbital of the benzene ring relative to the surface normal has been obtained by comparing the angular dependent intensity of the π_1^* resonance and the predicted resonance intensity according to a Stöhr-derived equation for twofold substrate symmetry,³⁷ see SI for details. As reported in Figure 4, the π_1^* resonance intensity shows an opposite polarization dependence to that of σ_1^* and σ_2^* and it is maximized at grazing incidence, while the non-vanishing intensity at normal incidence implies a non-planar geometry: the derived orientation of the benzene ring planes relative to the surface is $\alpha = 20^\circ \pm 5^\circ$ (see Figure SI4). Therefore, NEXAFS linear dichroism confirms that the PPP chains adopt a twisted conformation

wherein adjacent phenyl rings are alternately rotated clockwise and counterclockwise with respect to the PPP main axis. The full twist angle of $40^\circ \pm 10^\circ$ is of the order of that predicted for PPP in the gas phase³³ and remarks the weak influence of the substrate that, for stronger molecule-substrate interactions, would tend to flatten the polymer structure. The observed replica in the ARPES spectrum may thus be related both to a twisted conformation of the polymer and to the commensuration with the substrate, since both effects are observed at the same time.

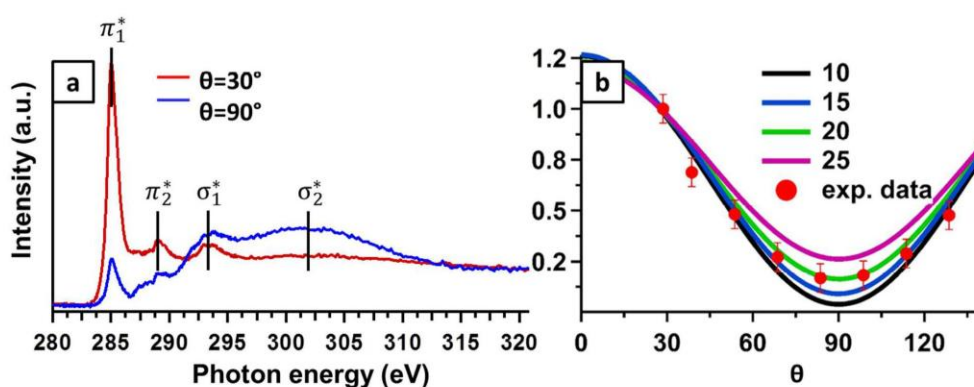


Figure 4. a) Angle-dependence of C K-edge NEXAFS spectra for the aligned PPP chains on Au(887). The spectra were collected with the polarization in the plane defined by the surface normal and the $[11\bar{2}]$ direction (perpendicular to the chains) and Θ is defined as the angle between the polarization and the surface normal (see Figure SI4). b) Angular dependence of the π_1^* resonance intensity compared to the calculated behavior for different tilt angles of the phenyl rings. The calculated curves have been normalized to the first experimental value at $\theta = 30^\circ$ for better comparison.

Interestingly, the formation of this ordered adlayer leads to the observation of an intense replica of the gold *sp* band at 1.13 \AA^{-1} , see the blue arrow in Figure 3d. Indeed, the adlayer introduces a new set of reciprocal lattice vectors \vec{g} , whose reciprocal length is 0.75 \AA^{-1} for the twisted PPP, which can lead to a back-folding of surface emission by a surface Umklapp process. Since the

1
2
3
4
5
6
7
8
9
10
11
12
13
14
15
16
17
18
19
20
21
22
23
24
25
26
27
28
29
30
31
32
33
34
35
36
37
38
39
40
41
42
43
44
45
46
47
48
49
50
51
52
53
54
55
56
57
58
59
60

parallel component of the electron momentum is conserved in the photoemission process, inclusion of this new \vec{g} gives rise, in the present case, to the observed band in the direction containing $\vec{k}_{\parallel} + \vec{g}$ ($1.13+0.75 \text{ \AA}^{-1}$ and folded back at $\approx 1.1 \text{ \AA}^{-1}$, since the \bar{K} point of gold is in the proximity of 1.49 \AA^{-1}).^{38,39} The presence of this Umklapp process, along with the disappearance of the surface state, hints to a significant hybridization between PPP and Au, which has been confirmed with DFT calculations (see Figure S13). Nevertheless, the hybridization is still modest enough to allow for the observation of the full PPP band dispersion throughout the Au 3d band energies, down to -6.3 eV.

The effect of nitrogen incorporation into the conjugated PPP chain has been investigated by two pyridinic derivatives of 4,4'-dibromo-*p*-terphenyl, see monomers **2** and **3** in Figure 1. By means of these molecules, the changes in the electronic and transport properties can be mapped as a function of gradually increased nitrogen content. Again, by employing the 1D templating effect of the Au(887) vicinal surface, the targeted linear products have been obtained with a massive yield. STM imaging reveals well-oriented wires parallel to the steps direction and organized according to the same commensurate epitaxial matrix [4 2,0 3] of the undoped PPP chains. In fact, the pyridinic derivatives are characterized by the same interring distance. Even if these PPP derivatives are isostructural with the undoped PPP, a closer inspection reveals an intramolecular modulation of the probed density of states with the same periodicity of the pyridinic functionalization as visible in the small scale STM images in Figure 5a and 5b.

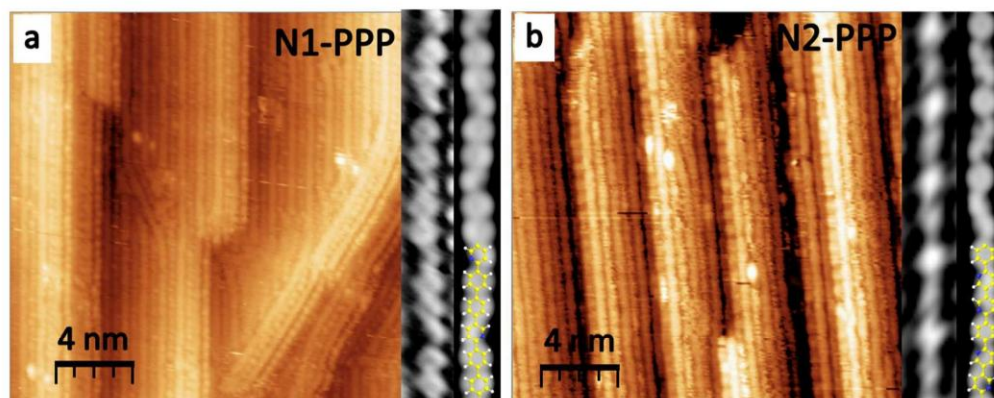


Figure 5. STM pictures of a) N1-PPP and b) N2-PPP grown on Au(887). The comparison between the experimental and DFT simulated STM images of a single are reported as lateral inset for the different polymers. a) $20 \times 20 \text{ nm}^2$ $V = -0.40 \text{ V}$ $I = 512 \text{ pA}$; inset) $V = -0.5 \text{ V}$ $I = 2.0 \text{ nA}$; b) $20 \times 20 \text{ nm}^2$ $V = -0.71 \text{ V}$ $I = 2.6 \text{ nA}$; inset) $V = -0.5 \text{ V}$ $I = 1.50 \text{ nA}$. Model color code: C yellow, N blue, H white.

DFT simulated STM images reported in Figure 5 correctly reproduce this behavior, where the pyridine rings appear smaller than phenyl rings, due to the lack of peripheral H atoms and to the lower N-related partial density of states near the Fermi energy (as reported below in Figure 6). Further evidence for the chemical environment of the nitrogen atoms comes from core-level photoemission (see SI for the complete XPS characterization of N 1s, C 1s, Br 3d core levels). Moving to ARPES, the electronic structure probed on nitrogen-containing polymers share the main characteristics of PPP. In fact, the double periodicity and the Umklapp process are clearly visible both for N1-PPP and for N2-PPP. However, the VBMs exhibit a dependence on the degree of nitrogen substitution. The VBM for the pristine PPP is $E_F - 1.04 \text{ eV}$ and decreases in the N1-PPP to $E_F - 1.26 \text{ eV}$ and to $E_F - 1.38 \text{ eV}$ in N2-PPP (see Figure 6a). Hence, we observe a continuous downshift of the VBM as the nitrogen content increases by as much as $\approx 0.35 \text{ eV}$ for the doubly substituted PPP derivative. Since the conduction band remains above the Fermi level

even in the doped wires, no information can be obtained about the magnitude of the band gap from these ARPES measurements, except that it should be larger than 1.3 ± 0.1 eV.

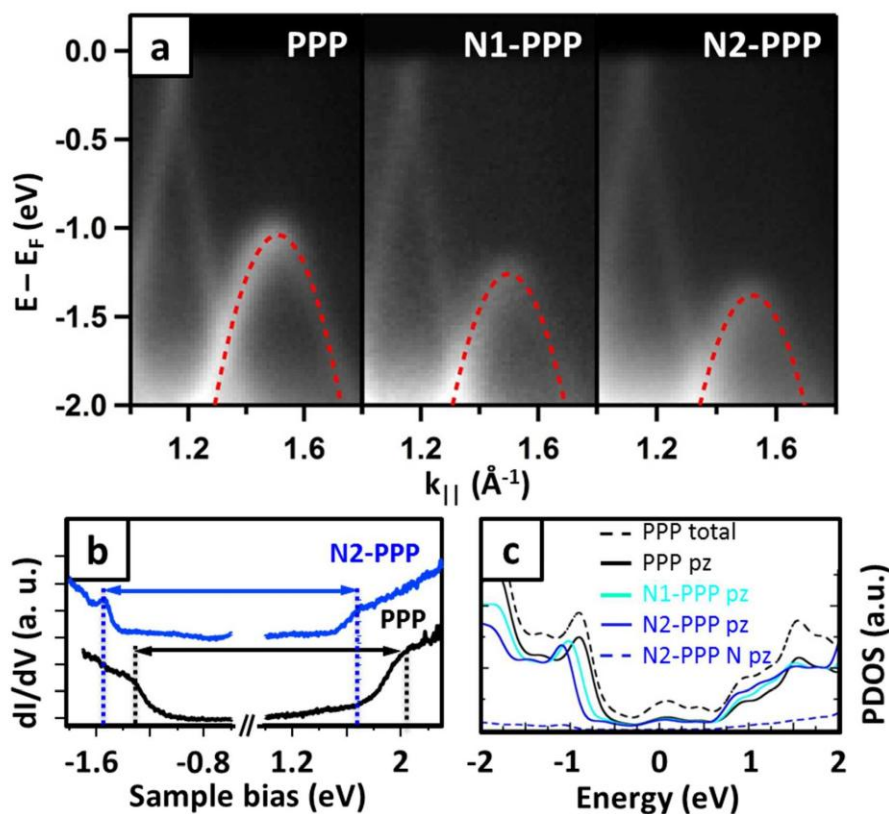


Figure 6: Doping level-dependent electronic properties. Panel a) reports the ARPES spectra of the different polymers at $k_{||}$ close to the VBM. The superimposed red-dashed lines are the parabolic fit of the band revealing an effective mass of $m^* = 0.19 m_0$; b) STM dI/dV spectroscopy performed on PPP and N2-PPP, black and blue spectra respectively; c) computed projected densities of states (PDOS) of the different polymers. Total and p_z projected density of states are compared for PPP, and Nitrogen-related p_z is additionally disclosed for N2-PPP to underline the negligible contribution of N to valence and conduction bands.

1
2
3 Direct measurement of the band gaps has been performed by STS (dI/dV) along the polymer
4 chains, see Figure 6b. In the experimental bias range of -1.8 V to +2.3 V, PPP clearly shows two
5 band onsets around -1.3 and +2.0 V ($E_g=3.3\pm 0.2$ eV), whereas the bands of the nitrogen-
6 containing polymer N2-PPP rigidly shift toward lower bias voltages: -1.5 and +1.7 V
7 ($E_g=3.2\pm 0.2$ eV). Such shift of the entire band structure is in line with previous observations in
8 graphene nanoribbons doped with peripheral nitrogen atoms.^{15,40} The calculated projected
9 densities of states (PDOS) of the different polymers are shown in Figure 6c. Apart from the
10 offset of the conduction band and the absolute value of E_g , the DFT PDOS are qualitatively in
11 agreement with the experimental dI/dV spectra, since both the VB and the CB onsets shift rigidly
12 towards lower bias voltage, leaving the band gap nearly unchanged.
13
14
15
16
17
18
19
20
21
22
23
24
25
26
27

28 The onset of the valence band occurs at slightly higher binding energies in our STS than in our
29 ARPES characterization, probably related to the difference in the measured systems: STS was
30 performed on single PPP chains on Au(111), while ARPES measurements were taken from
31 compact PPP layers on Au(788). Single chains are not flanked by Br atoms. Thus, changes in the
32 local work function due to the different substrates (we measure a lower work function on
33 Au(111) as compared to Au(788) (see Figure SI10)) or to the absence or presence of Br,⁴¹ as well
34 as the lack of screening from neighboring PPP chains or Br atoms during STS
35 characterization,^{42,43} may, together or separately, account for this minor difference.
36
37
38
39
40
41
42
43
44
45
46
47

48 Also the work function of the polymer-covered Au(788) shows a monotonic reduction by ≈ 90
49 meV for each added N atom ($\phi_{N0-PPP}=5.10$ eV, $\phi_{N1-PPP}=5.02$ eV, $\phi_{N2-PPP}=4.93$ eV, see figure
50 S10). However, this effect is smaller in magnitude than the observed shifts in the bands and thus
51 cannot account for the latter phenomenon, for example by vacuum level alignment. Instead, the
52 observed effect is in agreement with the generally accepted picture of pyridine being electron
53
54
55
56
57
58
59
60

1
2
3
4
5
6
7
8
9
10
11
12
13
14
15
16
17
18
19
20
21
22
23
24
25
26
27
28
29
30
31
32
33
34
35
36
37
38
39
40
41
42
43
44
45
46
47
48
49
50
51
52
53
54
55
56
57
58
59
60

deficient in character, in the sense that the electron density is decreased on the carbon ring by electronegative nitrogen. As a result, the HOMO and LUMO are stabilized, the ionization potential and the electron affinity systematically increase, while the HOMO-LUMO gap is nearly unaffected, as observed for solid films of PPP (2.93 eV) and poly-pyridine (2.82-2.95 eV).^{44,45} These gap values, obtained from optical measurements, are in reasonable agreement with our STS data. This agreement should not be surprising, since although it is well known that electron-hole interaction reduces the band gaps obtained from optical techniques,⁴⁶ our measurement is accessing the fundamental gap that is lowered by image charge effects coming from the metallic substrate.⁴⁶ The bandgap is furthermore in good agreement with that reported, based on STS measurements, for PPP on Cu(111) (3.1 ± 0.2 eV).¹⁹

Insight into the transport properties can be gathered in terms of effective mass (m^*) of holes in the valence band, derived from the curvature of the energy band. From a parabolic fit of the top of the valence band we determined $m^* = -0.19 m_e$ for PPP, a value in agreement with DFT calculations on an infinitely long, unsupported PPP wire ($-0.17 m_e$) (see Figure SI3) and in line with the high carrier mobility in PPP oligomers.²⁶ For direct comparison the same analysis was done on N1-PPP and N2-PPP, revealing a negligible effect of the pyridine ring, since both of them have $m^* = -0.19 m_e$. As indicated by the comparison of N2-PPP total p_z and N-related p_z projected DOS reported in figure 6c, the highest-lying valence bands are mainly composed by carbon π density, which amounts to saying that the heteroatom contributes little to define the holes carrier mobility in the valence band.^{45,47}

CONCLUSIONS

1
2
3
4
5
6
7
8
9
10
11
12
13
14
15
16
17
18
19
20
21
22
23
24
25
26
27
28
29
30
31
32
33
34
35
36
37
38
39
40
41
42
43
44
45
46
47
48
49
50
51
52
53
54
55
56
57
58
59
60

In summary, we have grown three different extended one-dimensional polymers in a bottom-up fashion, namely poly-*para*phenylene and two pyridinic derivatives, with selected and gradually increasing nitrogen content. In order to characterize their band structure, macroscopically anisotropic samples have been prepared taking advantage of vicinal surface templating. Using angle resolved photoemission spectroscopy, we reveal a fully dispersive one dimensional behaviour of these semiconducting organic wires and that the electronic structure can be monotonically downshifted relative to the metal Fermi level as the pyridine substitution is increased within the molecular scaffold. Although the nitrogen insertion modulates the valence band onset by as much of 0.3 eV for the doubly doped monomer, DFT calculations in combination with scanning tunneling spectroscopy show that the band gap is almost unaffected ($E_g = 3.3 \pm 0.2$ eV). Furthermore, from a parabolic fit of the ARPES data at the top of the valence band, a similar effective mass of $0.19m_0$ is evidenced for all polymers, implying comparable hole-transport properties irrespective of the degree of nitrogen doping. This work thus confirms the possibility to tailor the electronic properties of functional organic nanowires, in particular the energy level alignment with respect to the Fermi level, without compromising the product's transport response by selectively doping the molecular precursors. Finally, our findings represent a benchmark for the controlled growth of organic monolayers and the characterization of their electronic properties for future technological applications.

ASSOCIATED CONTENT

Supporting Information. Epitaxy model and convoluted LEED pattern, second derivative ARPES data highlighting the full band dispersion, overlap of experimental and calculated band structure, representation of geometry in NEXAFS measurements, C 1s XPS data throughout polymer preparation procedure, C 1s, Br 3d and N 1s XPS data comparing the various polymers

1
2
3
4
5
6
7
8
9
10
11
12
13
14
15
16
17
18
19
20
21
22
23
24
25
26
27
28
29
30
31
32
33
34
35
36
37
38
39
40
41
42
43
44
45
46
47
48
49
50
51
52
53
54
55
56
57
58
59
60

studied, C K-edge NEXAFS spectra comparing the various polymers studied, summary of the energy level shifts between the various polymers studied as observed with different techniques, work function measurements from the low energy cutoff in photoemission spectra, experimental details for chemical synthesis of precursors, sample preparation and characterization, as well as for the calculations. This material is available free of charge via the Internet at <http://pubs.acs.org>.

AUTHOR INFORMATION

Corresponding Author

*d_g_oteyza@ehu.es *francesco.sedona@unipd.it.

Author Contributions

The manuscript was written through contributions of all authors. All authors have given approval to the final version of the manuscript.

ACKNOWLEDGMENT

This work was partially funded by MIUR (PRIN 2010/11, Project 2010BNZ3F2: “DESCARTES”) by EU project PAMS (agreement no. 610446), by the European Research Council (ERC) under the EU Horizon 2020 research and innovation programme (grant agreement No 635919), by the European Community's Seventh Framework Programme (FP7/2007-2013) CALIPSO under grant agreement n° 312284, by the Spanish Ministry of Science and Competitiveness (MINECO, MAT2013-46593-C6-6-P and MAT2013-46593-C6-4-P) and FEDER, and by the Basque Government (Grant No. IT-621-13). We acknowledge the Swiss Supercomputing Center (CSCS) for computational support (project s507). Alberto Verdini

1
2
3
4
5
6
7
8
9
10
11
12
13
14
15
16
17
18
19
20
21
22
23
24
25
26
27
28
29
30
31
32
33
34
35
36
37
38
39
40
41
42
43
44
45
46
47
48
49
50
51
52
53
54
55
56
57
58
59
60

is acknowledged for useful discussions on NEXAFS measurements and beamline staff at Max IV's D1011 for support during the beamtime.

REFERENCES

- ¹ Ding, S.-Y.; Wang, W. Covalent Organic Frameworks (COFs): From Design to Applications. *Chem. Soc. Rev.* **2013**, *42*, 548–568.
- ² Sakamoto, J.; van Heijst, J.; Lukin, O.; Schlüter, A. D. Two-Dimensional Polymers: Just a Dream of Synthetic Chemists? *Angew. Chem. Int. Ed.* **2009**, *48*, 1030–1069.
- ³ Colson, J.; Dichtel, W. Rationally Synthesized Two-Dimensional Polymers. *Nat. Chem.* **2013**, *5*, 453–465.
- ⁴ Lindner, R.; Kühnle, A. On-Surface Reactions. *ChemPhysChem* **2015**, *16*, 1582-1592.
- ⁵ Franc, G.; Gourdon, A. Covalent Networks Through On-Surface Chemistry in Ultra-High Vacuum: State-of-the-Art and Recent Developments. *Phys. Chem. Chem. Phys.* **2011**, *13*, 14283–14292.
- ⁶ Bieri, M.; Blankenburg, S.; Kivala, M.; Pignedoli, C.; Ruffieux, P.; Müllen, K.; Fasel, R. Surface-Supported 2D Heterotriangulene Polymers. *Chem. Commun.* **2011**, *47*, 10239–10241.
- ⁷ Kuang, G.; Zhang, Q.; Li, D. Y.; Shang, X. S.; Lin, T.; Liu, P. N.; Lin, N. Cross-Coupling of Aryl-Bromide and Porphyrin-Bromide on an Au(111) Surface. *Chem. - A Eur. J.* **2015**, *21*, 8028-8032.
- ⁸ Fan, Q.; Wang, C.; Liu, L.; Han, Y.; Zhao, J.; Zhu, J.; Kuttner, J.; Hilt, G.; Gottfried, J.M. Covalent, Organometallic, and Halogen-Bonded Nanomeshes from Tetrabromo-Terphenyl by Surface-Assisted Synthesis on Cu(111). *J. Phys. Chem. C.* **2014**, *118*, 13018–13025.

1
2
3
4
5
6
7
8
9
10
11
12
13
14
15
16
17
18
19
20
21
22
23
24
25
26
27
28
29
30
31
32
33
34
35
36
37
38
39
40
41
42
43
44
45
46
47
48
49
50
51
52
53
54
55
56
57
58
59
60

⁹ Bieri, M.; Treier, M.; Cai, J.; Ait-Mansour, K.; Ruffieux, P.; Gröning, O.; Gröning, P.; Kastler, M.; Rieger, R.; Feng, X.; Müllen, K.; Fasel, R. Porous Graphenes: Two-Dimensional Polymer Synthesis With Atomic Precision. *Chem. Commun.* **2009**, 6919–6921.

¹⁰ Eichhorn, J.; Strunskus, T.; Rastgoo-Lahrood, A.; Samanta, D.; Schmittel, M.; Lackinger, M. On-Surface Ullmann Polymerization Via Intermediate Organometallic Networks on Ag(111). *Chem. Commun.* **2014**, 50, 7680–7682.

¹¹ Zhang, C.; Sun, Q.; Chen, H.; Tan, Q.; Xu, W. Formation of Polyphenyl Chains Through Hierarchical Reactions: Ullmann Coupling Followed by Cross-Dehydrogenative Coupling. *Chem. Commun.* **2015**, 51, 495–498.

¹² Lafferentz, L.; Eberhardt, V.; Dri, C.; Africh, C.; Comelli, G.; Esch, F.; Hecht, S.; Grill, L. Controlling On-Surface Polymerization by Hierarchical and Substrate-Directed Growth. *Nat. Chem.* **2012**, 4, 215–220.

¹³ Faury, T.; Clair, S.; Abel, M.; Dumur, F.; Gigmes, D.; Porte, L. Sequential Linking To Control Growth of a Surface Covalent Organic Framework. *J. Phys. Chem. C* **2012**, 116, 4819–4823.

¹⁴ Cardenas, L.; Gutzler, R.; Lipton-Duffin, J.; Fu, C.; Brusso, J. L.; Dinca, L. E.; Vondráček, M.; Fagot-Revurat, Y.; Malterre, D.; Rosei, F.; Perepichka, D. F. Synthesis and Electronic Structure of a Two Dimensional π -Conjugated Polythiophene. *Chem. Sci.* **2013**, 4, 3263.

¹⁵ Bronner, C.; Stremlau, S.; Gille, M.; Brauße, F.; Haase, A.; Hecht, S.; Tegeder, P. Aligning the Band Gap of Graphene Nanoribbons by Monomer Doping. *Angew. Chem. Int. Ed.* **2013**, 52, 4422–4425.

1
2
3
4
5
6
7
8
9
10
11
12
13
14
15
16
17
18
19
20
21
22
23
24
25
26
27
28
29
30
31
32
33
34
35
36
37
38
39
40
41
42
43
44
45
46
47
48
49
50
51
52
53
54
55
56
57
58
59
60

¹⁶ Ruffieux, P.; Cai, J.; Plumb, N. C.; Patthey, L.; Prezzi, D.; Ferretti, A.; Molinari, E.; Feng, X.; Müllen, K.; Pignedoli, C. A.; Fasel, R. Electronic Structure of Atomically Precise Graphene Nanoribbons. *ACS Nano* **2012**, *6*, 6930–6935.

¹⁷ Riss, A.; Wickenburg, S.; Gorman, P.; Tan, L. Z.; Tsai, H.-Z.; de Oteyza, D. G.; Chen, Y.-C.; Bradley, A. J.; Ugeda, M. M.; Etkin, G.; Louie, S. G.; Fischer, F. R.; Crommie, M. F. Local Electronic and Chemical Structure of Oligo-Acetylene Derivatives Formed Through Radical Cyclizations at a Surface. *Nano Lett.* **2014**, *14*, 2251–2255.

¹⁸ Reece, G.; Bulou, H.; Scheurer, F.; Speisser, V.; Carrière, B.; Mathevet, F.; Schull, G. Oligothiophene Nanorings as Electron Resonators for Whispering Gallery Modes. *Phys. Rev. Lett.* **2013**, *110*, 056802.

¹⁹ Wang, S.; Wang, W.; Lin, N. Resolving Band-Structure Evolution and Defect-Induced States of Single Conjugated Oligomers by Scanning Tunneling Microscopy and Tight-Binding Calculations. *Phys. Rev. Lett.* **2011**, *106*, 206803.

²⁰ Lafferentz, L.; Ample, F.; Yu, H.; Hecht, S.; Joachim, C.; Grill, L. Conductance of a Single Conjugated Polymer as a Continuous Function of Its Length. *Science* **2009**, *323*, 1193–1197.

²¹ Gutzler, R.; Perepichka, D. F. π -Electron Conjugation in Two Dimensions. *J. Am. Chem. Soc.* **2013**, *135*, 16585–16594.

²² Adjizian, J.-J.; Briddon, P.; Humbert, B.; Duvail, J.-L.; Wagner, P.; Adda, C.; Ewels, C. Dirac Cones in Two-Dimensional Conjugated Polymer Networks. *Nat. Commun.* **2014**, *5*, 5842.

²³ Baur, J. W.; Kim, S.; Balanda, P.B.; Reynolds, J. R.; Rubner, M.F. Thin-Film Light-Emitting Devices Based on Sequentially Adsorbed Multilayers of Water-Soluble Poly(p-Phenylene)s. *Adv. Mater.* **1998**, *10*, 1452-1455.

1
2
3
4
5
6
7
8
9
10
11
12
13
14
15
16
17
18
19
20
21
22
23
24
25
26
27
28
29
30
31
32
33
34
35
36
37
38
39
40
41
42
43
44
45
46
47
48
49
50
51
52
53
54
55
56
57
58
59
60

- ²⁴ Shacklette, L.W.; Eckhardt, H.; Chance, R.R.; Miller, G.G.; Ivory, D.M.; Baughman, R. H. Solid-State Synthesis of Highly Conducting Polyphenylene From Crystalline Oligomers. *J. Chem. Phys.* **1980**, *73*, 4098-4102.
- ²⁵ Narita, A.; Wang, X. Y.; Mullen, K. New Advances in Nanographene Chemistry. *Chem. Soc. Rev.* **2015**, *44*, 6616-6643.
- ²⁶ Basagni, A.; Sedona, F.; Pignedoli, C. A.; Cattelan, M.; Nicolas, L.; Casarin, M.; Sambri, M. Molecules–Oligomers–Nanowires–Graphene Nanoribbons: A Bottom-Up Stepwise On-Surface Covalent Synthesis Preserving Long-Range Order. *J. Am. Chem. Soc.*, **2015**, *137*, 1802–1808.
- ²⁷ Bredas, J. L.; Beljonne, D.; Coropceanu, V.; Cornil, J. Charge-Transfer and Energy-Transfer Processes in pi-Conjugated Oligomers and Polymers: a Molecular Picture. *Chem. Rev.* **2004**, *104*, 4971-5003.
- ²⁸ Banerjee, M.; Shukla, R.; Rathore, R. Synthesis, Optical, and Electronic Properties of Soluble Poly-p-Phenylene Oligomers as Models for Molecular Wires. *J. Am. Chem. Soc.* **2009**, *131*, 1780-1786.
- ²⁹ Koller, G.; Berkebile, S.; Oehzelt, M.; Puschnig, P.; Ambrosch-Draxl, C.; Netzer, F. P.; Ramsey, M. G. Intra- and Intermolecular Band Dispersion in an Organic Crystal. *Science* **2007**, *317*, 351–355.
- ³⁰ Baker, K. N.; Fratini, A. V.; Resch, T.; Knachel, H. C.; Adams, W. W.; Soggi, E. P.; Farmer, B. L. Crystal Structures, Phase Transitions and Energy Calculations of Poly(p-Phenylene) Oligomers. *Polymer (Guildf)*. **1993**, *34*, 1571–1587.

1
2
3
4
5
6
7
8
9
10
11
12
13
14
15
16
17
18
19
20
21
22
23
24
25
26
27
28
29
30
31
32
33
34
35
36
37
38
39
40
41
42
43
44
45
46
47
48
49
50
51
52
53
54
55
56
57
58
59
60

- ³¹ Zojer, E.; Shuai, Z.; Leising, G.; Brédas, J. L. From Molecular States to Band Structure: Theoretical Investigation of Momentum Dependent Excitations in Phenylene Based Organic Materials. *J. Chem. Phys.* **1999**, *111*, 1668.
- ³² Sasaki, S.; Yamamoto, T.; Kanbara, T.; Morita, A. Crystal Structure of Poly(p-Phenylene) Prepared by Organometallic Technique. *J. Polym. Sci. Part B Polym. Phys.* **1992**, *30*, 293–297.
- ³³ Ambrosch-Draxl, C.; Majewski, J.; Vogl, P.; Leising, G. First-Principles Studies of the Structural and Optical Properties of Crystalline Poly(para-Phenylene). *Phys. Rev. B* **1995**, *51*, 9668–9676.
- ³⁴ Di Giovannantonio, M.; El Garah, M.; Lipton-Duffin, J.; Meunier, V.; Cardenas, L.; Fagot Revurat, Y.; Cossaro, A.; Verdini, A.; Perepichka, D. F.; Rosei, F.; Contini, G. Insight Into Organometallic Intermediate and Its Evolution to Covalent Bonding in Surface-Confined Ullmann Polymerization. *ACS Nano* **2013**, *7*, 8190–8198.
- ³⁵ Horsley, J. A.; Stöhr, J.; Hitchcock, A. P.; Newbury, D. C.; Johnson, A. L.; Sette, F. Resonances in the K Shell Excitation Spectra of Benzene and Pyridine: Gas Phase, Solid, and Chemisorbed States. *J. Chem. Phys.* **1985**, *83*, 6099.
- ³⁶ Solomon, J. L.; Madix, R. J.; Stöhr, J. Orientation and Absolute Coverage of Benzene, Aniline, and Phenol on Ag(110) Determined by NEXAFS and XPS. *Surf. Sci.* **1991**, *255*, 12–30.
- ³⁷ Stöhr, J.; Outka, D. A. Determination of Molecular Orientations on Surfaces from the Angular Dependence of Near-Edge X-Ray-Absorption Fine-Structure Spectra. *Phys. Rev. B* **1987**, *36*, 7891–7905.
- ³⁸ Mariani, C.; Horn, K.; Bradshaw, A. M. Photoemission Studies of the Commensurate-Incommensurate Transition in the System Xe-Cu(110). *Phys. Rev. B* **1982**, *25*, 7798–7806.

1
2
3
4
5
6
7
8
9
10
11
12
13
14
15
16
17
18
19
20
21
22
23
24
25
26
27
28
29
30
31
32
33
34
35
36
37
38
39
40
41
42
43
44
45
46
47
48
49
50
51
52
53
54
55
56
57
58
59
60

- ³⁹ Anderson, J.; Lapeyre, G. J. Chemisorption-Induced Surface Umklapp Processes in Angle-Resolved Synchrotron Photoemission from W(001). *Phys. Rev. Lett.* **1976**, *36*, 376–379.
- ⁴⁰ Cai, J.; Pignedoli, C. A.; Talirz, L.; Ruffieux, P.; Söde, H.; Liang, L.; Meunier, V.; Berger, R.; Li, R.; Feng, X.; Müllen, K.; Fasel, R. Graphene Nanoribbon Heterojunctions. *Nat. Nanotechnol.* **2014**, *9*, 896–900.
- ⁴¹ Roman, T.; Gossenberger, F.; Forster-Tonigold, K.; Groß, A. Halide Adsorption on Close-Packed Metal Electrodes. *Phys. Chem. Chem. Phys.* **2014**, *16*, 13630–13634.
- ⁴² Fernandez-Torrente, I.; Franke, K.; Pascual, J.I. Spectroscopy of C60 Single Molecules: the Role of Screening on Energy Level Alignment. *J. Phys.: Cond. Mat.* **2008**, *20*, 184001–1–11.
- ⁴³ Cochrane, K.A.; Schiffrin, A.; Roussy, T.S.; Capsoni, M.; Burke, S.A. Pronounced Polarization-Induced Energy Level Shifts at Boundaries of Organic Semiconductor Nanostructures. *Nat. Commun.* **2015**, *6*, 8312–1–8.
- ⁴⁴ Miyamae, T.; Yoshimura, D.; Ishii, H.; Ouchi, Y.; Seki, K.; Miyazaki, T.; Koike, T.; Yamamoto, T. Ultraviolet Photoelectron Spectroscopy of Poly(Pyridine-2,5-Diyl), Poly(2,2'-Bipyridine-5,5'-Diyl), and their K-Doped States. *J. Chem. Phys.*, **1995**, *103*, 2738.
- ⁴⁵ Vaschetto, M. E.; Monkman, A. P.; Springborg, M.; Vaschetto, M. E.; Monkman, A. P.; Springborg, M. First-Principles Studies of Some Conducting Polymers: PPP, PPy, PPV, PPyV, and PANI. *J. Mol. Struct. THEOCHEM* **1999**, *468*, 181–191.
- ⁴⁶ Hill, I. G.; Kahn, A.; Soos, Z. G.; Pascal Jr, R. A. Charge-Separation Energy in Films of π -Conjugated Organic Molecules. *Chem. Phys. Letters*, **2000**, *327*, 181–188.

1
2
3
4
5
6
7
8
9
10
11
12
13
14
15
16
17
18
19
20
21
22
23
24
25
26
27
28
29
30
31
32
33
34
35
36
37
38
39
40
41
42
43
44
45
46
47
48
49
50
51
52
53
54
55
56
57
58
59
60

⁴⁷ Hutchison, G. R.; Zhao, Y.-J.; Delley, B.; Freeman, A. J.; Ratner, M. A.; Marks, T. J.

Electronic Structure of Conducting Polymers: Limitations of Oligomer Extrapolation

Approximations and Effects of Heteroatoms. *Phys. Rev. B* **2003**, *68*, 035204.

On-surface photodissociation of C-Br bonds: towards room temperature Ullmann coupling

This work proves that a light stimulus can be used to trigger the on-surface C-Br bonds photo-dissociation of a halogenated polycyclic aromatic hydrocarbon, namely 5,11-dibromo-tetracene (DBT), deposited as a monolayer on the Au(111) surface. More precisely, we have studied this sterically hindered precursor with respect to the Ullmann coupling reaction in order to observe specific spectroscopic and topological fingerprints associated with the organometallic intermediates obtained after the C-Br homolytic dissociation.

The results are of general interest in the Ullmann coupling topic. Indeed, one of the main limitations to obtain highly-ordered covalent networks on gold is the high temperature treatment required to dissociate the C-Br bond (120°C), due to the low catalytic activity of gold. These treatment usually leads to massive molecular desorption and/or decomposition. In this view mild reaction conditions are strictly required to significantly improve the quality of the resulting covalent network. Our work unambiguously reveals that an UV treatment can be used to overcome the rate determining step for the thermal reaction by triggering the C-Br dissociation already at room temperature (RT). In this way, after a low temperature annealing (50°C) a highly ordered organometallic network is obtained without molecular desorption and decomposition.

Complementary DFT modelling has highlighted how chemisorbed bromine significantly stabilizes the organometallic structure formed as a consequence of the C-Br photo-dissociation. In fact, the partially negative bromine atoms attractively interact with terminal gold adatoms providing a stabilization as high as 0.4 eV per unit cell.

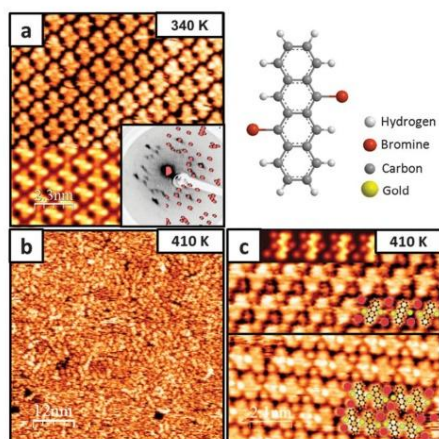


Fig. 1 STM images of the dark area: (a) monolayer of DBT molecules deposited on Au(111) with superimposed DFT simulation (inset: 17 eV experimental and [3.35; 0.5] simulated LEED patterns); (b) representative image of the surface after annealing at 410 K; (c) zoom-in of one of the rare ordered areas obtained after annealing at 410 K; the superimposed models highlight the presence of the organometallic dimers and the chemisorbed bromine. Tunneling parameters are (a) $I = 3$ nA, $V_{\text{bias}} = 0.67$ V; (b) $I = 2.5$ nA, $V_{\text{bias}} = -0.52$ V; (c) $I^{\text{upper}} = 1.5$ nA, $V_{\text{bias}}^{\text{upper}} = 0.69$ V; $I^{\text{bottom}} = 3.6$ nA, $V_{\text{bias}}^{\text{bottom}} = -0.1$ V.

Fig. 1a shows a STM image of a full monolayer of DBT after thermal desorption of the partially formed second layer at 340 K, showing that the Au(111) surface is covered by a well-organized superstructure whose periodicity is described by the [3.35; 0.5] epitaxial matrix, as confirmed by the LEED pattern. The main molecular axis lies along the [110] substrate direction and, according to the DFT simulated unit cell, each Br substituent can interact attractively with a partial positive charge residing on an H atom of the adjacent molecule to form a Br...H intermolecular interaction, $d_{\text{Br}\cdots\text{H}} \approx 3.3$ Å, which favours the formation of an ordered network.¹⁹ At RT the Au herringbone reconstruction is neither modified nor lifted upon adsorption of the molecules, indicating a weak molecule–substrate interaction. DFT calculations of a physisorbed monolayer provide a distance from the substrate of 3.2 Å and a binding energy of 2.0 eV per DBT, typical of a weakly interacting system driven by van der Waals forces and a tiny electron transfer effect (see the ESI† Fig. S1). XPS further corroborates the hypothesis that DBT molecules are intact at RT. Indeed, as reported in Fig. 2a, the Br 3d core level reveals the existence of almost exclusively carbon-bonded bromine (Br 3d_{5/2} BE = 69.7 eV).²⁰ Moreover, both the C 1s:Br 3d ratio (9.3:1) and the ratio between the different components of the C 1s peak, namely C–H:C–C:C–Br (5:3.2:1), are in agreement with the expected values for the intact molecules.

To study the thermo- and light-induced C–Br homolytic bond cleavage, we irradiate half of the surface of the Au single crystal at $\lambda = 405$ nm for 12 hours at RT. In this way a direct comparison of the effect of the annealing treatments on the two different areas is made possible.

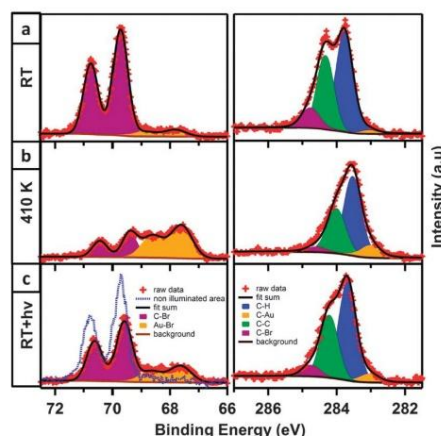


Fig. 2 Br 3d ($h\nu = 150$ eV) and C 1s ($h\nu = 400$ eV) XPS spectra and fitting components of (a) the DBT monolayer on Au(111); (b) the DBT monolayer after annealing at 410 K; (c) the DBT monolayer after illumination at RT. The blue dotted line in (c) reports the Br 3d peak from the non-illuminated area of the same sample.

Fig. 1 reports the thermal behaviour of the non-illuminated area: when the deposited monolayer (Fig. 1a) is annealed at a temperature lower than 410 K, no noticeable effects are observed, while after treatments at 410 K (Fig. 1b) the quality of the resulting surface is very poor, with partial desorption–decomposition of the DBT precursor. XPS analysis (Fig. 2b) indicates a consistent coverage decrease ($\approx 19\%$) with respect to the RT surface probably related to the low sublimation temperature of the precursor, as reported in the Experimental section.

Little islands wherein molecules are ordered have been found sporadically. Fig. 1c reports two of these areas formed by monomeric and dimeric species, the latter consisting of two tetracene units interconnected by a bridging bright dot and with two brighter terminal features at both their sides (yellow circles in Fig. 1c). Moreover, additional circular features are discernible between successive dimers (red circles in Fig. 1c). According to literature data,^{9,21} we propose that the observed monomers and dimers are formed by tetracene units, where bromine atoms have been substituted by gold atoms (yellow circles). The additional bumps between the molecules are the residual chemisorbed bromine (red circles), as visualized by the atomic model superimposed to the STM images (see also the ESI† for optimized DFT monomeric and dimeric structures in Fig. S3a and S4a, respectively). It is noteworthy that two chemisorbed bromine atoms laterally cap a couple of adjacent terminal (mono-coordinated) Au atoms belonging to successive dimers in a 1:1 ratio, while no bromine atoms are associated with the single bridging (twofold-coordinated) Au atom within each individual dimer. As a further proof of the organometallic nature of the dimers, STM analysis shows that the centre-to-centre distance within a dimer is 0.65 ± 0.03 nm, significantly larger than the expected value for directly linked phenyl rings, e.g. nearest neighbour phenylene groups in poly(*para*-phenylene) (0.43 nm),²² but in agreement with that

expected for an organometallic structure.^{12,23} Moreover, the lifted herringbone Au(111) reconstruction (see Fig. 1b) suggests that the incorporated Au atoms are partially provided by surface reordering.¹³

C 1s XPS analysis further corroborates this scenario, since the area of the component at lower binding energy, usually associated with carbon bonded to metal atoms,^{20,23} increases at the expense of the C–Br related peak: starting from 12%, the percentage of metal-bonded carbon ($100 \cdot \text{area}_{\text{C-Au}} / (\text{area}_{\text{C-Au}} + \text{area}_{\text{C-Br}})$) becomes 74%, see Fig. 2b. Moreover, the whole C 1s peak rigidly shifts towards lower BE (≈ 0.2 eV), as a consequence of both bromine chemisorption^{24,25} and lifting the herringbone reconstruction.¹¹ Regarding the circular protrusions between the organometallic species, the XPS bromine spectra highlight the presence of mainly chemisorbed Br (Br 3d_{5/2} BE 67.8 eV),²⁰ so we associate these features with chemisorbed bromine, as anticipated before. Finally, the DFT simulated images, based on the aforementioned model and fully optimized atomic structures, well reproduce the experimental features, such as the brightness of Br side atoms (see the inset in Fig. 1a) and the contrast between the molecular cores and the surface adsorbed Br atoms (see the inset in Fig. 1c).

As observed for sterically hindered organic scaffolds,^{12,26} the flat geometry of the DBT molecules maximizes the interaction with the Au(111) surface, but at the same time inhibits the metal elimination step of the Ullmann-like coupling reaction, so that the final C–C coupling is hampered. Even if at 410 K the C–Br bond is activated, the resulting organometallic network contains mainly dimeric and monomeric species while longer oligomers are randomly observed. Previous studies^{1,8} show that large organometallic islands of metal-interconnected monomers are usually obtained due to the reversible nature of the carbon–metal–carbon bonds, while for DBT this is not the case even after annealing at higher temperature. As reported in Fig. 2b, the Br 3d area amounts to 53% of the as-deposited signal and only 27% is related to carbon-bonded bromine (14% of the initial amount), so that an incomplete de-bromination cannot justify the low polymerization degree. Even the availability of gold adatoms cannot justify this evidence, since longer oligomers require smaller amounts of metal atoms. A possible key to this behaviour is given by the presence of bromine atoms regularly lying adjacent to the terminal, mono-coordinated gold adatoms both in the dimers and the monomers, which suggests that they contribute to the stabilization of these species.^{6,27} In fact, DFT simulations show that gold adatoms singly-bonded to tetracene cores are electron-deficient, in the sense that a partial positive charge resides on them (see discussion in the ESI† and Fig. S2). For this reason chemisorbed Br atoms attractively interact with two neighbouring terminal Au atoms of gold-substituted tetracene molecules, thus stabilizing the formation of the ordered network. More precisely, our DFT calculation shows that the experimental-like unit cell that contains two Br atoms is 0.4 eV more stable than the same cell without the bromines, which are assumed to adsorb far from the self-assembled structure in the latter case (see Fig. S3 and S4, ESI† for details). We cannot exclude that other factors affect the observed outcome, such as

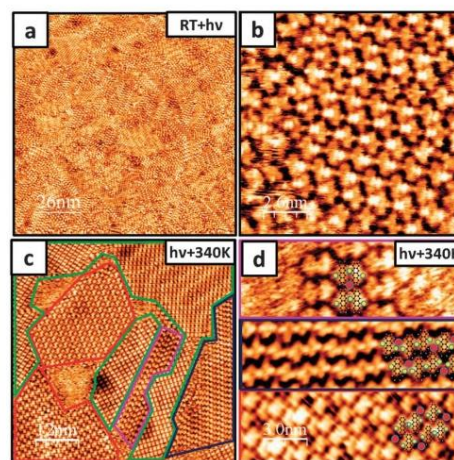


Fig. 3 STM images of the illuminated area. (a and b) Monolayer of DBT molecules irradiated at RT; (c) the same surface after annealing at 340 K. Islands with different ordered nanostructures are contoured with different colours; more precisely, the green islands are formed by brominated DBT while the red, blue and cyan islands by organometallic monomers or dimers. (d) Zoom-in of the islands formed by organometallic molecules. Tunneling parameters are (a and b) $I = 4$ nA, $V_{\text{bias}} = 0.99$ V; (b and c) $I = 3.2$ nA, $V_{\text{bias}} = 0.52$ V.

the lattice mismatch between the surface and the periodicity of the oligomers, which could favour the formation of ordered island of dimers and monomers.

In summary, even if at 410 K the C–Br bond is activated, the quality of the resulting surface is very poor, with large disordered areas due to the partial desorption or decomposition of DBT molecules. By increasing the annealing temperature the quality of the resulting surface is even worse and the formation of direct C–C bonds is not observed, see Fig. S5 (ESI†).

Moving to the illuminated area, reported in Fig. 3, after the irradiation at RT (Fig. 3a) we observe a strong variation of the topography: the herringbone reconstruction disappears within large area and the surface appears to be more disordered, even if the coverage does not change, *i.e.* the C 1s area is unaffected by the treatment. Fig. 3b shows that, even if the as-deposited DBT molecules are still present, the majority of the surface is covered by organometallic species: indeed, bright dots as those observed after thermal activation of the precursors are clearly visible at the sides of the molecules. As before, when the bright dots appear, the underlying herringbone reconstruction is lifted, confirming that the bright dots are Au adatoms. Furthermore, the XPS analysis reveals the light-induced activation of the C–Br bond. Fig. 2c reports the comparison of the Br 3d doublet measured on illuminated *versus* dark sample regions. Within the illuminated area the bromine signal is split into two components. Indeed, an additional Br 3d doublet appears at 67.8 and 68.8 eV accounting for 27% of the total signal area, indicating the presence of surface-stabilized bromine atoms.^{20,28} The total subtended area decreases by 22% with respect to the dark

sample regions, suggesting that part of the bromine desorbs during the irradiation and that the reaction yield is about 45%, see discussion below Fig. S6 (ESI†).

After mild annealing at 340 K, unable to trigger the thermal dissociation of the C–Br bond (Fig. S6, ESI†), the order of the illuminated area is strongly enhanced, as shown in Fig. 3c. The dark area, instead, is unaffected by this treatment since only the as-deposited structure is observed. In the illuminated area two types of ordered islands are well distinguishable: the one above the Au(111) herringbone reconstructed surface (contoured with green lines in Fig. 3c), where the as-deposited DBT structure is still present, and those on the un-reconstructed surface (contoured with red, blue and cyan lines in Fig. 3c and d), where different ordered nanostructures of organometallic monomers and dimers are visible according to the different bonding schemes obtainable from the asymmetric functionalization of the tetracene core. These organometallic ordered structures are the same that are obtained by annealing at 410 K: the main difference is that the coverage does not decrease and the order is strongly improved due to the low temperature treatment in the light-triggered surface reaction. Remarkably, even with this light-triggered procedure longer oligomeric chains are not formed. As the temperature is increased above 410 K, the illuminated and dark regions become microscopically and spectroscopically indistinguishable, with a decrease of the coverage and the structural order.

In summary, by combining UHV-STM, XPS and DFT we have shown that a light stimulus can be used to trigger the first step of the Ullmann coupling reaction. In particular, the irradiation procedure leads to the C–Br bond cleavage at RT rather than at 410 K, thus allowing one to obtain a completely ordered organometallic network after mild annealing. Since it has to be noted that the light-induced debromination in the gas-phase occurs at shorter wavelengths, it appears reasonable then to imagine an active role of the substrate in the observed reactivity by mean the known indirect excitation process.²⁹ Our precursor (5,11-dibromo-tetracene) cannot further react due to steric hindrance between the units. For this reason differently functionalized molecules will be studied to highlight the differences between thermal and photochemical activation under steric conditions allowing for Ullmann coupling completion. An orthogonal activation of the polymerization with respect to the extensively applied thermal treatments may be of particular interest to improve the quality of the covalent organic networks. In this sense, a light-triggered C–Br dissociation offers a new possible way to combine halogens with other functional groups to exploit a hierarchical synthesis, wherein sequential light and thermal treatments may be applied to polymerize a bi-functional precursor.

This work has been partially funded by MIUR (PRIN 2010/11, Project No. 2010BNZ3F2: “DESCARTES”), Progetti di Ricerca di Ateneo (CPDA118475/11), Progetto Futuro in Ricerca 2012 (RBFR128BEC) and by CINECA supercomputing center through LI03p_CBC4FC and IsrB_CMGEC4FC grants.

Notes and references

- Q. Fan, C. Wang, Y. Han, J. Zhu, W. Hieringer, J. Kuttner, G. Hilt and J. M. Gottfried, *Angew. Chem., Int. Ed. Engl.*, 2013, **52**, 4668–4672.
- J. Cai, P. Ruffieux, R. Jaafar, M. Bieri, T. Braun, S. Blankenburg, M. Muoth, A. P. Seitsonen, M. Saleh and X. Feng, *et al.*, *Nature*, 2010, **466**, 470–473.
- F. Sedona, M. Di Marino, M. Sambì, T. Carofiglio, E. Lubian, M. Casarin and E. Tondello, *ACS Nano*, 2010, **4**, 5147–5154.
- R. Lindner and A. Kühnle, *ChemPhysChem*, 2015, **16**, 1582–1592.
- L. Lafferentz, V. Eberhardt, C. Dri, C. Africh, G. Comelli, F. Esch, S. Hecht and L. Grill, *Nat. Chem.*, 2012, **4**, 215–220.
- J. Park, K. Y. Kim, K. H. Chung, J. K. Yoon, H. Kim, S. Han and S. J. Kahng, *J. Phys. Chem. C*, 2011, **115**, 14834–14838.
- W. Wang, X. Shi, S. Wang, M. a. Van Hove and N. Lin, *J. Am. Chem. Soc.*, 2011, **133**, 13264–13267.
- M. Bieri, S. Blankenburg, M. Kivala, C. a. Pignedoli, P. Ruffieux, K. Müllen and R. Fasel, *Chem. Commun.*, 2011, **47**, 10239–10241.
- J. Eichhorn, D. Nieckarz, O. Ochs, D. Samanta, M. Schmittel, P. J. Szabelski and M. Lackinger, *ACS Nano*, 2014, **8**, 7880–7889.
- Q. Fan, C. Wang, L. Liu, Y. Han, J. Zhao, J. Zhu, J. Kuttner, G. Hilt and J. M. Gottfried, *J. Phys. Chem. C*, 2014, **118**, 13018–13025.
- A. Basagni, F. Sedona, C. A. Pignedoli, M. Cattelan, L. Nicolas, M. Casarin and M. Sambì, *J. Am. Chem. Soc.*, 2015, **137**, 1802–1808.
- A. Saywell, W. Greñ, G. Franc, A. Gourdon, X. Bouju and L. Grill, *J. Phys. Chem. C*, 2014, **118**, 1719–1728.
- H. Zhang, J. H. Franke, D. Zhong, Y. Li, A. Timmer, O. D. Arado, H. Mönig, H. Wang, L. Chi and Z. Wang, *et al.*, *Small*, 2014, **10**, 1361–1368.
- J. Björk, F. Hanke and S. Stafström, *J. Am. Chem. Soc.*, 2013, **135**, 5768–5775.
- A. Basagni, L. Colazzo, F. Sedona, M. DiMarino, T. Carofiglio, E. Lubian, D. Forrer, A. Vittadini, M. Casarin and A. Verdini, *et al.*, *Chemistry*, 2014, **20**, 14296–14304.
- H. Y. Gao, D. Zhong, H. Mönig, H. Wagner, P. A. Held, A. Timmer, A. Studer and H. Fuchs, *J. Phys. Chem. C*, 2014, **118**, 6272–6277.
- Q. Shen, J. H. He, J. L. Zhang, K. Wu, G. Q. Xu, A. T. S. Wee and W. Chen, *J. Chem. Phys.*, 2015, **142**, 101902.
- K.-H. Chung, B.-G. Koo, H. Kim, J. K. Yoon, J.-H. Kim, Y.-K. Kwon and S.-J. Kahng, *Phys. Chem. Chem. Phys.*, 2012, **14**, 7304–7308.
- T. A. Pham, F. Song, M.-T. Nguyen and M. Stöhr, *Chem. Commun.*, 2014, **50**, 14089–14092.
- K. A. Simonov, N. A. Vinogradov, A. S. Vinogradov, A. V. Generalov, E. M. Zagrebina, N. Mårtensson, A. A. Cafolla, T. Carpy, J. P. Cunniffe and A. B. Preobrajenski, *J. Phys. Chem. C*, 2014, **118**, 12532–12540.
- J. Eichhorn, T. Strunskus, A. Rastgoo-Lahrood, D. Samanta, M. Schmittel and M. Lackinger, *Chem. Commun.*, 2014, **50**, 7680–7682.
- J. a. Lipton-Duffin, O. Ivasenko, D. F. Perepichka and F. Rosei, *Small*, 2009, **5**, 592–597.
- M. Di Giovannantonio, M. El Garah, J. Lipton-Duffin, V. Meunier, L. Cardenas, Y. Fagot Revurat, A. Cossaro, A. Verdini, D. F. Perepichka and F. Rosei, *et al.*, *ACS Nano*, 2013, **7**, 8190–8198.
- A. Batra, D. Cvetko, G. Kladnik, O. Adak, C. Cardoso, A. Ferretti, D. Prezzi, E. Molinari, A. Morgante and L. Venkataraman, *Chem. Sci.*, 2014, **5**, 4419–4423.
- M. Chen, J. Xiao, H. P. Steinrück, S. Wang, W. Wang, N. Lin, W. Hieringer and J. M. Gottfried, *J. Phys. Chem. C*, 2014, **118**, 6820–6830.
- L. Ferrighi, I. Piš, T. H. Nguyen, M. Cattelan, S. Nappini, A. Basagni, M. Parravicini, A. Papagni, F. Sedona and E. Magnano, *et al.*, *Chem. – Eur. J.*, 2015, **21**, 5826–5835.
- H. Zhang, H. Lin, K. Sun, L. Chen, Y. Zagranjarski, N. Aghdassi, S. Duhm, Q. Li, D. Zhong and Y. Li, *et al.*, *J. Am. Chem. Soc.*, 2015, **137**, 4022–4025.
- A. Lunghi and F. Totti, *J. Mater. Chem. C*, 2014, **2**, 8333–8343.
- J. Lee, S. Ryu, J. Chang, S. Kim and S. K. Kim, *J. Phys. Chem. B*, 2005, **109**, 14481–14485.

Stereoselective photopolymerization of tetraphenylporphyrin derivatives on Ag(110) at the sub-monolayer level

This study proves that a light stimulus can be used to trigger the on-surface polymerization of a tetra-phenyl porphyrin derivative, namely 5,15-bis(4-aminophenyl)-10,20-diphenylporphyrin (*trans*-TPP(NH₂)₂) in the sub-monolayer coverage range on the Ag(110) surface. More precisely, our results reveal that the reaction proceeds with the formation of azo-bridges (Ph-N=N-Ph) between the molecular building blocks.

This proof of principle is of general interest in the field of surface-supported systems, since it represents an example of how light can be used to activate functional groups otherwise silent with respect to thermal treatments. In addition, this approach offers a way to overcome the limitations posed by the close relationship between molecular surface mobility, chemical reactivity and temperature. Indeed, the ability to separately control the reaction initiation and the surface mobility by light stimuli and temperature, respectively, is found to be a critical degree of freedom to get an extended ordered structure. We show that by reducing the surface mobility, i.e. by working at low temperature (100 – 300 K), it is possible to apply a low-to-high surface molecular density approach, which helps preventing the formation of compact, non-covalent structures. Meanwhile, the chemical reaction between slowly diffusing monomers is independently triggered by irradiation at a suitable wavelength. The quantitative formation of a new, long-range ordered and covalently-bonded super-structure is thus obtained.

Finally, this study represents a step forward in the application of organic photochemistry to on-surface synthesis, which is currently limited to the use of diacetylene groups, and it opens up new opportunities for using several organic functional groups as photoactive centers for the synthesis of covalent organic frameworks.

CHEMISTRY

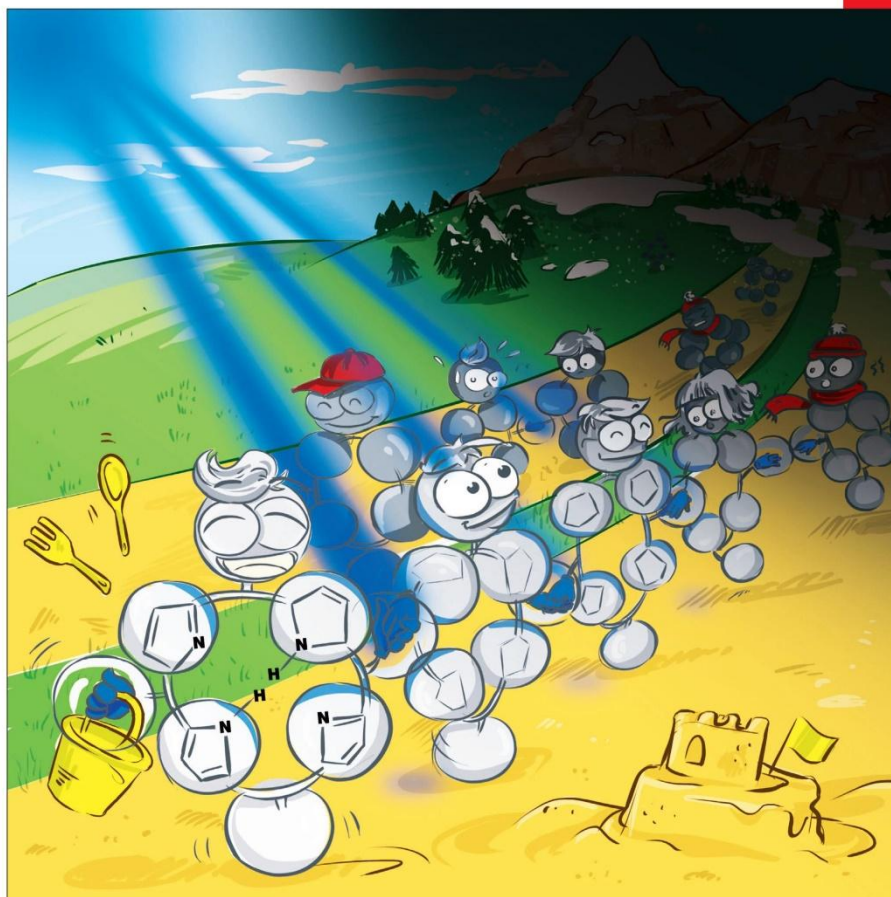
A European Journal

www.chemeurj.org

A Journal of



2014-20/44



Cold regions ...

... (the mountain chain in the illustration) and warm areas (the beach in the foreground) represent the temperature ramp applied to obtain extended molecular wires under illumination at the sub-monolayer level. The transurance of amino-functionalized porphyrins along the close-packed atomic rows (the parallel roads) of the cold Ag(110) surface ends at the beach, where light induces their union (covalent bonding) as soon as they approach each other. For more details, see the Full Paper by A. Basagni et al. on page 14296 ff.

Supported by

ACES

WILEY-VCH

Surface Photochemistry | Hot Paper |


Stereoselective Photopolymerization of Tetraphenylporphyrin Derivatives on Ag(110) at the Sub-Monolayer Level

Andrea Basagni,^{*,[a]} Luciano Colazzo,^[a] Francesco Sedona,^{*,[a]} Marco Di Marino,^[a] Tommaso Carofiglio,^[a] Elisa Lubian,^[a] Daniel Forrer,^[b, c] Andrea Vittadini,^[b, c] Maurizio Casarin,^[a, b, c] Alberto Verdini,^[d] Albano Cossaro,^[d] Luca Floreano,^[d] and Mauro Sambi^[a, b]

Abstract: We explore a photochemical approach to achieve an ordered polymeric structure at the sub-monolayer level on a metal substrate. In particular, a tetraphenylporphyrin derivative carrying *para*-amino-phenyl functional groups is used to obtain extended and highly ordered molecular wires on Ag(110). Scanning tunneling microscopy and density functional theory calculations reveal that porphyrin building blocks are joined through azo bridges, mainly as *cis* isomers. The observed highly stereoselective growth is the result of adsorbate/surface interactions, as indicated by X-ray photo-

electron spectroscopy. At variance with previous studies, we tailor the formation of long-range ordered structures by the separate control of the surface molecular diffusion through sample heating, and of the reaction initiation through light absorption. This previously unreported approach shows that the photo-induced covalent stabilization of self-assembled molecular monolayers to obtain highly ordered surface covalent organic frameworks is viable by a careful choice of the precursors and reaction conditions.

Introduction

Over the past few years, synthesis of organic surface-supported covalent nanostructures has gained substantial interest for the preparation of low-dimensional materials.^[1,2] These are highly interesting from a basic science perspective, but also for nanotechnological applications such as template-assisted nanopatterning^[3] and organic electronics.^[4] Molecular self-assembly is a widely applied tool for creating ordered organic structures on surfaces and indeed many arrangements have been produced in ultrahigh-vacuum (UHV) conditions, ranging from wirelike structures^[5] and two dimensional layers^[6] to more complex architectures such as host-guest networks.^[7–9] Formation and stabilization of self-assembled structures can be

driven by intermolecular interactions such as metal-ligand coordination^[10–12] and hydrogen bonding,^[13–17] but also by the weaker and non-directional van der Waals interactions.^[18–20] The weakness of these interactions makes the network formation reversible, which, on one hand, favors defect correction, and, ultimately, the formation of long-range ordered structures. On the other hand, instability is a severe limitation for ex situ applications in ambient environment.

In recent years, direct on-substrate synthesis in UHV has been exploited as a promising strategy to obtain thermally and chemically stable structures by covalent bonding of suitable precursors.^[21] The 2D confinement of molecular precursors has many advantages over 3D solution chemistry, such as the possibility of preparing large molecules impossible to synthesize in solution owing to their low solubility, better control of the system architecture through the use of a pretemplating substrate, and finally access to new reaction pathways, thanks to the catalytic role of the substrate.^[22,23] Usually, covalent linking of organic molecules onto metal and bulk insulator surfaces is carried out thermally: the energy supplied to the system promotes substitution reactions^[24–27] or activates the precursors by C–Br or C–I homolytic dissociation.^[28–32] These approaches, however, perform monomer assembly and polymerization simultaneously under dynamic-bond-forming conditions, and usually provide polymers with many defects and only short-range order.^[33] A reversible reaction environment might improve the surface covalent organic frameworks (SCOF) quality,^[34–36] but typically thermodynamic equilibrium conditions cannot be achieved in UHV.

[a] A. Basagni, L. Colazzo, F. Sedona, M. Di Marino, Prof. T. Carofiglio, E. Lubian, Prof. M. Casarin, Prof. M. Sambi
Dipartimento di Scienze Chimiche
Università di Padova
Via Marzolo 1, 35131, Padova (Italy)
E-mail: andrea.basagni@studenti.unipd.it
francesco.sedona@unipd.it

[b] D. Forrer, A. Vittadini, Prof. M. Casarin, Prof. M. Sambi
Consorzio INSTM
Via Marzolo 1, 35131 Padova (Italy)

[c] D. Forrer, A. Vittadini, Prof. M. Casarin
CNR-IEI
Via Marzolo 1, 35131 Padova (Italy)

[d] A. Verdini, A. Cossaro, L. Floreano
Laboratorio Nazionale TASC
Area Science Park
S. S. 14, km 163.5, 34149 Trieste (Italy)

Photochemically activated reactions, instead, have proven to be a powerful tool to stabilize the self-organized structures without disrupting the long-range order.^[37–39] However, covalent interlinking of molecules by light triggering on metal substrates poses additional challenges. First of all, the high quenching rate of electronically excited species on metal surfaces inhibits the photophysical processes commonly observed in the gas phase and in solution.^[40] Moreover, the presence of the surface can also provide new relaxation pathways, such as photodesorption,^[41,42] and new charge-transfer-mediated photochemistry.^[43,44] As a result, the surface photochemistry of a given molecule is considerably different from what would be anticipated for a gas-phase or solution environment. These are some of the reasons why light-driven on-surface synthesis is not as developed as it is in solution.

Herein, we present the covalent coupling of a tetraphenyl porphyrin derivative, namely 5,15-bis(4-aminophenyl)-10,20-diphenylporphyrin (hereafter, *trans*-TPP(NH₂)₂). The aniline moiety is known to adsorb on and interact with a silver substrate much like phenol^[45] and both molecules display similar photophysical behavior in the gas phase.^[46,47] In particular, the N–H bond photodissociation threshold was estimated at 4.61 eV, that is approximately 0.4 eV lower than the O–H analogue in phenol^[48,49]—we therefore expect that aniline residues can form radicals on the silver surface, as reported for phenol.^[48,49] Here, the anilino radical formation is employed to covalently bond *trans*-TPP(NH₂)₂ monomers by a radical coupling reaction. Our results indicate that porphyrins form nanowires extending along the substrate [110] direction and that the monomers are joined by N=N (azo) links. N 1s X-ray photoelectron spectroscopy (XPS) measurements show that the substrate takes an active part in the stabilization of the formed bond and in its stereochemistry.

The interest for such a prototype reaction is tightly linked to the use of radical photodissociation reactions between organic chromophores as a tool for the covalent stabilization of highly ordered surface supramolecular structures. Moreover, light-induced topochemical processes exploiting small fragments (H[•] or CH₃[•] radicals) as leaving groups, not directly involved in the self-assembly process, are expected to induce minor conformational rearrangements, thus minimizing the probability of generating structural defects.

Results and Discussion

As reported in previous studies,^[8,9] *trans*-TPP(NH₂)₂ molecules deposited on Ag(110) at room temperature (RT) self-organize in an ordered structure, Figure 1a. This is characterized by an oblique unit cell, which is commensurate with the substrate, and described by the epitaxial matrices (5 ± 2, ∓2 3), hereafter referred to as “oblique phase”.

We first checked the effects of 10 h of irradiation at λ = 405 nm on 0.5 monolayer (ML) *trans*-TPP(NH₂)₂ deposited on Ag(110) at RT. As shown in Figure 1c, the low-energy electron diffraction (LEED) pattern still displays the same (5 ± 2, ∓2 3) symmetry observed before irradiation. Nevertheless, within the sample illuminated area, some porphyrins exhibit a decrease of

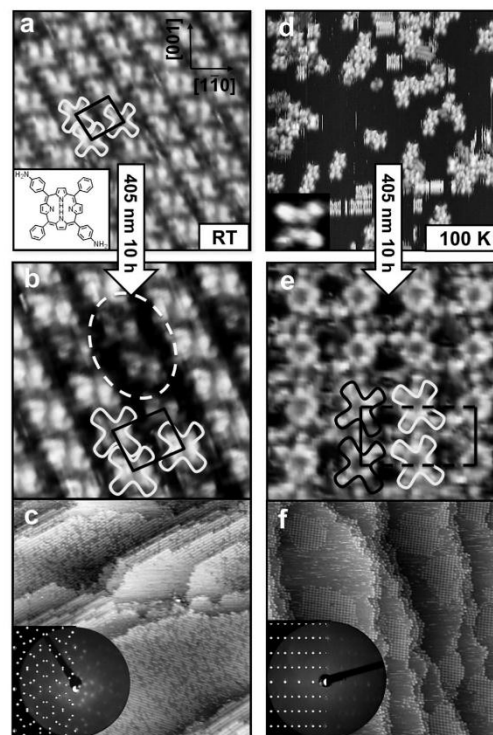


Figure 1. a) STM image of the oblique (5 ± 2, ∓2 3) self-assembled *trans*-TPP(NH₂)₂ superstructure on Ag(110) at RT with the corresponding molecular structural formula (13 × 13 nm², $V_{\text{bias}} = 0.58$ V, $I = 15.20$ nA). b) Small-scale (7 × 7 nm², $V_{\text{bias}} = 0.45$ V, $I = 3.20$ nA), and c) large-scale (150 × 150 nm², $V_{\text{bias}} = 1.00$ V, $I = 1.00$ nA) STM images and LEED pattern with superimposed simulation of the oblique structure illuminated for 10 h at RT. d) STM image of *trans*-TPP(NH₂)₂ on Ag(110) at 100 K (30 × 30 nm², $V_{\text{bias}} = 0.30$ V, $I = 1.00$ nA; inset 2.4 × 2.4 nm², $V_{\text{bias}} = -0.95$ V, $I = 1.94$ nA). e) Small-scale (8 × 8 nm², $V_{\text{bias}} = -1.00$ V, $I = 17.37$ nA) and f) large-scale (150 × 150 nm², $V_{\text{bias}} = 1.00$ V, $I = 1.00$ nA) STM images and LEED pattern with superimposed simulation of the rectangular p(12 × 4) structure obtained by the two-step procedure as described in the text. The superimposed porphyrin shapes highlight the different azimuthal orientation of the molecules in the rectangular phase, which gives rise to the glide symmetry line (dashed line). In all the STM images, the directions lie as indicated in (a).

their apparent height by 0.5 ± 0.1 Å, as highlighted by the dashed oval in Figure 1b; the irradiated molecules also show a reduced mobility over the terraces at RT. These molecular changes (in conformation and mobility) disappear after one hour at 410 K, thus highlighting the metastable nature of the molecular state produced by irradiation.

We found an efficient photoreaction pathway by depositing different amounts of *trans*-TPP(NH₂)₂ on Ag(110) maintained at 100 K. The sample was then illuminated at 405 nm during a linear heating ramp up to RT over approximately 10 h. With this two-step procedure, the formation of a new extended su-

perstructure is observed for coverage lower than about 0.5 ML (Figure 1 f). At higher coverage, the oblique structure develops, whereas at very low coverage, step decoration occurs. As shown in Figure 1 d, porphyrin molecules deposited at 100 K are randomly distributed owing to the low mobility, and are mostly aggregated as disordered small clusters. The new superstructure only develops when molecules are irradiated during the slow heating ramp up to RT, that is, during the self-assembly process. Conversely, if molecules are first exposed to the light at 100 K and then heated to RT in the dark, they organize into the known oblique structure.

Figure 1 e and f show small- and large-scale STM images of the new photo-induced phase, together with the corresponding measured and simulated LEED patterns that are consistent with a commensurate $p(12 \times 4)$ superstructure, hereafter referred to as "rectangular phase". The systematic absence of the $(2n + 1, 0)$ diffraction spots in LEED patterns indicates the presence of a glide line symmetry operation parallel to the b_2 unit vector. The STM images reveal a rectangular unit cell, in agreement with the LEED pattern, Figure 1 e, where it is also evident that two adjacent porphyrins along the $[1\bar{1}0]$ direction display a mirror-like azimuthal orientation. This alternation is the origin of the observed glide line symmetry, represented in Figure 1 e by a dashed line. The reported unit cell contains two molecules, so that the surface density (ρ_s) in the rectangular structure is 0.37 nm^{-2} , 16% lower than in the oblique phase (0.44 nm^{-2}). The large-scale STM image in Figure 1 f shows that the new rectangular phase forms extended domains on terraces within the illuminated area.

As observed in several self-organized structures of TPP derivatives,^[50,51] the self-assembly driving force generating the oblique structure is the T interaction between *meso*-phenyl rings (where the H atom of one ring points toward the center of the adjacent ring, as shown in the model of the oblique phase in Figure 2, bottom).

However, geometrical constraints associated with the rectangular phase prevent a full exploitation of these interactions. As a matter of fact, the distances between the phenyl centroids of nearest neighbor (NN) molecules are estimated to be approximately 7.2 and 9.5 Å along the $[1\bar{1}0]$ direction, segments 1 and 3 respectively, and about 7.8 Å along $[1\bar{1}2]$, segment 2, see Figure 2. All these distances are significantly longer than those suitable for T interactions (~ 5 Å), as well as for direct stacking (3.3–3.6 Å) between adjacent benzene rings.^[52–54]

Taking into account the lower ρ_s of the rectangular phase with respect to the oblique one, the stability of this superstructure requires the onset of a highly uni-directional interaction between monomers, stronger than T interaction, such as a covalent bond. As an alternative, a different intramolecular structure (either a conformational change or a structural change due to light-induced intramolecular reactions) could lead to a different organization, for example, owing to changes in the molecular recognition interactions governing the self-assembly process, as well to changes in the molecular size and/or shape.^[55] To get a comparative insight into the structure of oblique and rectangular phases under the same tunneling conditions, we made a RT deposition of *trans*-TPP(NH₂)₂ on a sample partially precovered by the rectangular phase, as shown in Figure 3.

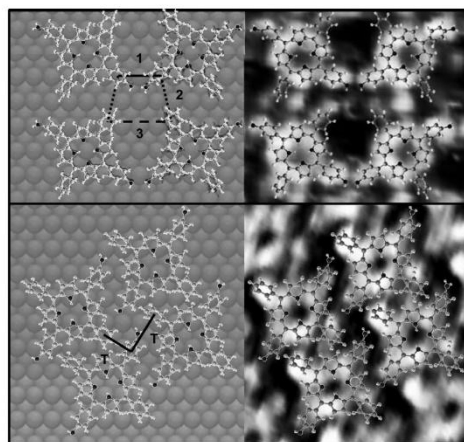


Figure 2. Overlay of STM images and the ball-sticks models of the rectangular (top) and oblique (bottom) structures on the Ag(110) surface. Four segments in the rectangular structure indicate the distances between the phenyl centroids: 1) 0.72 nm, 2) 0.78 nm, 3) 0.95 nm. In the oblique structure, two segments highlight the T interaction between adjacent molecules. The Ag(110) lattice is illustrated by the underlying spheres. The relative positions of the adsorbate and the substrate are chosen arbitrarily. The tunneling parameters are $V_{\text{bias}} = -1.00 \text{ V}$, $I = 17.37 \text{ nA}$ and $V_{\text{bias}} = 1.00 \text{ V}$, $I = 3.47 \text{ nA}$ for the top and bottom images, respectively.

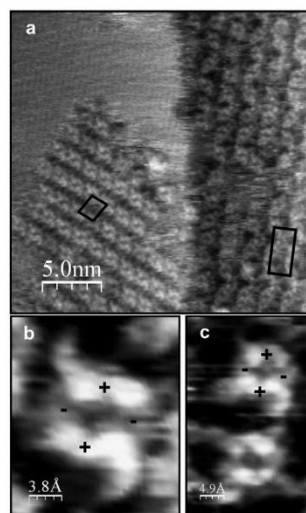


Figure 3. a) STM image ($20 \times 20 \text{ nm}^2$) of the rectangular and oblique structures coexisting on a silver terrace. b) Small-scale image of non-illuminated ($1.5 \times 1.5 \text{ nm}^2$) and c) illuminated TPP(NH₂)₂ ($1.9 \times 3.8 \text{ nm}^2$), the signs "+" and "-" indicate the elevated and depressed macrocycle positions, respectively ($V_{\text{bias}} = -0.51 \text{ V}$, $I = 4.72 \text{ nA}$ for all three images).

The comparison of the small-scale images shows that in both phases the molecules display the so-called saddle shape, a characteristic contrast of the metal-free porphyrin macrocycle.^{156,571} A quantitative analysis of the intramolecular contrast reveals that the difference between the apparent height of up and down pyrrole rings (marked by plus (+) and minus (-) signs in Figure 3) is very similar ($\Delta h_{\text{oblique}} = 0.4 \pm 0.1 \text{ \AA}$ and $\Delta h_{\text{rectangular}} = 0.5 \pm 0.1 \text{ \AA}$) and perfectly in agreement with former reports for TPP on Ag.⁵¹¹ In addition, there is no difference in the apparent porphyrin height with respect to the substrate. The strong similarity of molecules in the rectangular phase with those in the oblique one suggests that no significant change of the central macrocycle structure takes place upon irradiation.

As a direct probe of the *trans*-TPP(NH₂)₂ positioning and molecular unoccupied electronic structure, we compared the near-edge X-ray absorption fine structure (NEXAFS) spectra of the two phases, Figure 4a and b, at different orientations of

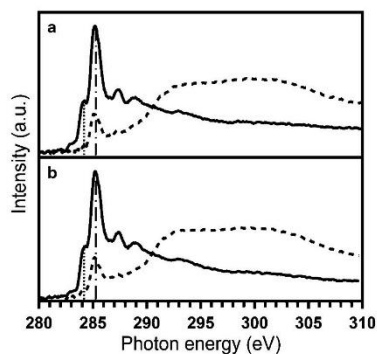


Figure 4. NEXAFS spectra measured by partial electron yield at the C K-edge of oblique (a) and rectangular (b) structures. Two spectra are reported for each sample corresponding to transverse magnetic (solid line) and transverse electric polarization (dashed line). The peaks at 284.1 and 285.2 eV are marked with a dotted and dot-dashed line, respectively.

the surface with respect to the electric field direction.

The C K-edge NEXAFS spectra of the oblique phase are equivalent to those reported for the monolayer phase of H₂-TPP on Ag(111) deposited at RT.⁵⁵¹ Transverse-magnetic (TM) spectra are dominated by the feature at approximately 285.2 eV (dot-dashed line), mainly generated by C^{ph}-based 1s → π* electronic transitions,⁵⁹¹ and the evident shoulder on its lower excitation energy side at approximately 284.1 eV (dotted line), associated with 1s → π* excitations involving macrocycle carbon atoms.⁵⁹¹ Additional resonances in the 286–290 eV range correspond to a mix of higher order π*-symmetry molecular orbitals (MOs) localized on the aromatic atoms and σ*-symmetry MOs associated with C–H bonds. The intensity variation of the NEXAFS resonances observed upon changing the orientation from TM to transverse-electric (TE) (polar dichroism) confirms the preferential orientation of the molecules

and the intensity ratio allows us to determine the average molecular orientation. In particular, we find that the resonance at 284.1 eV vanishes in TE polarization, an observation that implies that the macrocycle is parallel to the surface, whereas the large residual intensity measured in TE polarization at 285.2 eV indicates that the phenyl rings are oriented off the surface with a tilt angle in the range of 30–35°.

The NEXAFS spectra measured in the rectangular phase preserve approximately the same polar dichroism of the oblique phase, thus confirming the absence of significant conformational change upon irradiation.

To understand whether the rectangular phase is a metastable structure rather than the product of a chemical reaction, we studied its thermal stability. Figure 5 shows the comparison between the thermal behavior of the as-deposited *trans*-TPP(NH₂)₂ and of the rectangular phase (a–c and d–f, respectively).

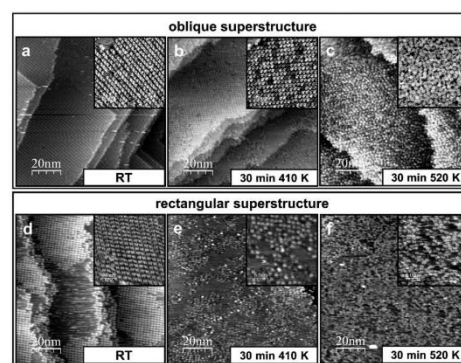


Figure 5. Comparison between the thermal stability of the oblique (a–c) and rectangular (d–f) phases. The temperatures and the annealing times are shown in the figures. All the images have been acquired at RT. Large images: 100 × 100 nm²; insets: 30 × 30 nm². a) $V_{\text{bias}} = 1.80 \text{ V}$, $I = 0.07 \text{ nA}$; inset $V_{\text{bias}} = -0.74 \text{ V}$, $I = 1.71 \text{ nA}$; b) $V_{\text{bias}} = -1.00 \text{ V}$, $I = 1.00 \text{ nA}$; inset $V_{\text{bias}} = 0.65 \text{ V}$, $I = 10.00 \text{ nA}$; c) $V_{\text{bias}} = -0.24 \text{ V}$, $I = 3.66 \text{ nA}$; inset $V_{\text{bias}} = -0.15 \text{ V}$, $I = 2.00 \text{ nA}$; d) $V_{\text{bias}} = 1.00 \text{ V}$, $I = 1.00 \text{ nA}$; inset $V_{\text{bias}} = 0.47 \text{ V}$, $I = 13.05 \text{ nA}$; e) $V_{\text{bias}} = 0.53 \text{ V}$, $I = 7.36 \text{ nA}$; inset $V_{\text{bias}} = 1.00 \text{ V}$, $I = 1.88 \text{ nA}$; f) $V_{\text{bias}} = 1.00 \text{ V}$, $I = 2.58 \text{ nA}$; inset $V_{\text{bias}} = 0.77 \text{ V}$, $I = 7.36 \text{ nA}$.

As far as the oblique structure is concerned, the results of many experiments carried out at the sub-monolayer level are consistent with data reported in ref. [55]. There, it is shown that high-temperature annealing induces a flat molecular conformation as a consequence of the generation of new aryl–aryl carbon bonds between the phenyl rings and the macrocycle. The sequence a–c shown in Figure 5 clearly indicates that, in addition to the total loss of molecular order and mobility, the treatment at 520 K induces changes affecting both the molecular shape (which becomes more rectangular) and the apparent height (molecules appear flattened). On the other hand, annealing at lower temperatures (410 K) promotes the surface ordering of this phase, which therefore appears to be the thermodynamically most stable arrangement before thermal deg-

radation. The rectangular structure instead shows molecular disordering and domain fragmentation already at 410 K (Figure 5e). This excludes the rectangular phase to be a kinetically frozen intermediate stage of the self-assembly mechanism leading to the formation of the oblique phase. The irradiation protocol is thus associated with an irreversible chemical reaction that brings the system into a different thermodynamic path.

The estimated distances between facing *meso*-groups along the $[1\bar{1}0]$ direction indicate that the amino residues might interact when the NN is either a nonfunctionalized phenyl ($d_{NC} \approx 2.9 \text{ \AA}$) or another amino group ($d_{NN} \approx 2 \text{ \AA}$).

To obtain indications on the nature of this interaction, several polymerization schemes of porphyrin monomers have been modelled by referring to the possible nitrogen oxidation states. In Figure 6, we compare the STM images acquired at

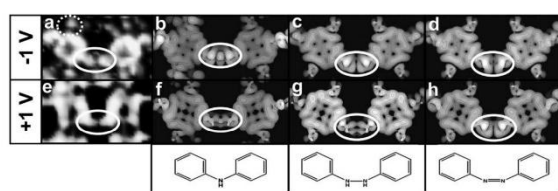


Figure 6. Experimental (a, e) and calculated (b–d), (f–h) STM images of the rectangular superstructure with sketched models of the simulated bonds. The simulated images represent the integrated local density of states between E_f and -1.5 eV (b–d) and between E_f and $+1.5 \text{ eV}$ (f–h), respectively (see Experimental Section). From left to right: the simulations of polyaniline- (b, f), 1,2-diphenylhydrazine- (c, g) and azobenzene-like bonds (d, h) are shown. The white ovals highlight the bond between the units, which are to be compared with the experimentally observed nodal plane structure. The dotted circle marks the cushion effect. (a): $4.3 \times 2.4 \text{ nm}^2$, $V_{\text{bias}} = -1.00 \text{ V}$, $I = 17.37 \text{ nA}$; (e): $4.16 \times 2.59 \text{ nm}^2$, $V_{\text{bias}} = +1.00 \text{ V}$, $I = 6.70 \text{ nA}$.

-1 V ($+1 \text{ V}$) with the simulated STM images of three different models: Figure 6b (6f) shows a polyaniline-like structure with an amino bridge (Ph-NH-Ph)^[60] between the porphyrinic units, whereas both Figure 6c (6g) and 6d (6h) imply the coupling of nitrogen atoms with the formation of a Ph-NH-NH-Ph or a Ph-N=N-Ph group, respectively, which are structurally related either to 1,2-diphenylhydrazine (Figure 6c, g), or to azobenzene (Figure 6d, h). Irrespective of the applied bias, the STM image is characterized by a spread of the integrated density of states over the whole molecule except for the area highlighted with a white oval. In this region, a nodal plane parallel to the $[001]$ substrate direction is clearly visible. In addition, some regular circular bright tunneling features are identifiable between TPP units (dotted circle) only at negative bias. These features have been already observed by some of us^[61] and ascribed to the so-called “cushion effect”. This consists in electron density build-ups in the intermolecular interstices owing to the interaction between the surface and the adsorbate electron clouds.^[62]

It appears that the amino bridge, at both positive and negative bias (Figure 6b and f), does not match the experimental observation, both because the azimuthal orientation of TPP

units differs by several degrees from the experimental evidence and because the nodal plane crossing the bond is missing. Although at negative bias, Figure 6c and d, it is not possible to distinguish between a Ph-NH-NH-Ph and a Ph-N=N-Ph bond, the images simulated at positive bias display some differences. Even if in both models reported in Figure 6g and h TPP units have the correct azimuthal orientation, only the azo group in Figure 6h exhibits a nodal plane crossing the N=N bond as in the experimental STM images. Thus, the azobenzene-like polymeric structure fits best with the real system.

Having accepted this model, it remains to be explained why azobenzene-like structures are almost exclusively in a *cis* configuration, while *trans* structures amount to less than 4% of the surface coverage.

These are observed as linear defects within the rectangular structure and are identifiable by a wavelike pattern, Figure 7.

In these regions, the *trans*-TPP(NH_2)₂ units are shifted by half a lattice parameter along the $[001]$ direction and the position and the mutual orientation of molecules facing each other at the linear defect are compatible with the presence of a *trans* azo bond between the porphyrins, as sketched in Figure 7. Explaining the strong stereoselectivity of the polymerization reaction requires understanding the details of the polymerization mechanism. XPS data give valuable, albeit indirect, information in this respect.

The N1s XPS spectrum from as-deposited *trans*-TPP(NH_2)₂ at RT (Figure 8a) shows two main peaks whose area ratio (R) is 2. As the molecule has three pairs of inequivalent nitrogen atoms (iminic, pyrrolic, and aminic), it is clear that the aminic signal partially

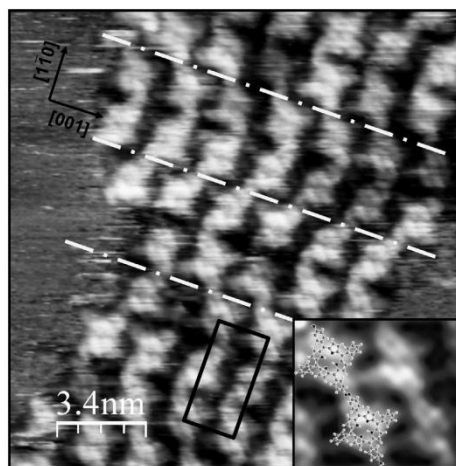


Figure 7. STM image of the linear defects occasionally found within the rectangular structure compatible with the presence of the *trans*-azo geometrical isomer ($17 \times 17 \text{ nm}^2$, $V_{\text{bias}} = 0.09 \text{ V}$, $I = 5.71 \text{ nA}$). Inset: Small-scale STM image of a linear defect with superimposed model ($4.94 \times 4.24 \text{ nm}^2$, $V_{\text{bias}} = 0.09 \text{ V}$, $I = 5.71 \text{ nA}$).

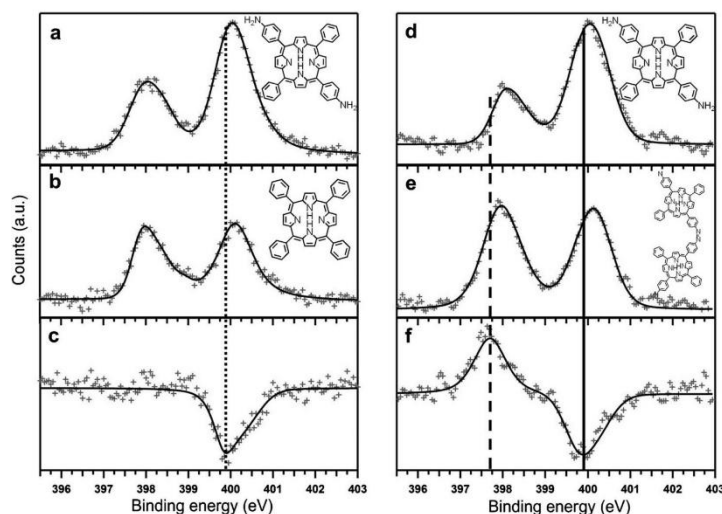


Figure 8. The left panel shows the N 1s XP signals from as-deposited *trans*-TPP(NH₂)₂ (a) and H₂-TPP (b) at RT with the corresponding difference spectrum (c). The right panel shows the N 1s XP spectra from as-deposited *trans*-TPP(NH₂)₂ at 130 K (d) and the rectangular phase (e) acquired on the same sample of (d) after the reaction protocol. The (d)–(e) difference spectrum is shown in (f). The molecular models are superimposed for clarity and the lines mark the positions of the peaks determined by difference.

overlaps with the pyrrolic one, so its position can be determined by difference, Figure 8c, with the spectrum originated from tetraphenylporphyrin (H₂-TPP), Figure 8b. According to this analysis, the pyrrolic peak (–NH–) is found at a binding energy (BE) of 400.1 ± 0.05 eV, the aminic N (–NH₂) at BE = 399.9 ± 0.05 eV, and the iminic N (–N=) at BE = 398.0 ± 0.05 eV; these values are in agreement with previous studies on monolayer phases on Ag.^[63] The effects of the reaction protocol on *trans*-TPP(NH₂)₂ were observed on the same sample by measuring the N 1s XP signals before and after irradiation, Figure 8d and e, respectively. After reaction, the peak area at high BE decreases and is associated with the increase by the same amount of the peak at lower BE, as shown in the difference spectrum in Figure 8f and marked by the solid and dashed lines, respectively. In particular, a new N species arises at 397.7 ± 0.05 eV at the expense of the species at 399.9 eV, previously associated with the amino groups. Although these arguments, supported by literature data that confirm the Ag-supported photocatalyzed formation of azo bonds from primary amines,^[64–68] would suggest a straightforward association of this new component to the azo nitrogen, we note that the expected BE for a simply physisorbed azo group should be higher than the observed one.^[69–72] Chemisorption on metal surfaces generally induces a BE redshift^[73] as consequence of the electron donation from the surface.^[74] In particular, chemisorption through the central azo bridge at the metal surface^[75] can reduce the observed binding energy to 398 eV.^[76] Our results show a new species at 397.7 eV, which can be interpreted as nitrogen azo atoms chemisorbed on silver, in agreement

with the BE observed for diazonium salts grafted on several metal surfaces (397.5 eV).^[77,78] Moreover, the complete dissociation of the azo center can be ruled out because metal-N-Ar nitrogen species lower binding energy values (397–395 eV).^[76,77] In summary, the resulting reaction scenario includes the formation of covalent bonds between the *trans*-TPP(NH₂)₂ through N=N bonds that chemisorb associatively on the silver surface. In turn, this interaction likely promotes the preferential formation of the *cis* isomer.

It appears, then, reasonable to imagine an active role of the substrate in the observed reactivity.

Several photochemical studies^[40,44,79,80] have shown that the absorption of light by metallic substrates produces a hot electron distribution able to populate an adsorbate empty state.

Such a mechanism is known as an indirect excitation process and it may be responsible for photochemical reactions occurring at a noncovalently interacting molecule–metal interfacial system. Besides triggering a reaction through the population of an adsorbate excited state, an indirect excitation may also activate photodissociation processes at longer wavelengths (λ) than those observed in molecular beams. For instance, gas-phase measurements on phenol^[46] indicate that the phenoxyl radical (O–H dissociation) is formed by photoexcitations at $\lambda < 275$ nm, whereas at sub-monolayer coverage on Ag(111) photodissociation takes place at $\lambda = 355$ nm.^[48] Aniline in the gas phase undergoes N–H bond breaking at wavelengths in the range $193.3 \leq \lambda \leq 269.5$ nm, with a photophysical electronic mechanism equivalent to that observed for phenol.^[47]

To our knowledge, no two-photon-photoemission results pertaining to aniline on Ag single-crystal surfaces are available, but it is plausible that irradiation at 405 nm (3.06 eV) could trigger the N–H photodissociation also in *trans*-TPP(NH₂)₂. Within such an assumption, a direct transformation of the oblique phase into the rectangular phase would imply a significant in-plane expansion of the superstructure, which would require a simultaneous highly ordered long-range mass transport with a contextual reorientation of the monomers. However, this only partly explains why the reaction does not proceed at RT. In fact, given the estimated deposition flux (see Experimental Section), the local instantaneous ρ_s is low during deposition. Nevertheless, direct illumination during growth at RT is not efficient in promoting the photoreaction, but it rather leads to the same oblique phase obtained in dark conditions. The role

of the substrate temperature, therefore, proves to be of critical importance in its own right. In the first place, our two-step protocol (low-temperature deposition followed by illumination during slow annealing to RT) provides a separate control of the local density ρ_s (low-density frozen molecules, see Figure 1d) and of the diffusion anisotropy (by preferentially quenching the diffusion along [001],^[81,82] that is, across the compact rows), the subtle balance of which can determine the suitable pairing geometry for the N–H dissociation to take place. In addition, STM images at 100 K (see the inset in Figure 1d) show a molecular shape and contrast (the high density of states on the now clearly visible four peripheral phenyl rings) compatible with a reduction of the dihedral angle between the porphyrin macrocycle and the *meso*-phenyl rings compared with that at RT. A smaller dihedral angle means a shorter distance between the silver surface and the *trans*-TPP(NH₂)₂ amino groups. As the indirect excitation process responsible for the N–H bond breaking is distance-dependent,^[48,83] temperature-induced changes in the adsorbate–substrate distance can affect the efficiency of the photoreaction.

Conclusion

We report on the formation of a new long-range ordered and mainly defect-free SCOF obtained photochemically from *trans*-TPP(NH₂)₂.

The STM images, C K-edge NEXAFS spectra, and thermal stability prove that the rectangular SCOF structure is not metastable and is not due to an intramolecular reaction, which in principle could lead to a different supramolecular organization of the starting monomers. In addition, comparison with DFT simulations and XPS N1s spectra suggest that the protocol used leads to the formation of N=N bonds between porphyrin units, likely through the dissociation of N–H bonds mediated by the metallic substrate. This in turn is shown to play a key role in coupling the monomers by low-coverage/variable-temperature experiments, where the reaction is particularly efficient.

Taking in consideration the mild reaction conditions that have been used, we have obtained evidence that, in this system, light is able to induce reactions that would not occur thermally, and, most importantly, we have shown that light can be used as a further parameter to control the growth of low-density structures. In particular, with a low-to-high density approach the probability of defects formation is reduced because the starting conditions do not sterically prevent the conformational adaptation of the molecules. In contrast, the significant conformational reorganization of a densely packed structure required by a high-to-low density approach promotes frequent improper alignments of the molecular building blocks in the resulting covalent structure, as it is commonly observed in the thermally activated reactions, or it can even hamper the reaction, as observed in this work.

The use of radical photodissociation for the covalent stabilization of the supramolecular structure therefore requires that the initial superstructure does not prevent the conformational changes necessary to lead to the formation of the adduct. A low-to-high surface density approach and the use of small

leaving groups promote the efficient stabilization of the SCOF. In addition, temperature control is important both to tune the rate and the spatial anisotropy of molecular diffusion and the molecular conformation in order to meet the reaction steric and photoexcitation requirements.

Experimental Section

Scanning tunneling microscopy (STM) imaging

All the experiments were performed in ultrahigh-vacuum conditions at a base pressure of 2×10^{-10} mbar with an Omicron Scanning Tunneling Microscope (VT-STM). The STM measurements were carried out at room temperature (RT, ≈ 298 K) and near the liquid nitrogen (LN) temperature (≈ 100 K) in constant-current mode by using an electrochemically etched Pt–Ir tip. All STM images were acquired at RT except for those otherwise specified. The sample bias voltage (V_{bias}) is indicated for all STM images and length measurements are calibrated against the Ag lattice parameter along the [001] direction, which was set equal to 4.09 Å. The error bars associated with length determinations represent one standard deviation, as determined from repeated measurements. The STM data were processed with the WSxM software.^[84] Moderate filtering was applied for noise reduction.

Sample preparation

The Ag(110) crystal was cleaned by repeated cycles of 1 keV Ar⁺ sputtering and annealing at 820 K until a clean surface with sufficiently large terraces was confirmed by STM imaging. *trans*-TPP(NH₂)₂ molecules were deposited from a PBN crucible held at ≈ 550 K with an estimated flux of ≈ 0.02 MLmin⁻¹ (1.47×10^{10} cm⁻² s⁻¹). The molecular source was outgassed until the pressure did not increase during the sublimation. One ML is defined as a fully covering single molecular layer of *trans*-TPP(NH₂)₂ arranged in the (5 ± 2, ± 2 ± 3) superstructure. The continuous-wave laser source at 405 nm (Roithner Laser Technik, GmbH; model X40LM-10, Vienna, Austria) provided a surface power density of 75 mWcm⁻² and the beam impinged on the sample with an angle of 70° with respect to the surface normal.

X-ray photoelectron spectroscopy (XPS)

XPS measurements were performed at the ALOISA beamline^[85] at the ELETTRA synchrotron radiation facility (Trieste, Italy), using linearly polarized radiation. The spectra were obtained in normal emission geometry with photon energy of 520 eV and overall XPS resolution of ~ 0.3 eV, by using grazing incident radiation and a home-built hemispherical electron analyzer equipped with a multichannel plate (MCP) detector.

Near-edge X-ray absorption fine structure (NEXAFS)

NEXAFS spectra were measured at the ALOISA beam-line in partial electron yield with a channeltron and a negatively biased (–230 V) grid in front of it to reject low-energy secondary electrons. The orientation of the surface with respect to the linearly polarized photon beam was changed by rotating the surface around the beam axis at a constant grazing incidence angle of $\sim 6^\circ$.^[86] The polarization is defined by the orientation of the scattering plane with respect to either the electric or the magnetic field. Transverse electric (TE) polarization corresponds to *s*-polarization, whereas transverse magnetic (TM) closely corresponds to *p*-polarization (apart

from the grazing angle). The spectra have been energy-calibrated a posteriori by the characteristic absorption signal of the carbon K-edge in the I_0 signal (drain current on the last mirror).

Density functional (DF) calculations

Density functional calculations were performed within the plane-wave pseudopotential formalism using the Quantum ESPRESSO code.^[67] The PBE^[68] approximation to the exchange-correlation functional was adopted, while van der Waals interactions were taken into account by means of the DFT-D2 semi-empirical correction scheme.^[69,90] Ultrasoft pseudopotentials^[91,92] from the QE database were employed, and the cut-offs on plane waves were set to 25 Ry and 250 Ry on the wave function and the charge density, respectively. Geometries were optimized until energy and forces converged within $1\text{E}-4$ Ry and $1\text{E}-5$ Ry/ a_0 , respectively. Reported results refer to an unsupported model of the molecular overlayer: a single layer of TPP molecules not supported by the metal surface placed in a proper cell having the periodicity of the real system. As there is no conducting substrate in our model, STM images cannot be simulated by the conventional Tersoff–Hamann^[93] approach. Rather, in the same spirit of the aforementioned approach, we define the STM current at the position r simply as the integrated local density of states (ILDOS) at that point. Here, local density of states (LDOS) are integrated from the Fermi level E_f to the bias energy ($E_f + eV_b$):

$$I(r, eV_b) = \text{ILDOS}(r, E_f : E_f + eV_b) = \sum_{E_f < E_i < E_f + eV_b}^n \varphi_i(r)^2 \quad (1)$$

where V_b is the applied bias voltage, and the Fermi level is defined as the center of the HOMO–LUMO gap. Within this approach, the numerical value of the current does not have physical meaning, and isocurrent profiles can be qualitatively compared to STM images. To better match the appearance of the porphyrin core, the integration integral of ILDOS was extended up to $+1.5$ eV (-1.5 eV) to simulate STM images acquired at $V_b = 1$ V ($V_b = -1$ V). This choice doesn't affect the features related to the link between monomers, as orbitals localized in that space region are close to the Fermi level. Besides, this roughly takes into account the broadening of molecular states due to the interaction with the surface.

Acknowledgements

P. Villoresi is gratefully acknowledged for providing the laser source. This work has been partially funded by MIUR (PRIN 2010/11, Project No. 2010BNZ3F2: "DESCARTES") and by the University of Padova (Progetto Strategico STPD08RCX5 "HELIOS" and Progetti di Ricerca di Ateneo, CPDA118475/11). The authors acknowledge Cecilia Crestale for the cover illustration.

Keywords: covalent organic frameworks • on-surface synthesis • porphyrins • scanning tunneling microscopy (STM) • surface photochemistry • surface polymerization

- [1] S.-Y. Ding, W. Wang, *Chem. Soc. Rev.* **2013**, *42*, 548–568.
[2] J. Sakamoto, J. van Heijst, O. Lukin, D. Schlüter, *Angew. Chem.* **2009**, *121*, 1048–1089; *Angew. Chem. Int. Ed.* **2009**, *48*, 1030–1069.
[3] D. Bonifazi, S. Mohnani, A. Llanes-Pallas, *Chem. Eur. J.* **2009**, *15*, 7004–7025.

- [4] L. Zang, Y. Che, J. Moore, *Acc. Chem. Res.* **2008**, *41*, 1596–1608.
[5] D. Heim, D. Eciya, K. Seufert, W. Auwärter, C. Aurisicchio, C. Fabbro, D. Bonifazi, J. V. Barth, *J. Am. Chem. Soc.* **2010**, *132*, 6783–6790.
[6] Y. Yang, C. Wang, *Chem. Soc. Rev.* **2009**, *38*, 2576–2589.
[7] T. Kudernac, S. Lei, J. W. Elemans, S. De Feyter, *Chem. Soc. Rev.* **2009**, *38*, 402–421.
[8] M. Di Marino, F. Sedona, M. Sambì, T. Carofiglio, E. Lubian, M. Casarin, E. Tondello, *Langmuir* **2010**, *26*, 2466–2472.
[9] F. Sedona, M. Di Marino, A. Basagni, L. Colazzo, M. Sambì, *J. Phys. Chem. C* **2014**, *118*, 1587–1593.
[10] A. Dmitriev, H. Spillmann, N. Lin, J. V. Barth, K. Kern, *Angew. Chem.* **2003**, *115*, 2774–2777; *Angew. Chem. Int. Ed.* **2003**, *42*, 2670–2673.
[11] A. Langner, S. L. Tait, N. Lin, C. Rajadurai, M. Ruben, K. Kern, *Proc. Natl. Acad. Sci. USA* **2007**, *104*, 17927–17930.
[12] S. Stepanow, N. Lin, J. V. Barth, K. Kern, *J. Phys. Chem. B* **2006**, *110*, 23472–23477.
[13] R. Otero, M. Schöck, L. M. Molina, E. Laegsgaard, I. Stensgaard, B. Hammer, F. Besenbacher, *Angew. Chem.* **2005**, *117*, 2310–2315; *Angew. Chem. Int. Ed.* **2005**, *44*, 2270–2275.
[14] J. Theobald, N. S. Oxtoby, M. Phillips, N. R. Champness, P. H. Beton, *Nature* **2003**, *424*, 1029–1031.
[15] M. Stöhr, M. Wahl, C. H. Galka, T. Riehm, T. a. Jung, L. H. Gade, *Angew. Chem.* **2005**, *117*, 7560–7564; *Angew. Chem. Int. Ed.* **2005**, *44*, 7394–7398.
[16] A. El-Sayed, P. Borghetti, E. Goiri, C. Rogero, L. Floreano, G. Lovat, D. J. Mowbray, J. L. Cabellos, Y. Wakayama, A. Rubio, *ACS Nano* **2013**, *7*, 6914–6920.
[17] D. G. de Oteyza, J. M. García-Lastra, M. Corso, B. P. Doyle, L. Floreano, A. Morgante, Y. Wakayama, A. Rubio, J. E. Ortega, *Adv. Funct. Mater.* **2009**, *19*, 3567–3573.
[18] K. W. Hipps, L. Scudiero, D. E. Barlow, M. P. Cooke, *J. Am. Chem. Soc.* **2002**, *124*, 2126–2127.
[19] S. Furukawa, K. Tahara, F. C. De Schryver, M. Van der Auweraer, Y. Tobe, S. De Feyter, *Angew. Chem.* **2007**, *119*, 2889–2892; *Angew. Chem. Int. Ed.* **2007**, *46*, 2831–2834.
[20] F. Tao, S. L. Bermasek, *J. Am. Chem. Soc.* **2005**, *127*, 12750–12751.
[21] J. Méndez, M. F. López, J. Martín-Gago, *Chem. Soc. Rev.* **2011**, *40*, 4578–4590.
[22] G. Franc, A. Gourdon, *Phys. Chem. Chem. Phys.* **2011**, *13*, 14283–14292.
[23] F. Sedona, M. Di Marino, M. Sambì, T. Carofiglio, E. Lubian, M. Casarin, E. Tondello, *ACS Nano* **2010**, *4*, 5147–5154.
[24] M. Treier, N. V. Richardson, R. Fasel, *J. Am. Chem. Soc.* **2008**, *130*, 14054–14055.
[25] S. Weigelt, C. Busse, C. Bombis, M. M. Knudsen, K. V. Gothelf, T. Strunskus, C. Wöll, M. Dahlbom, B. Hammer, E. Laegsgaard, *Angew. Chem.* **2007**, *119*, 9387–9390; *Angew. Chem. Int. Ed.* **2007**, *46*, 9227–9230.
[26] C. H. Schmitz, J. Ikononov, M. Sokolowski, *J. Phys. Chem. C* **2009**, *113*, 11984–11987.
[27] A. C. Marele, R. Mas-Ballesté, L. Terracciano, J. Rodríguez-Fernández, I. Berlanga, S. S. Alexandre, R. Otero, J. M. Gallego, F. Zamora, J. M. Gómez-Rodríguez, *Chem. Commun.* **2012**, *48*, 6779–6781.
[28] J. Lipton-Duffin, O. Ivasenko, D. F. Perepichka, F. Rosei, *Small* **2009**, *5*, 592–597.
[29] M. Bieri, S. Blankenburg, M. Kivala, C. Pignedoli, P. Ruffieux, K. Müllen, R. Fasel, *Chem. Commun.* **2011**, *47*, 10239–10241.
[30] L. Lafferentz, V. Eberhardt, C. Dri, C. Africh, G. Comelli, F. Esch, S. Hecht, L. Grill, *Nat. Chem.* **2012**, *4*, 215–220.
[31] J. Cai, P. Ruffieux, R. Jaafar, M. Bieri, T. Braun, S. Blankenburg, M. Muoth, A. P. Seitsonen, M. Saleh, X. Feng, *Nature* **2010**, *466*, 470–473.
[32] M. Kittelmann, P. Rahe, M. Nimrlich, C. M. Hauke, A. Gourdon, A. Kühnle, *ACS Nano* **2011**, *5*, 8420–8425.
[33] J. Colson, W. Dichtel, *Nat. Chem.* **2013**, *5*, 453–465.
[34] L. Xu, X. Zhou, Y. Yu, W. Q. Tian, J. Ma, S. Lei, *ACS Nano* **2013**, *7*, 8066–8073.
[35] J. F. Dienstmaier, A. M. Gigler, A. J. Goetz, P. Knochel, T. Bein, A. Lyapin, S. Reichlmaier, W. M. Heckl, M. Lackinger, *ACS Nano* **2011**, *5*, 9737–9745.
[36] C.-Z. Guan, D. Wang, L.-J. Wan, *Chem. Commun.* **2012**, *48*, 2943–2945.
[37] Y.-H. Qiao, Q.-D. Zeng, Z.-Y. Tan, S.-D. Xu, D. Wang, C. Wang, L.-J. Wan, C.-L. Bai, *J. Vac. Sci. Technol. B* **2002**, *20*, 2466.

- [38] X. Zhang, S. Xu, M. Li, Y. Shen, Z. Wei, S. Wang, Q. Zeng, C. Wang, *J. Phys. Chem. C* **2012**, *116*, 8950–8955.
- [39] A. Deshpande, C.-H. Sham, J. M. P. Alaboson, J. M. Mullin, G. C. Schatz, M. C. Hersam, *J. Am. Chem. Soc.* **2012**, *134*, 16759–16764.
- [40] X.-L. Zhou, X.-Y. Zhu, J. M. White, *Surf. Sci. Rep.* **1991**, *13*, 73–220.
- [41] K. Fukutani, M.-B. Song, Y. Murata, *J. Chem. Phys.* **1995**, *103*, 2221.
- [42] S. K. So, R. Franchy, W. Ho, *J. Chem. Phys.* **1991**, *95*, 1385.
- [43] X. L. Zhou, X. Y. Zhu, J. M. White, *Acc. Chem. Res.* **1990**, *23*, 327–332.
- [44] X.-Y. Zhu, J. M. White, *J. Chem. Phys.* **1991**, *94*, 1555.
- [45] J. L. Solomon, R. J. Madix, J. Stöhr, *Surf. Sci.* **1991**, *255*, 12–30.
- [46] V. Poterya, L. Šišťík, P. Slaviček, M. Fárnik, *Phys. Chem. Chem. Phys.* **2012**, *14*, 8936–8944.
- [47] G. King, T. Oliver, M. N. R. Ashfold, *J. Chem. Phys.* **2010**, *132*, 214307.
- [48] J. Lee, S. Ryu, J. S. Ku, S. K. Kim, *J. Chem. Phys.* **2001**, *115*, 10518.
- [49] J. Lee, S. Ryu, J. Chang, S. Kim, S. K. Kim, *J. Phys. Chem. B* **2005**, *109*, 14481–14485.
- [50] J. Brede, M. Linares, S. Kuck, J. Schwöbel, A. Scarfato, S.-H. Chang, G. Hoffmann, R. Wiesendanger, R. Lensen, P. H. J. Kouwer, *Nanotechnology* **2009**, *20*, 275602.
- [51] F. Buchner, I. Kellner, W. Hieringer, *Phys. Chem. Chem. Phys.* **2010**, *12*, 13082–13090.
- [52] M. O. Sinnokrot, C. D. Sherrill, *J. Phys. Chem. A* **2006**, *110*, 10656–10668.
- [53] E. Arunan, H. S. Gutowsky, *J. Chem. Phys.* **1993**, *98*, 4294.
- [54] V. Barone, M. Casarin, D. Forrer, S. Monti, G. Prampolini, *J. Phys. Chem. C* **2011**, *115*, 18434–18444.
- [55] G. Di Santo, S. Blankenburg, C. Castellarin-Cudia, M. Fanetti, P. Borghetti, L. Sangaletti, L. Floreano, A. Verdini, E. Magnano, F. Bondino, *Chem. Eur. J.* **2011**, *17*, 14354–14359.
- [56] T. Yokoyama, S. Yokoyama, T. Kamikado, S. Mashiko, *J. Chem. Phys.* **2001**, *115*, 3814.
- [57] F. Buchner, K.-G. Warnick, T. Wölflle, A. Görling, H.-P. Steinrück, W. Hieringer, H. Marbach, *J. Phys. Chem. C* **2009**, *113*, 16450–16457.
- [58] G. Di Santo, C. Sfiligoi, C. Castellarin-Cudia, A. Verdini, A. Cossaro, A. Morgante, L. Floreano, A. Goldoni, *Chem. Eur. J.* **2012**, *18*, 12619–12623.
- [59] Scalar relativistic two component zeroth-order regular approximation time-dependent-DFT (ZORA TD-DFT) calculations pertaining to H₂-TPP state that, despite the major contribution to the peak at 285.2 eV comes from Cth-based 1s→π* transitions, the participation of 1s→π* excitations involving all the macrocycle C atoms (Cth and C^m) is not negligible (M. V. Nardi, R. Verucchi, L. Pasquali, A. Giglia, G. Fronzoni, M. Sambì, G. Mangione, M. Casarin, submitted).
- [60] Y. Lee, C. Chang, S. Yau, L. Fan, Y. Yang, L. O. Yang, K. Itaya, *J. Am. Chem. Soc.* **2009**, *131*, 6468–6474.
- [61] M. Casarin, M. Di Marino, D. Forrer, M. Sambì, F. Sedona, E. Tondello, A. Vittadini, V. Barone, M. Pavone, *J. Phys. Chem. C* **2010**, *114*, 2144–2153.
- [62] G. Witte, S. Lukas, P. S. Bagus, C. Wöll, *Appl. Phys. Lett.* **2005**, *87*, 263502.
- [63] G. Di Santo, C. Castellarin-Cudia, M. Fanetti, B. Taleatu, P. Borghetti, L. Sangaletti, L. Floreano, E. Magnano, F. Bondino, A. Goldoni, *J. Phys. Chem. C* **2011**, *115*, 4155–4162.
- [64] B. Dong, Y. Fang, L. Xia, H. Xu, M. Sun, *J. Raman Spectrosc.* **2011**, *42*, 1205–1206.
- [65] Y.-F. Huang, H.-P. Zhu, G.-K. Liu, D.-Y. Wu, B. Ren, Z.-Q. Tian, *J. Am. Chem. Soc.* **2010**, *132*, 9244–9246.
- [66] Y. Fang, Y. Li, H. Xu, M. Sun, *Langmuir* **2010**, *26*, 7737–7746.
- [67] L.-B. Zhao, Y.-F. Huang, X.-M. Liu, J. R. Anema, D.-Y. Wu, B. Ren, Z.-Q. Tian, *Phys. Chem. Chem. Phys.* **2012**, *14*, 12919–12929.
- [68] D. Wu, X. Liu, Y. Huang, B. Ren, X. Xu, Z. Tian, *J. Phys. Chem. C* **2009**, *113*, 18212–18222.
- [69] M. Onoue, M. R. Han, E. Ito, M. Hara, *Surf. Sci.* **2006**, *600*, 3999–4003.
- [70] U. Jung, S. Kuhn, U. Cornelissen, F. Tuzcek, T. Strunskus, V. Zaporotchenko, J. Kubitschke, R. Herges, O. Magnussen, *Langmuir* **2011**, *27*, 5899–5908.
- [71] D. Brete, D. Przyrembel, C. Eickhoff, R. Carley, W. Freyer, K. Reuter, C. Gahl, M. Weinelt, *J. Phys. Condens. Matter* **2012**, *24*, 394015.
- [72] G. Mercurio, E. R. McNellis, I. Martin, S. Hagen, F. Leyssner, S. Soubatch, J. Meyer, M. Wolf, P. Tegeder, F. S. Tautz, *Phys. Rev. Lett.* **2010**, *104*, 036102.
- [73] D. Menzel, *Crit. Rev. Solid State Mater. Sci.* **1978**, *7*, 357–384.
- [74] T. Nakayama, K. Inamura, Y. Inoue, S. Ikeda, K. Kishi, *Surf. Sci.* **1987**, *179*, 47–58.
- [75] M. Piantek, J. Miguel, M. Bernien, C. Navío, A. Krüger, B. Priewisch, K. Rück-Braun, W. Kuch, *Appl. Phys. A* **2008**, *93*, 261–266.
- [76] M. Piantek, J. Miguel, A. Krüger, C. Navío, M. Bernien, D. K. Ball, K. Hermann, W. Kuch, *J. Phys. Chem. C* **2009**, *113*, 20307–20315.
- [77] M. Miyachi, Y. Yamamoto, Y. Yamanoi, A. Minoda, S. Oshima, Y. Kobori, H. Nishihara, *Langmuir* **2013**, *29*, 5099–5103.
- [78] A. Mesnager, X. Lefèvre, P. Jégou, G. Deniau, S. Palacin, *Langmuir* **2012**, *28*, 11767–11778.
- [79] J. W. Gadzuk, *J. Chem. Phys.* **2012**, *137*, 091703.
- [80] S. R. Hatch, X.-Y. Zhu, J. M. White, A. Campion, *J. Chem. Phys.* **1990**, *92*, 2681.
- [81] F. Montalenti, R. Ferrando, *Phys. Rev. B* **1999**, *59*, 5881–5891.
- [82] U. T. Ndongmouo, F. Hontinfinde, *Surf. Sci.* **2004**, *571*, 89–101.
- [83] M. Comstock, N. Levy, A. Kirakosian, J. Cho, F. Lauterwasser, J. Harvey, D. Strubbe, J. Fréchet, D. Trauner, S. Louie, *Phys. Rev. Lett.* **2007**, *99*, 038301.
- [84] I. Horcas, R. Fernández, J. M. Gómez-Rodríguez, J. Colchero, J. Gómez-Herrero, A. M. Baro, *Rev. Sci. Instrum.* **2007**, *78*, 013705.
- [85] L. Floreano, G. Naletto, D. Cvetko, R. Gotter, M. Malvezzi, L. Marassi, A. Morgante, A. Santaniello, A. Verdini, F. Tommasini, *Rev. Sci. Instrum.* **1999**, *70*, 3855.
- [86] L. Floreano, A. Cossaro, R. Gotter, A. Verdini, G. Bavdek, F. Evangelista, A. Ruocco, A. Morgante, D. Cvetko, *J. Phys. Chem. C* **2008**, *112*, 10794–10802.
- [87] P. Giannozzi, S. Baroni, N. Bonini, M. Calandra, R. Car, C. Cavazzoni, D. Ceresoli, G. L. Chiarotti, M. Cococcioni, I. Dabo, *J. Phys. Condens. Matter* **2009**, *21*, 395502.
- [88] J. P. Perdew, K. Burke, M. Ernzerhof, *Phys. Rev. Lett.* **1996**, *77*, 3865–3868.
- [89] S. Grimme, *J. Comput. Chem.* **2006**, *27*, 1787–1799.
- [90] V. Barone, M. Casarin, D. Forrer, M. Pavone, M. Sambì, A. Vittadini, *J. Comput. Chem.* **2009**, *30*, 934–939.
- [91] A. Rappe, K. Rabe, E. Kaxiras, J. Joannopoulos, *Phys. Rev. B* **1990**, *41*, 1227–1230.
- [92] D. Vanderbilt, *Phys. Rev. B* **1990**, *41*, 7892–7895.
- [93] J. Tersoff, D. R. Hamann, *Phys. Rev. Lett.* **1983**, *50*, 1998–2001.

Received: April 23, 2014

Published online on September 8, 2014

Summary and outlook

In this thesis the synthesis of surface supported organic nanostructures has been studied under ultra-high vacuum conditions. The molecular assemblies and each reaction step were characterized by means of scanning tunneling microscopy, X-ray photoelectron spectroscopy, low-energy electron diffraction and, when it was possible, by synchrotron radiation-based techniques. The combination of local, real- and reciprocal-space probe techniques and surface-averaging spectroscopy provided complementary information about the molecular structures and the chemical states. The identification of bond types and binding configurations are supported by density functional theory calculations of geometry-optimized building blocks.

The main part of the thesis focuses on the synthesis of low-dimensional covalent nanostructures by means of on-surface polymerization. To this end, different coupling reactions, substrate materials and reaction parameters were investigated.

Firstly, advanced growth modes have been employed to synthesize specific molecular objects such as graphene nanoribbons and doped poly-paraphenylene 1D wires. We adopted a finely tuned hierarchical approach to perform a stepwise on-surface polymerization reaction leading to oriented GNRs as the final product. According to a carefully designed retrosynthetic analysis, 4,4''-dibromo-p-terphenyl has been recognized as the possible starting precursor. In fact, after an initial Ullmann coupling step between the monomers in order to get ordered and extended poly(p-phenylene)wires, the N=6 armchair graphene nanoribbons are obtained by a controlled activation of the C-H bond. As outlined in table 1 (page 20), the good separation of the reaction steps is a consequence of the rather high bond enthalpy difference between the C-Br and the C-H functional groups. The synthesis was performed on Au(111), which is well-suited for the on-surface covalent coupling, since on it the organometallic network found on other coinage metals is not formed and therefore no higher temperature treatments are required to complete the Ullmann reaction. The protocol developed in this thesis reveals an important characteristic that the on-surface reactions should have in order to obtain large domains of long-range ordered materials using non-reversible covalent coupling: the precursors have to be able to rearrange from the starting supramolecular motif to the final covalent nanostructure with small local positional/orientational adjustments. In this way, long-range diffusion is avoided and hence defects formation is less

probable. Finally, the spectroscopic characterization of the synthesis allowed us to shed new light on the behaviour of the C 1s peak during the Ullmann-like coupling on Au(111). In fact, the shift toward lower BE of this core level seems to be related to the evolution of the surface reconstruction as a function of temperature and reaction extent rather than to the chemisorption of bromine atoms, as previously claimed. Performing the reaction protocol on a (887) vicinal surface allowed us to characterize the electronic π -band structure of the bottom-up synthesized poly-p-phenylene (PPP) polymer. Insight about the electronic properties have been obtained by angle resolved photoemission spectroscopy (ARPES) and NEXAFS. The ARPES data acquired parallel to the main axis of the molecules reveal the formation of a highly dispersive valence band with maximum (VBM) at $E_F - 1.04$ eV, $k_{\parallel} = 1.49 \text{ \AA}^{-1}$ once the polymer is obtained, in agreement with the PPP lattice periodicity. Constant energy maps at VBM reveal that its intensity is spread almost uniformly in k_{\perp} (perpendicular to the wires) with negligible energy dispersion. Such flat bands imply that these orbitals are localized within the molecules due to a rather small intermolecular overlap, hence our results highlight the occurrence of truly mono-dimensional dispersion.

The same reaction protocol has been used to investigate the effect of nitrogen incorporation into the conjugated PPP chain. For this purpose two pyridinic derivatives of 4,4"-p-dibromo-terphenyl have been specifically synthesized. The electronic structure revealed by ARPES for the nitrogen-containing polymers shares the main characteristic of pristine PPP; however, a shift of the entire band structure towards lower binding energy has been observed. Interestingly, the magnitude of such shift is directly proportional to the nitrogen content, while the HOMO-LUMO gap remains unaltered.

Part of this work was devoted to the study and to the optimization of the experimental conditions that could lead to low temperature Ullmann coupling. Mild reaction conditions are particularly important when dealing with organic molecules because they could desorb or undergo decomposition as result of a thermal treatment. We adopted a sterically hindered precursor with respect to the second step of the reaction, i.e. the C-C coupling, because it allowed us to reveal fingerprint signals of the occurred C-Br photodissociation process. In addition to the effectiveness of the protocol, the results show that low temperatures coupled with laser irradiation significantly improve the molecular ordering to a level that is not reachable by

annealing only. Sideways to the feasibility of photochemical activation, DFT modelling has highlighted how chemisorbed bromine are by no means independent species, since they contribute significantly to stabilize the organometallic structure.

During the research activity, apart from the Ullmann based reactions, other photochemical reactions have been tested. In particular, aniline-functionalized porphyrins have been shown to undergo covalent coupling leading to aza-connected meso-tetraphenyl porphyrin wires. This work points out that not only the mobility, but also the molecular density of the self-organized structure affects the reactivity of a chemical species.

In perspective of future works, the reported bottom-up synthesis of graphene nanoribbons seems to be quite promising for the growth and characterization of the full $N=3n$ class of nanoribbons. In fact, although it is possible to partially control the synthesis of $N=6$ by annealing at the minimum temperature able to activate the C-H bonds, higher temperature treatments lead to the merging of more than two poly-paraphenylene chains. Even if a wide size distribution is observed, atomic sensitive techniques (STS) can be applied to gather information about the electronic structure of each single width-selected nanoribbon, such as band gap size and energy level alignment with respect to the Fermi level. Fine control of the dimensional dispersion of the ribbons may be obtained by adopting surface templating, as successfully applied to the characterization of the electronic structure of doped-polyparaphenylene chains. By confining the rodlike molecules onto a reduced-width terrace of a vicinal surface, it should be possible to tune the number of laterally connected PPP strands, thus allowing the use of surface averaging characterization techniques.

The application of photochemical reactions to on-surface synthesis is definitely the area with the greatest possibilities of development. In fact, the reported work shows that it is possible to find appropriate conditions to activate specific functional groups. Actually, considering the reduced number of publications in this field, a screening of the applicable reactions has still to be carried out. Particular attention should be directed towards homolytic photodissociations because they are the only ones that in principle can compete with the very short quenching times of molecular excitations and because they can be activated by an indirect mechanism.

- [1] K. C. Nicolaou, C. R. H. Hale, C. Nilewski, H. A. Ioannidou, *Chem. Soc. Rev.* **2012**, *41*, 5185.
- [2] K. C. Nicolaou, J. S. Chen, *Chem. Soc. Rev.* **2009**, *38*, 2993.
- [3] C. Grondal, M. Jeanty, D. Enders, *Nat. Chem.* **2010**, *2*, 167–178.
- [4] C. M. Thomas, *Chem. Soc. Rev.* **2010**, *39*, 165–173.
- [5] P. Anastas, N. Eghbali, *Chem. Soc. Rev.* **2010**, *39*, 301–312.
- [6] D. J. Newman, G. M. Cragg, *J. Nat. Prod.* **2007**, *70*, 461–477.
- [7] C. W. Bielawski, R. H. Grubbs, *Prog. Polym. Sci.* **2007**, *32*, 1–29.
- [8] K. Matyjaszewski, N. V. Tsarevsky, *Nat. Chem.* **2009**, *1*, 276–288.
- [9] M. Semsarilar, S. Perrier, *Nat. Chem.* **2010**, *2*, 811–820.
- [10] J. Sakamoto, J. van Heijst, O. Lukin, a D. Schlüter, *Angew. Chem. Int. Ed. Engl.* **2009**, *48*, 1030–69.
- [11] P. Wei, X. Yan, F. Huang, *Chem. Soc. Rev.* **2015**, *44*, 815–832.
- [12] K. Thorkelsson, P. Bai, T. Xu, *Nano Today* **2015**, *10*, 48–66.
- [13] Y. Zhao, F. Sakai, L. Su, Y. Liu, K. Wei, G. Chen, M. Jiang, *Adv. Mater.* **2013**, *25*, 5215–5256.
- [14] P. Murugan, M. Krishnamurthy, S. N. Jaisankar, D. Samanta, A. B. Mandal, *Chem. Soc. Rev.* **2015**, *44*, 3212–3243.
- [15] L.-S. Zhong, J.-S. Hu, H.-P. Liang, A.-M. Cao, W.-G. Song, L.-J. Wan, *Adv. Mater.* **2006**, *18*, 2426–2431.
- [16] Y. Yang, Y. Zheng, W. Cao, A. Titov, J. Hyvonen, J. R. Manders, J. Xue, P. H. Holloway, L. Qian, *Nat. Photonics* **2015**, DOI 10.1038/nphoton.2015.36.
- [17] S.-Y. Min, T.-S. Kim, Y. Lee, H. Cho, W. Xu, T.-W. Lee, *Small* **2015**, *11*, 45–62.
- [18] Z. Liu, J. Xu, D. Chen, G. Shen, *Chem. Soc. Rev.* **2015**, *44*, 161–192.
- [19] L. Dou, A. B. Wong, Y. Yu, M. Lai, N. Kornienko, S. W. Eaton, A. Fu, C. G. Bischak, J. Ma, T. Ding, et al., *Science (80-.)*. **2015**, *349*, 1518–1521.

- [20] Y. Shi, H. Li, L.-J. Li, *Chem. Soc. Rev.* **2015**, *44*, 2744–2756.
- [21] a K. Geim, K. S. Novoselov, *Nat. Mater.* **2007**, *6*, 183–91.
- [22] L. D. Landau, *Phys. Z. Sowjetunion* **1937**, *11*, 26–35.
- [23] R. Peierls, *Ann. l'institut Henri Poincaré* **1935**, *5*, 177–222.
- [24] E. M. Landau, L. D. and Lifshitz, *Statistical Physics, Part I*, Oxford, **1980**.
- [25] N. D. Mermin, *Phys. Rev.* **1968**, *176*, 250–254.
- [26] J. A. Venables, G. D. T. Spiller, M. Hanbucken, *Reports Prog. Phys.* **1984**, *47*, 399–459.
- [27] J. W. Evans, P. A. Thiel, M. C. Bartelt, *Surf. Sci. Rep.* **2006**, *61*, 1–128.
- [28] K. S. Novoselov, D. Jiang, F. Schedin, T. J. Booth, V. V. Khotkevich, S. V. Morozov, A. K. Geim, *Proc. Natl. Acad. Sci.* **2005**, *102*, 10451–10453.
- [29] K. S. Novoselov, *Science (80-.)*. **2004**, *306*, 666–669.
- [30] J. C. Meyer, A. K. Geim, M. I. Katsnelson, K. S. Novoselov, T. J. Booth, S. Roth, *Nature* **2007**, *446*, 60–63.
- [31] P. Blake, P. D. Brimicombe, R. R. Nair, T. J. Booth, D. Jiang, F. Schedin, L. A. Ponomarenko, S. V. Morozov, H. F. Gleeson, E. W. Hill, et al., *Nano Lett.* **2008**, *8*, 1704–1708.
- [32] S. K. Min, W. Y. Kim, Y. Cho, K. S. Kim, *Nat. Nanotechnol.* **2011**, *6*, 162–165.
- [33] M. Liu, X. Yin, E. Ulin-Avila, B. Geng, T. Zentgraf, L. Ju, F. Wang, X. Zhang, *Nature* **2011**, *474*, 64–67.
- [34] D. Chen, L. Tang, J. Li, *Chem. Soc. Rev.* **2010**, *39*, 3157.
- [35] M. I. Katsnelson, K. S. Novoselov, *Solid State Commun.* **2007**, *143*, 3–13.
- [36] F. Diederich, M. Kivala, *Adv. Mater.* **2010**, *22*, 803–812.
- [37] N. Narita, S. Nagai, S. Suzuki, K. Nakao, *Phys. Rev. B* **1998**, *58*, 11009–11014.
- [38] A. T. Balaban, *Comput. Math. with Appl.* **1989**, *17*, 397–416.
- [39] C. D. Simpson, J. D. Brand, A. J. Berresheim, L. Przybilla, H. J. Räder, K. Müllen, *Chem. - A Eur. J.* **2002**, *8*, 1424–1429.

- [40] J. A. Marsden, M. M. Haley, *J. Org. Chem.* **2005**, *70*, 10213–10226.
- [41] X. Zhuang, Y. Mai, D. Wu, F. Zhang, X. Feng, *Adv. Mater.* **2015**, *27*, 403–427.
- [42] I. Levesque, J. R. Néabo, S. Rondeau-Gagné, C. Vigier-Carrière, M. Daigle, J.-F. Morin, *Chem. Sci.* **2014**, *5*, 831–836.
- [43] K. Baek, G. Yun, Y. Kim, D. Kim, R. Hota, I. Hwang, D. Xu, Y. H. Ko, G. H. Gu, J. H. Suh, et al., *J. Am. Chem. Soc.* **2013**, *135*, 6523–6528.
- [44] J. Wu, L. Gherghel, M. D. Watson, J. Li, Z. Wang, C. D. Simpson, U. Kolb, K. Müllen, *Macromolecules* **2003**, *36*, 7082–7089.
- [45] C. S. Hartley, E. L. Elliott, J. S. Moore, *J. Am. Chem. Soc.* **2007**, *129*, 4512–4513.
- [46] T. E. O. Screen, J. R. G. Thorne, R. G. Denning, D. G. Bucknall, H. L. Anderson, *J. Am. Chem. Soc.* **2002**, *124*, 9712–9713.
- [47] J. F. Dienstmaier, D. D. Medina, M. Dogru, P. Knochel, T. Bein, W. M. Heckl, M. Lackinger, *ACS Nano* **2012**, *6*, 7234–42.
- [48] S.-Y. Ding, W. Wang, *Chem. Soc. Rev.* **2013**, *42*, 548–68.
- [49] A. P. Cote, *Science (80-.)*. **2005**, *310*, 1166–1170.
- [50] X. Feng, X. Ding, D. Jiang, *Chem. Soc. Rev.* **2012**, *41*, 6010.
- [51] H. Furukawa, O. M. Yaghi, *J. Am. Chem. Soc.* **2009**, *131*, 8875–83.
- [52] Q. Fang, J. Wang, S. Gu, R. B. Kaspar, Z. Zhuang, J. Zheng, H. Guo, S. Qiu, Y. Yan, *J. Am. Chem. Soc.* **2015**, *137*, 8352–8355.
- [53] J. Colson, W. Dichtel, *Nat. Chem.* **2013**, *5*, 453–465.
- [54] A. Dubault, C. Casagrande, M. Veyssie, *J. Phys. Chem.* **1975**, *79*, 2254–2259.
- [55] C. Rosilio, A. Ruaudel-Teixier, *J. Polym. Sci. Polym. Chem. Ed.* **1975**, *13*, 2459–2471.
- [56] R. Xie, Y. Song, L. Wan, H. Yuan, P. Li, X. Xiao, L. Liu, S. Ye, S. Lei, L. Wang, *Anal. Sci.* **2011**, *27*, 129–38.
- [57] G. Franc, A. Gourdon, *Phys. Chem. Chem. Phys.* **2011**, *13*, 14283–92.
- [58] J. Méndez, M. F. López, J. a Martín-Gago, *Chem. Soc. Rev.* **2011**, *40*, 4578–90.

- [59] K. Morigaki, T. Baumgart, U. Jonas, W. Knoll, **2002**, 5128–5135.
- [60] W. Eck, A. Küller, M. Grunze, B. Völkel, A. Götzhäuser, *Adv. Mater.* **2005**, *17*, 2583–2587.
- [61] G. Sui, M. Micic, Q. Huo, R. M. Leblanc, *Colloids Surfaces A Physicochem. Eng. Asp.* **2000**, *171*, 185–197.
- [62] S. Bresler, M. Judin, Talmud D., *Acta Physicochim. URSS* **1941**, *XIV*, 71–84.
- [63] G. Wegner, *Thin Solid Films* **1992**, *216*, 105–116.
- [64] G. Weidemann, G. Brezesinski, D. Vollhardt, C. DeWolf, H. Möhwald, *Langmuir* **1999**, *15*, 2901–2910.
- [65] G. Brezesinski, E. Scalas, B. Struth, H. Moehwald, F. Bringezu, U. Gehlert, G. Weidemann, D. Vollhardt, *J. Phys. Chem.* **1995**, *99*, 8758–8762.
- [66] R. Gutzler, D. F. Perepichka, *J. Am. Chem. Soc.* **2013**, *135*, 16585–16594.
- [67] J.-J. Adjizian, P. Briddon, B. Humbert, J.-L. Duvail, P. Wagner, C. Adda, C. Ewels, *Nat. Commun.* **2014**, *5*, 5842.
- [68] G. M. Whitesides, *Science (80-.)*. **2002**, *295*, 2418–2421.
- [69] Y. Yang, C. Wang, *Chem. Soc. Rev.* **2009**, *38*, 2576–89.
- [70] T. Kudernac, S. Lei, J. a a W. Elemans, S. De Feyter, *Chem. Soc. Rev.* **2009**, *38*, 402–21.
- [71] J. V. Barth, G. Costantini, K. Kern, *Nature* **2005**, *437*, 671–679.
- [72] O. Ikkala, G. ten Brinke, *Science* **2002**, *295*, 2407–9.
- [73] F. Sedona, M. Di Marino, M. Sambri, T. Carofiglio, E. Lubian, M. Casarin, E. Tondello, *ACS Nano* **2010**, *4*, 5147–54.
- [74] X. Zhang, S. Xu, M. Li, Y. Shen, Z. Wei, S. Wang, Q. Zeng, C. Wang, *J. Phys. Chem. C* **2012**, *116*, 8950–8955.
- [75] A. Deshpande, C.-H. Sham, J. M. P. Alaboson, J. M. Mullin, G. C. Schatz, M. C. Hersam, *J. Am. Chem. Soc.* **2012**, *134*, 16759–64.
- [76] N. a a Zwaneveld, R. Pawlak, M. Abel, D. Catalin, D. Gigmes, D. Bertin, L. Porte, *J. Am. Chem. Soc.* **2008**, *130*, 6678–9.
- [77] O. Ourdjini, R. Pawlak, M. Abel, S. Clair, L. Chen, N. Bergeon, M. Sassi, V. Oison, J.-M. Debierre, R. Coratger, et al., *Phys. Rev. B* **2011**, *84*, 125421.

- [78] C.-Z. Guan, D. Wang, L.-J. Wan, *Chem. Commun. (Camb)*. **2012**, 48, 2943–5.
- [79] J. F. Dienstmaier, A. M. Gigler, A. J. Goetz, P. Knochel, T. Bein, A. Lyapin, S. Reichlmaier, W. M. Heckl, M. Lackinger, *ACS Nano* **2011**, 5, 9737–45.
- [80] L. Xu, X. Zhou, Y. Yu, W. Q. Tian, J. Ma, S. Lei, *ACS Nano* **2013**, 7, 8066–73.
- [81] S. Weigelt, C. Busse, C. Bombis, M. M. Knudsen, K. V. Gothelf, E. Laegsgaard, F. Besenbacher, T. R. Linderoth, *Angew. Chem. Int. Ed. Engl.* **2008**, 47, 4406–10.
- [82] S. Weigelt, C. Busse, C. Bombis, M. M. Knudsen, K. V. Gothelf, T. Strunskus, C. Wöll, M. Dahlbom, B. Hammer, E. Laegsgaard, et al., *Angew. Chem. Int. Ed. Engl.* **2007**, 46, 9227–30.
- [83] G. Otero, G. Biddau, C. Sánchez-Sánchez, R. Caillard, M. F. López, C. Rogero, F. J. Palomares, N. Cabello, M. A. Basanta, J. Ortega, et al., *Nature* **2008**, 454, 865–868.
- [84] K. Amsharov, N. Abdurakhmanova, S. Stepanow, S. Rauschenbach, M. Jansen, K. Kern, *Angew. Chemie Int. Ed.* **2010**, 49, 9392–9396.
- [85] D. Zhong, J.-H. Franke, S. K. Podiyanachari, T. Blömker, H. Zhang, G. Kehr, G. Erker, H. Fuchs, L. Chi, *Science* **2011**, 334, 213–6.
- [86] M. Koudia, M. Abel, *Chem. Commun. (Camb)*. **2014**, 50, 8565–7.
- [87] A. Wiengarten, K. Seufert, W. Auwärter, D. Ecija, K. Diller, F. Allegretti, F. Bischoff, S. Fischer, D. A. Duncan, A. C. Papageorgiou, et al., *J. Am. Chem. Soc.* **2014**, 136, 9346–54.
- [88] M. Abel, S. Clair, O. Ourdjini, M. Mossoyan, L. Porte, *J. Am. Chem. Soc.* **2011**, 133, 1203–1205.
- [89] L. Lafferentz, F. Ample, H. Yu, S. Hecht, C. Joachim, L. Grill, *Science* **2009**, 323, 1193–1197.
- [90] G. Di Santo, C. Castellarin-Cudia, M. Fanetti, B. Taleatu, P. Borghetti, L. Sangaletti, L. Floreano, E. Magnano, F. Bondino, A. Goldoni, *J. Phys. Chem. C* **2011**, 115, 4155–4162.
- [91] K. Diller, F. Klappenberger, M. Marschall, K. Hermann, A. Nefedov, C. Wöll, J. V Barth, *J. Chem. Phys.* **2012**, 136, 014705.
- [92] A. Goldoni, C. a Pignedoli, G. Di Santo, C. Castellarin-Cudia, E. Magnano, F. Bondino, A. Verdini, D. Passerone, *ACS Nano* **2012**, 6, 10800–7.
- [93] S. De Feyter, J. Hofkens, *Chem. ...* **2001**, 1, 585–592.
- [94] Y. Okawa, M. Aono, *Nature* **2001**, 409, 683–684.

- [95] Q. Fan, C. Wang, L. Liu, Y. Han, J. Zhao, J. Zhu, J. Kuttner, G. Hilt, J. M. Gottfried, *J. Phys. Chem. C* **2014**, *118*, 13018–13025.
- [96] M. O. Blunt, J. C. Russell, N. R. Champness, P. H. Beton, *Chem. Commun. (Camb)*. **2010**, *46*, 7157–9.
- [97] J. Eichhorn, D. Nieckarz, O. Ochs, D. Samanta, M. Schmittel, P. J. Szabelski, M. Lackinger, *ACS Nano* **2014**, *8*, 7880–9.
- [98] A. C. Marele, R. Mas-Ballesté, L. Terracciano, J. Rodríguez-Fernández, I. Berlanga, S. S. Alexandre, R. Otero, J. M. Gallego, F. Zamora, J. M. Gómez-Rodríguez, *Chem. Commun. (Camb)*. **2012**, *48*, 6779–81.
- [99] S. Jensen, H. Früchtl, C. J. Baddeley, *J. Am. Chem. Soc.* **2009**, *131*, 16706–13.
- [100] J. Greenwood, H. A. Fru, C. J. Baddeley, *J. Phys. Chem. C* **2013**, DOI 10.1021/jp3107606.
- [101] M. Treier, N. V Richardson, R. Fasel, *J. Am. Chem. Soc.* **2008**, *130*, 14054–5.
- [102] M. Treier, R. Fasel, N. R. Champness, S. Argent, N. V Richardson, *Phys. Chem. Chem. Phys.* **2009**, *11*, 1209–14.
- [103] C. H. Schmitz, J. Ikononov, M. Sokolowski, **2011**, 7270–7278.
- [104] S. Jensen, J. Greenwood, H. A. Fr, C. J. Baddeley, **2011**, 8630–8636.
- [105] F. Bebensee, C. Bombis, S.-R. Vadapoo, J. R. Cramer, F. Besenbacher, K. V Gothelf, T. R. Linderoth, *J. Am. Chem. Soc.* **2013**, *135*, 2136–9.
- [106] J. Hassan, M. Sévignon, C. Gozzi, E. Schulz, M. Lemaire, *Chem. Rev.* **2002**, *102*, 1359–470.
- [107] R. Lindner, A. Kühnle, *ChemPhysChem* **2015**, n/a–n/a.
- [108] S.-W. Hla, L. Bartels, G. Meyer, K.-H. Rieder, *Phys. Rev. Lett.* **2000**, *85*, 2777–2780.
- [109] L. Grill, M. Dyer, L. Lafferentz, M. Persson, M. V Peters, S. Hecht, *Nat. Nanotechnol.* **2007**, *2*, 687–91.
- [110] R. Gutzler, H. Walch, G. Eder, S. Kloft, W. M. Heckl, M. Lackinger, *Chem. Commun. (Camb)*. **2009**, 4456–8.
- [111] G. S. McCarty, P. S. Weiss, *J. Am. Chem. Soc.* **2004**, *126*, 16772–6.
- [112] A. Saywell, W. Greń, G. Franc, A. Gourdon, X. Bouju, L. Grill, *J. Phys. Chem. C* **2014**, *118*, 1719–1728.

- [113] Q. Fan, C. Wang, Y. Han, J. Zhu, W. Hieringer, J. Kuttner, G. Hilt, J. M. Gottfried, *Angew. Chem. Int. Ed. Engl.* **2013**, *52*, 4668–72.
- [114] M. Chen, J. Xiao, H. P. Steinrück, S. Wang, W. Wang, N. Lin, W. Hieringer, J. M. Gottfried, *J. Phys. Chem. C* **2014**, *118*, 6820–6830.
- [115] M. Di Giovannantonio, M. El Garah, J. Lipton-Duffin, V. Meunier, L. Cardenas, Y. Fagot Revurat, A. Cossaro, A. Verdini, D. F. Perepichka, F. Rosei, et al., *ACS Nano* **2013**, *7*, 8190–8198.
- [116] J. Eichhorn, T. Strunskus, A. Rastgoo-Lahrood, D. Samanta, M. Schmittel, M. Lackinger, *Chem. Commun. (Camb)*. **2014**, *50*, 7680–2.
- [117] A. Batra, D. Cvetko, G. Kladnik, O. Adak, C. Cardoso, A. Ferretti, D. Prezzi, E. Molinari, A. Morgante, L. Venkataraman, *Chem. Sci.* **2014**, *5*, 4419–4423.
- [118] K. A. Simonov, N. A. Vinogradov, A. S. Vinogradov, A. V Generalov, E. M. Zagrebina, N. Mårtensson, A. A. Cafolla, T. Carpy, J. P. Cunniffe, A. B. Preobrajenski, *J. Phys. Chem. C* **2014**, *118*, 12532–12540.
- [119] H. Zhang, H. Lin, K. Sun, L. Chen, Y. Zagranyarski, N. Aghdassi, S. Duhm, Q. Li, D. Zhong, Y. Li, et al., *J. Am. Chem. Soc.* **2015**, *137*, 4022–4025.
- [120] W. J. Jang, K.-H. Chung, M. W. Lee, H. Kim, S. Lee, S.-J. Kahng, *Appl. Surf. Sci.* **2014**, *309*, 74–78.
- [121] T. A. Pham, F. Song, M.-T. Nguyen, M. Stöhr, *Chem. Commun.* **2014**, *50*, 14089–14092.
- [122] J. Park, K. Y. Kim, K. H. Chung, J. K. Yoon, H. Kim, S. Han, S. J. Kahng, *J. Phys. Chem. C* **2011**, *115*, 14834–14838.
- [123] W. Wang, X. Shi, S. Wang, M. a Van Hove, N. Lin, *J. Am. Chem. Soc.* **2011**, *133*, 13264–7.
- [124] M. Bieri, M. Treier, J. Cai, K. Aït-Mansour, P. Ruffieux, O. Gröning, P. Gröning, M. Kastler, R. Rieger, X. Feng, et al., *Chem. Commun. (Camb)*. **2009**, 6919–21.
- [125] M. O. M. Blunt, J. J. C. Russell, N. R. Champness, P. H. Beton, *Chem. Commun. (Camb)*. **2010**, *46*, 7157–9.
- [126] K.-H. Chung, B.-G. Koo, H. Kim, J. K. Yoon, J.-H. Kim, Y.-K. Kwon, S.-J. Kahng, *Phys. Chem. Chem. Phys.* **2012**, *14*, 7304–8.
- [127] M. Bieri, S. Blankenburg, M. Kivala, C. a Pignedoli, P. Ruffieux, K. Müllen, R. Fasel, *Chem. Commun. (Camb)*. **2011**, *47*, 10239–41.
- [128] Q. Fan, C. Wang, Y. Han, J. Zhu, J. Kuttner, G. Hilt, J. M. Gottfried, *ACS Nano* **2014**, *8*, 709–718.

- [129] J. Björk, F. Hanke, S. Stafström, *J. Am. Chem. Soc.* **2013**, *135*, 5768–75.
- [130] M. Bieri, M.-T. Nguyen, O. Gröning, J. Cai, M. Treier, K. Ait-Mansour, P. Ruffieux, C. a Pignedoli, D. Passerone, M. Kastler, et al., *J. Am. Chem. Soc.* **2010**, *132*, 16669–76.
- [131] H. Zhang, J. H. Franke, D. Zhong, Y. Li, A. Timmer, O. D. Arado, H. Mönig, H. Wang, L. Chi, Z. Wang, et al., *Small* **2014**, *10*, 1361–1368.
- [132] F. Klappenberger, Y.-Q. Zhang, J. Björk, S. Klyatskaya, M. Ruben, J. V. Barth, *Acc. Chem. Res.* **2015**, *48*, 2140–2150.
- [133] Y.-Q. Zhang, N. Kepčija, M. Kleinschrodt, K. Diller, S. Fischer, A. C. Papageorgiou, F. Allegretti, J. Björk, S. Klyatskaya, F. Klappenberger, et al., *Nat. Commun.* **2012**, *3*, 1286.
- [134] J. Liu, P. Ruffieux, X. Feng, K. Müllen, R. Fasel, *Chem. Commun. (Camb)*. **2014**, *50*, 11200–11203.
- [135] H. Zhou, J. Liu, S. Du, L. Zhang, G. Li, Y. Zhang, B. Z. Tang, H.-J. Gao, *J. Am. Chem. Soc.* **2014**, *136*, 5567–70.
- [136] H.-Y. Gao, J.-H. Franke, H. Wagner, D. Zhong, P.-A. Held, A. Studer, H. Fuchs, *J. Phys. Chem. C* **2013**, *117*, 18595–18602.
- [137] J. Björk, Y.-Q. Zhang, F. Klappenberger, J. V. Barth, S. Stafström, *J. Phys. Chem. C* **2014**, *118*, 3181–3187.
- [138] H.-Y. Gao, P. A. Held, M. Knor, C. Mück-Lichtenfeld, J. Neugebauer, A. Studer, H. Fuchs, *J. Am. Chem. Soc.* **2014**, *136*, 9658–63.
- [139] S. Vajda, M. J. Pellin, J. P. Greeley, C. L. Marshall, L. A. Curtiss, G. A. Ballentine, J. W. Elam, S. Catillon-Mucherie, P. C. Redfern, F. Mehmood, et al., *Nat. Mater.* **2009**, *8*, 213–216.
- [140] M. C. Tsai, C. M. Friend, E. L. Muetterties, *J. Am. Chem. Soc.* **1982**, *104*, 2539–2543.
- [141] M. Treier, C. A. Pignedoli, T. Laino, R. Rieger, K. Müllen, D. Passerone, R. Fasel, *Nat. Chem.* **2011**, *3*, 61–67.
- [142] J. Cai, P. Ruffieux, R. Jaafar, M. Bieri, T. Braun, S. Blankenburg, M. Muoth, A. P. Seitsonen, M. Saleh, X. Feng, et al., *Nature* **2010**, *466*, 470–3.
- [143] M. In't Veld, P. Iavicoli, S. Haq, D. B. Amabilino, R. Raval, *Chem. Commun. (Camb)*. **2008**, 1536–8.
- [144] M. Matena, T. Riehm, M. Stöhr, T. a Jung, L. H. Gade, *Angew. Chem. Int. Ed. Engl.* **2008**, *47*, 2414–7.
- [145] C. Zhang, Q. Sun, H. Chen, Q. Tan, W. Xu, *Chem. Commun. (Camb)*. **2015**, *51*, 495–8.

- [146] L. Ferrighi, I. Piš, T. H. Nguyen, M. Cattelan, S. Nappini, A. Basagni, M. Parravicini, A. Papagni, F. Sedona, E. Magnano, et al., *Chem. - A Eur. J.* **2015**, *21*, 5826–5835.
- [147] X.-L. Zhou, X.-Y. Zhu, J. M. White, *Surf. Sci. Rep.* **1991**, *13*, 73–220.
- [148] C. Frischkorn, M. Wolf, *Chem. Rev.* **2006**, *106*, 4207–33.
- [149] H. Petek, *J. Chem. Phys.* **2012**, *137*, 091704.
- [150] C. D. Lindstrom, X.-Y. Zhu, *Chem. Rev.* **2006**, *106*, 4281–300.
- [151] J. W. Gadzuk, *J. Chem. Phys.* **2012**, *137*, 091703.
- [152] M. Lisowski, P. A. Loukakos, U. Bovensiepen, J. St hler, C. Gahl, M. Wolf, *Appl. Phys. A Mater. Sci. Process.* **2004**, *78*, 165–176.
- [153] X.-Y. Zhu, J. M. White, *J. Chem. Phys.* **1991**, *94*, 1555.
- [154] L. Lafferentz, V. Eberhardt, C. Dri, C. Africh, G. Comelli, F. Esch, S. Hecht, L. Grill, *Nat. Chem.* **2012**, *4*, 215–20.
- [155] T. Faury, S. Clair, M. Abel, F. Dumur, D. Gigmes, L. Porte, *J. phys. Chem. C* **2012**, DOI Doi 10.1021/Jp300417g.
- [156] T. Lin, X. S. Shang, J. Adisojoso, P. N. Liu, N. Lin, *J. Am. Chem. Soc.* **2013**, *135*, 3576–82.
- [157] B. Cirera, Y.-Q. Zhang, J. Björk, S. Klyatskaya, Z. Chen, M. Ruben, J. V Barth, F. Klappenberger, *Nano Lett.* **2014**, *14*, 1891–7.
- [158] S. Linden, D. Zhong, a. Timmer, N. Aghdassi, J. H. Franke, H. Zhang, X. Feng, K. Müllen, H. Fuchs, L. Chi, et al., *Phys. Rev. Lett.* **2012**, *108*, 216801.
- [159] V. K. Kanuru, G. Kyriakou, S. K. Beaumont, A. C. Papageorgiou, D. J. Watson, R. M. Lambert, *J. Am. Chem. Soc.* **2010**, *132*, 8081–6.
- [160] G. Kuang, Q. Zhang, D. Y. Li, X. S. Shang, T. Lin, P. N. Liu, N. Lin, *Chem. - A Eur. J.* **2015**, n/a–n/a.
- [161] F. Sedona, M. Di Marino, M. Sambì, T. Carofiglio, E. Lubian, M. Casarin, E. Tondello, *ACS Nano* **2010**, *4*, 5147–54.
- [162] - user, *Langmuir* **2009**, *25*, 7342–7352.

Publications

- Andrea Basagni, Luciano Colazzo, Francesco Sedona, Marco DiMarino, Tommaso Carofiglio, Elisa Lubian, Daniel Forrer, Andrea Vittadini, Maurizio Casarin, Alberto Verdini, Albano Cossaro, Luca Floreano and Mauro Sambi. *Stereoselective Photopolymerization of Tetraphenylporphyrin Derivatives on Ag(110) at the Sub-Monolayer Level*. Chem. Eur. J. **2014**, 20, 14296 – 14304. Highlighted as “hot paper”
- Back-cover illustration of Chem. Eur. J. **2014** Volume 20, Issue 44.
- Andrea Basagni, Francesco Sedona, Carlo Pignedoli, Mattia Cattelan, Louis Nicolas, Maurizio Casarin, Mauro Sambi. *Molecules-oligomers-nanowires-graphene nanoribbons: a bottom-up stepwise on-surface covalent synthesis preserving long range order*. JACS **2015**, 137, 1802-1808.
- Andrea Basagni, Lara Ferrighi, Mattia Cattelan, Louis Nicolas, Karsten Handrup, Luca Vaghi, Antonio Papagni, Francesco Sedona, Cristiana di Valentin, Stefano Agnoli, Mauro Sambi. *On-surface photodissociation of C-Br bonds: towards room temperature Ullmann coupling*. Chem. Commun. **2015**, 51, 12593-12596.
- Andrea Basagni, Guillaume Vasseur, Carlo A. Pignedoli, Manuel Vilas-Varela, Diego Peña, Louis Nicolas, Lucia Vitali, Jorge Lobo-Checa, Dimas G. de Oteyza, Francesco Sedona, Maurizio Casarin, J. Enrique Ortega, and Mauro Sambi. *Tuning the one-dimensional band dispersion of on-surface synthesized organic nanowires*. ACS Nano, submitted, under revision.

Publications outside the research project

- Francesco Sedona, Marco Di Marino, Andrea Basagni, Luciano Colazzo, Mauro Sambi. *Structurally Tunable Self-Assembled 2D Cocrystals of C60 and Porphyrins on the Ag (110) Surface*. J. Phys. Chem. C, **2014**, 118, 1587–1593.
- Juan Bartolomé, Fernando Bartolomé, Nicholas B. Brookes, Francesco Sedona, Andrea Basagni, Daniel Forrer, Mauro Sambi. *Reversible Fe magnetic moment switching in catalytic oxygen reduction reaction of Fe-Phthalocyanine adsorbed on Ag(110)*. J. Phys Chem. C **2015**, 119, 12488-12495.
- Lara Ferrighi, Igor Pis, Thanh Hai Nguyen, Mattia Cattelan, Silvia Nappini, Andrea Basagni, Matteo Parravicini, Antonio Papagni, Francesco Sedona, Elena Magnano, Federica Bondino, Cristiana di Valentin, Stefano Agnoli. *Control of the intermolecular coupling of dibromotetracene on Cu(110) by the sequential activation of C-Br and C-H bonds*. Chem. Eur. J. **2015**, 21, 5826-5835.